Scratching the Surface of Colloidal InP Nanoparticles: Tuning the Physical and Electronic Structure through Surface Chemistry

Jennifer Lynn Stein

A dissertation

submitted in partial fulfillment of the

requirements for the degree of

Doctor of Philosophy

University of Washington

2018

Reading Committee:

Brandi M. Cossairt, Chair

Daniel R. Gamelin

Xiaosong Li

Program Authorized to Offer Degree:

Chemistry

University of Washington

Abstract

Scratching the Surface of Colloidal InP Nanoparticles: Tuning the Physical and Electronic Structure through Surface Chemistry

Jennifer Lynn Stein

Chair of the Supervisory Committee:
Assistant Professor Brandi M. Cossairt
Department of Chemistry

The structural and compositional variety of materials afforded by nanocrystal synthetic chemistry has established a foundation for developing high quality and tailored materials for a broad spectrum of applications, including photovoltaics, display and lighting, biological imaging, and catalysis. In all of these applications, colloidal processing presents a low-cost, highly scalable

strategy for manufacturing. Quantum-confined semiconductor nanocrystals, or quantum dots (QDs), have size-dependent optical and electronic properties that have been successfully exploited in commercial display technologies that require phosphors with high color purity and emission tunability. Cadmium-based materials have dominated the field with respect to efficient syntheses that can produce monodisperse and highly emissive QDs, but the toxic nature of cadmium has led to environmental regulations that limit the amount of cadmium permitted in consumer products in many countries. Indium phosphide nanomaterials, InP, have thus gained interest as lower toxicity phosphors that emit in the visible region.

The synthetic development of emissive InP QDs has encountered obstacles related to the more covalent nature of the crystal lattice and a lack of diverse precursor compounds. Furthermore, as-synthesized InP QDs are characterized by prohibitively weak emission that requires a non-trivial effort involving synthetic re-design or post-synthetic processing to improve photoluminescence quantum yields (PL QYs). This thesis works seeks to develop methods for overcoming this challenge. Chapter 1 summarizes the current state of InP QDs as viable commercial phosphors, including the strategies chemists use to improve PL QYs, and sets the stage for the following four chapters that target the rational design of PL enhancement strategies. Chapter 2 describes the interaction between InP QD surfaces and exogenous M^{2+} Lewis acids, revealing that M^{2+} cations (cadmium and zinc) undergo Z-type ligand exchange with surface indium, and through this shallow degree of alloying and surface passivation, impart distinct electronic properties and PL enhancement. In Chapter 3, the state of InP QD surface oxidation is discussed wherein adventitious side-reactions occur in common InP syntheses, resulting in the presence of oxidized phosphorus species that contribute to the non-radiative trap landscape that limits the obtainable QYs of surface-modified InP QDs. X-ray emission spectroscopy was used as a powerful technique to systematically and rapidly assess the degree of oxidation imparted in a series of InP syntheses and industrially-relevant shelling reactions.

In an alternative approach to direct and improve InP QD properties, InP magic-sized clusters (MSCs) were used as scaffolds for cation exchange where once again, surface chemistry plays a critical role in facilitating partial or complete cation exchange. Motivating these studies was an interest in developing a fundamental understanding of cation exchange mechanisms in the larger InP quantum dots, described in Chapter 2, and the appeal of employing alloyed clusters as single-source precursors to access emergent properties in InP QDs. Chapter 4 outlines the cation exchange reaction that takes place between InP MSCs and cadmium carboxylates, where incorporation of cadmium induces a complete structural rearrangement and full cation exchange to cadmium phosphide clusters. The findings from this study revealed the distinct reactivity differences between larger QDs and clusters, leading to the development of zinc alloyed clusters in Chapter 5 and their role as precursors for InP QDs.

TABLE OF CONTENTS

LIST OF FIGURES

LIST OF TABLES

ACKNOWLEDGEMENTS

Self-reflection is an important habit to uphold, said the hypocrite. I always like to offer that advice to younger students considering graduate school, yet I find that I personally did not spend enough time evaluating if I was accomplishing my goals. When I look back at the last five years spent at the University of Washington, I realize that is because I enjoyed every single day, including the months crawling by to see if a new project would pan out, the endless weekends cranking out tedious data, or the occasional chair-arm rattle of rage as another instrument went out of commission. I could not stand by this statement if not for the wonderful community that supported me over that time.

First, Brandi. I came to UW with the “Brandi or Bust” mentality and am incredibly grateful that my instincts were correct. She has a knack for tailoring her mentoring style to each unique student and with that skill, continued to teach, motivate, and support me in my scientific endeavors. I’ve never had the means to travel internationally so one of my most memorable grad school experiences is when Brandi popped her head into the office and told me I should check out this quantum dot conference in Korea (which was AMAZING). While I’m a little heartbroken that I won’t be able to see the next five years of Brandi and how she continues to evolve as a brilliant advisor, I have no doubt that our friendship will continue to flourish and my naturally nosy tendencies will be satisfied. Keep it silly, Brandi.

When it comes to the lab dynamic, dear Mike Norris would always remind me, “you don’t have to be friends with the people you work with”. He might have been right, but the friendship

I’ve developed with my peers made the work environment relaxed and fun. It also helps to have good rapport when I yell at everyone because they’re a bunch of filthy slobs and maybe someday they will learn to respect the shared working spaces. I wish Max Friedfeld had started his eternal post-doctoral fellowship a year or two earlier because he has been the salty rock for my barnacle; I only hope that the rest of the lab picks up on his immense value soon. Nayon and Penny have kept me well-fed, both literally and emotionally and I trust that we will always come together from our distant corners of the earth to be together. Lastly, Andrew Ritchhart should be commended for keeping me sane.

I couldn’t have gotten here today without the education I received from the Pacific Lutheran University Department of Chemistry. A special shout-out to Andrea Munro, Justin Lytle, and Neal Yakelis for fostering my interest in chemistry and helping me develop the analytical skills I would need to survive.

Finally, I love my mother and sister so much and I don’t think I can take all the credit for how much we’ve all grown and dealt with change in the last 5 years. I appreciate that my mother constantly makes an effort to spend time together, even when I get stressed and cranky and blow her off, especially in the weeks leading up to my defense. My second family, the Rainbow City Performing Arts, has been an outrageous, loving, and accepting community that I am continuously grateful to have been a part of. Sometimes it gets difficult to find your niche in the non-chemistry world but there they were, smothered in rainbow face paint and tootin’ on their horns, I couldn’t have asked for a better musical outlet. Finally, I’m grateful that my cat Maxwell put up with my long work hours yet still cared enough to cuddle with me at night.

Chapter 1. Introduction

1.1 Commercial Application of Luminescent Quantum Dots

Colloidal semiconductor nanocrystals, or quantum dots (QDs), are a valuable class of materials that are widely applicable in catalysis,[1] bioimaging,[2] photovoltaic devices,[3–5] and display technologies.[6,7] Nanocrystals achieve this broad versatility through the quantum confinement effect, a phenomenon that directly relates the size of the particle with the semiconductor band gap. Size-tunable band gaps are especially useful for display applications that utilize QDs as downconversion chromophores, in which red- and green-emitting particles are deposited in a film layer that is pumped by a high energy (blue) LED that can excite the QDs and induce radiative recombination.[7,8] QDs are additionally appealing materials for display devices because of their increased thermostability, solution-processability, and narrow luminescence linewidths as compared to more traditional molecular chromophores.[9]

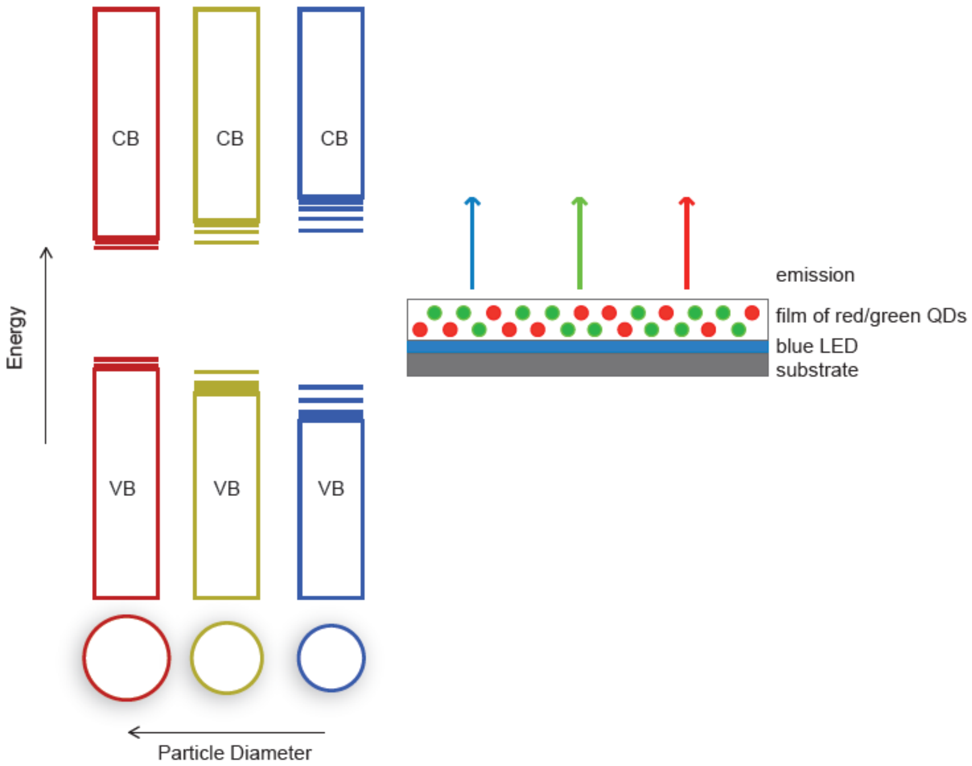

Figure 1.1. Depiction of semiconductor quantum confinement (left) and a simplified version of QD downconverters used in a light-emitting device (right).

To be a viable candidate for display materials, QDs must satisfy at least two criteria: 1) efficient radiative recombination, i.e. high photoluminescence quantum yields (PL QYs), meaning that every photon used to excite the semiconductor should be ejected as a lower energy photon, and 2) narrow emission linewidths, i.e. the sample is composed of monodisperse particles, resulting in high color purity. Thus far, cadmium selenide (CdSe) and other II-VI materials have dominated early exploration and commercial efforts and have been the leading materials to meet these requirements. CdSe QDs have been processed in display devices from companies such as LG, Phillips, Sony, Amazon, and others, from as early as 2013.[9] There has been growing concern over the environmental impact of such cadmium-containing materials, especially with the Restriction of Hazardous Substances limitations in Europe, thus a search for cadmium-free QDs has been gaining momentum.[10] Of these Cd-free materials, indium phosphide (InP), a III-V semiconductor, possesses several properties that make it an attractive alternative, such as a wider emission range, larger Bohr exciton radius, and lower toxicity.[11–13] However, current InP QD colloidal syntheses do not benefit from the same ease and reproducibility of metal chalcogenide syntheses. This difference has been attributed to the more covalent nature of the crystal lattice and the general scarcity of phosphorus precursors.[14]

1.2 Synthetic Challenges of InP QDs

Although various phosphorus precursors have been explored (e.g. P_4, TOP/TOPO, PH_3),[13] $P(SiMe_3)_3$ has remained a frontrunner dating back to 2002 in which the standard colloidal conditions, reaction between $P(SiMe_3)_3$ and long chain indium carboxylates and excess acid, were reported by Peng and co-workers.[15] Unfortunately, a long-standing issue accompanying this synthetic approach has been the rapid reaction of $P(SiMe_3)_3$ at elevated temperatures that depletes molecular precursors almost immediately, resulting in broader particle size distributions. In classical LaMer type growth, the separation of particle nucleation and growth affords monodisperse QD ensembles with narrow luminescence linewidths.[16,17] Efforts to tune the reactivity of $P(SiMe_3)_3$ resulted in the realization that InP QDs do not conform to LaMer growth kinetics and that growth proceeds through stable InP intermediates, known as magic-sized clusters.[18,19] Our lab has pursued the development of magic-sized InP clusters as precursors to quantum dots which will be discussed in greater detail in Chapter 5.

While the high reactivity of $P(SiMe_3)_3$ poses a barrier to producing samples with desirable luminescence linewidths, ideally in the range of 20-30 nm to compete with II-VI materials,[20] a greater issue lies in the fact that as-synthesized InP QDs exhibit PL QYs <1%. The lack of band edge emission has been attributed to the presence of surface defects, such as un-passivated atoms or oxidized species, that act as electronic trap sites with a high activation barrier for detrapping.[21–23] InP QD syntheses are performed under cation-rich conditions (2:1) to favor colloidal stability from the indium long-chain ligands, thus surface phosphorus atoms are considered highly suspect as the source of most non-radiative recombination. While the identification and depth of specific trap sites associated with electron or hole trapping was performed by Nozik and co-workers, the InP materials they studied were synthesized by an obsolete preparation that does not provide insight to modern InP QD materials.[21,24] Thus, a joint study between the Cossairt lab and the Gamelin lab at the University of Washington is underway in which a series of InP samples with various surface treatments are examined by time-resolved and ultra-fast spectroscopies.

1.3 Strategies to Enhance InP QD Emission

Due to the intrinsic lack of radiative emission in as-prepared InP QDs, a variety of approaches, such as fluoride etching, shelling, and alloying, have been examined (Figure 2). Synthetically, chemists have moved away from the use of highly corrosive HF in favor of fluoride-containing ionic liquids that can be utilized in the microwave synthesis of InP QDs and achieve PL QYs up to 50%.[23,25,26] There remains some controversy regarding the mechanism of etching with regard to which trap sites are affected and how fluoride ions interact with the surface, thus limiting the rational design of emissive materials due to the poor understanding of the underlying mechanism.[27,28] Conversely, the development and optimization of InP shell materials has grown considerably to meet the demand for thermo-, photo- and air-stable cadmium-free materials.

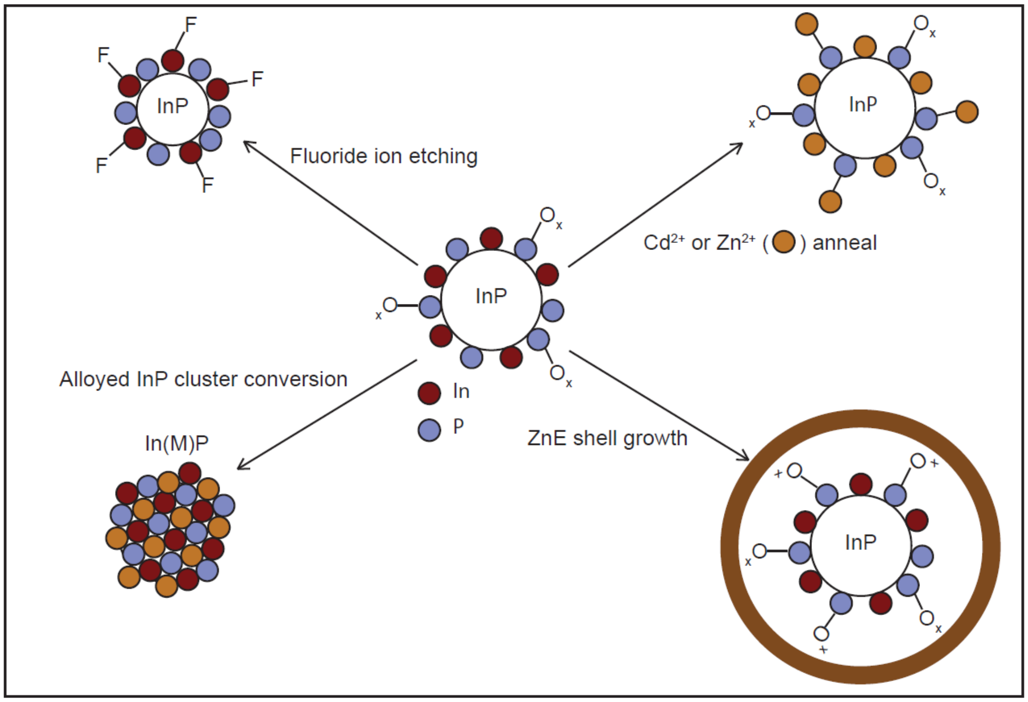

Figure 1.2. Strategies to improve InP QD PL. Most synthetic routes to InP QDs coincidentally oxidize the surface which is conserved following surface cation exchange or shell growth. Both fluoride-based etching and alloyed cluster conversion are in their early developmental stages.

Core/shell systems are classified as Type I, in which the shell has a wider band gap and effectively confines the exciton to the core, and Type II, where the band edges are offset and one of the carriers is delocalized into the shell. Regardless of the target carrier location, shells simultaneously provide a passivating layer for the core surface to enhance PL QYs and improve the chemical stability of the particle. Shell materials must be carefully selected for lattice compatibility, otherwise shell growth can result in strain-related defects at the mismatched interface and through compression of the core, even under optimized epitaxial deposition conditions.[29,30] Thus far, ZnS and ZnSe with lattice mismatches of 7.7% and 3.3%, respectively, have been the focus of InP shelling studies due to the absence of more toxic elements, i.e., lead, cadmium, and arsenic. Successive ionic layer adsorption and reaction (SILAR) is the typical strategy for shell deposition in which cation/anion precursors are added alternatingly to the core InP particles in dilute concentrations to avoid homonucleation of the shell material. Interestingly, the initial addition of cationic precursor alone was reported to enhance of PL QYs but the accompanying hypotheses were inconsistent.[31–33] These conflicting reports motivated the research described in Chapter 2 in which we pursued an understanding of the underlying pathway for PL enhancement through the simple addition of Lewis acids, or metal carboxylates.

Even with the most sophisticated shelling syntheses, InP QD quantum yields plateau at 85%.[34,35] While minimizing defects in the core and shell materials is necessary, perhaps the most crucial aspect of design is at the core-shell interface. InP QDs have been shown to be incredibly susceptible to surface oxidation from *in-situ* and *ex-situ* sources during both core and shell syntheses, resulting in oxidized phosphorus species that likely perturb conformal shell growth.[22,36,37] Chapter 3 outlines our efforts to quantify the oxidized phosphorus species across a series of common, but chemically distinct InP synthetic methods, and the impact these defects have on the optical properties of subsequently shelled InP QDs.

Finally, the last route to PL turn-on addressed in this manuscript is through compositional tailoring of nanoscale colloids, which has been highlighted as an aspect of synthetic chemistry that can access emergent properties of materials that would normally be unattainable in the binary semiconductor. This facile reaction employs the anionic sublattice as a template while cations partially or fully exchange, typically retaining the original crystallite size and shape. Experimental conditions have been developed to access a wide variety of doped nanocrystals, anisotropic structures, alloyed nanocrystals, nanocrystalline heterostructures, and semiconductor nanocrystals that are synthetically challenging to produce via a direct route.[38–40] Chemists have continued to develop this technique by extracting general design principles through examination of ion exchange thermodynamics and consideration of the shared similarities with solid-state ion exchange occurring over a reaction zone and by probing mechanism using a combination of theory, dynamic simulations, and experiment.[41–45]

1.4 Cation Exchange in InP QDs

Attempts to tune the cationic composition of InP QDs through alloying have taken two distinct approaches, the first of which involves the mixing of multiple metallic monomer species before the QD nucleation event and necessitates that the reactivity of the precursors is well-matched.[46–49] Thus far, this approach has sacrificed control of the dopant atom location (e.g. surface vs core) in favor of a straightforward synthetic method that offers control over InP optical properties. The second method takes a reverse approach to InP cation exchange by utilizing pre-formed metal phosphide nanostructures as the anionic template for insertion of indium. These examples encompass $Cu_{3-x}P$ and Cd_3P_2 as the foundation for this reverse-type of cation exchange where nearly composition-pure InP nanostructures were achieved.[50,51] The authors noted that in the case of the Cd_3P_2 to InP phase transformation, the reverse ion exchange reactions (InP to Cd_3P_2) were highly irreversible as the diffusion of In^{3+} for Cd^{2+} already required elevated temperatures.[51] In chapter 2, we similarly observed a high activation barrier of cation exchange through the Z-type ligand exchange of cadmium and zinc Lewis acids on InP QDs.

In an effort to directly probe the mechanism and structural consequences of alloying, magic-sized clusters can be employed as a model system. Magic-sized clusters (MSCs) represent the interface between small molecules and quantum-confined nanostructures. MSCs are atomically precise clusters with elevated thermodynamic stability compared to structures of similar size that can play a role in nanocrystal nucleation and growth. Beyond the application of clusters as quantum dot precursors, atomically precise clusters provide a unique opportunity to take advantage of the spectroscopic handles that accompany the their perfect monodispersity and homogeneity of their surface chemistry. Often, alloyed nanocrystals need to be characterized as the "average" ensemble of nanocrystals that contain some amount of dopant atom that impart the new observed properties. In this regard, atomically precise clusters serve as ideal models for elucidating the interaction and position of the substituted atoms in a host lattice that directs the resulting properties.

A principal example of an atomically precise cluster model system is the work surrounding cation exchange in tetrameric metal thiolate cluster.[52,53] Using tetrameric metal thiolate clusters as models for metal chalcogenide nanocrystals, Kittilstved and co-workers were able to assign the site-specific incorporation of dopant Mn^{2+} ions (surface vs core) and accompanying outwards-diffusion of dopants over time, contributing invaluable insight to the rational design of larger doped nanocrystals.[54] Other noteworthy research has centered on the doping and alloying of stoichiometric $(CdSe)_n$ nanocluster species, whose specific compositions are inferred by mass spectrometry. These clusters have been examined as not only Mn^{2+}-doped and alloyed precursors to nanomaterials,[55] but as a model to probe the co-operative nature of Cu^+ cation exchange observed in larger CdSe nanocrystals.[56] In spite of the unidentified crystal structure of these $(CdSe)_{33,34}$ nanoclusters, these types of fundamental studies that utilize species with distinct spectroscopic and structural handles can further enhance our understanding and development of compositional tailoring in larger nanostructures.

The advent of an atomically precise InP cluster was appealing to further probe the potential of cation exchange in materials with more covalent character compared to the breadth of more ionic metal chalcogenide nanocrystal lattices. A diffraction-quality single crystal of

$In_{37}P_{20}(O_2CCH_2Ph)_{51}$, an InP MSC, revealed a strained $[In_{21}P_{20}]^{3+}$ inorganic core ligated by 16 additional indium atoms and an interconnected network of 51 bidentate and mostly bridging carboxylate ligands.[57] Our lab has observed that the InP MSC displays site-selective reactivity when exposed to moist air, leading to a carboxylate ligand shift (bidentate to monodentate) in order to accommodate a water molecule bound to an indium. Furthermore, exposure to Lewis bases, i.e. amines, initiated indium carboxylate desorption and ultimately structural rearrangement of the cluster.[58] Thus, utilizing InP MSCs as templates for cation exchange reactions toward new cluster materials with the ability to predict the progression of the reaction was of great interest to us. The related chemistry will be described in Chapters 4 and 5.

1.5 References

(1) Weiss, E. A. Designing the Surfaces of Semiconductor Quantum Dots for Colloidal Photocatalysis. *ACS Energy Lett.* **2017**, *2* (5), 1005–1013.

(2) Kairdolf, B. A.; Smith, A. M.; Stokes, T. H.; Wang, M. D.; Young, A. N.; Nie, S. Semiconductor Quantum Dots for Bioimaging and Biodiagnostic Applications. *Annu. Rev. Anal. Chem. Palo Alto Calif* **2013**, *6* (1), 143–162.

(3) Tang, J.; Sargent, E. H. Infrared Colloidal Quantum Dots for Photovoltaics: Fundamentals and Recent Progress. *Adv. Mater.* **2011**, *23* (1), 12–29.

(4) Semonin, O. E.; Luther, J. M.; Beard, M. C. Quantum Dots for Next-Generation Photovoltaics. *Mater. Today* **2012**, *15* (11), 508–515.

(5) Li, X.-B.; Tung, C.-H.; Wu, L.-Z. Semiconducting Quantum Dots for Artificial Photosynthesis. *Nat. Rev. Chem.* **2018**, 1.

(6) McKittrick, J.; Shea-Rohwer, L. E. Review: Down Conversion Materials for Solid-State Lighting. *J. Am. Ceram. Soc.* **2014**, *97* (5), 1327–1352.

(7) Supran, G. J.; Shirasaki, Y.; Song, K. W.; Caruge, J.-M.; Kazlas, P. T.; Coe-Sullivan, S.; Andrew, T. L.; Bawendi, M. G.; Bulović, V. QLEDs for Displays and Solid-State Lighting. *MRS Bull.* **2013**, *38* (09), 703–711.

(8) Talapin, D. V.; Steckel, J. Quantum Dot Light-Emitting Devices. *MRS Bull.* **2013**, *38* (09), 685–691.

(9) Steckel, J. S.; Ho, J.; Hamilton, C.; Xi, J.; Breen, C.; Liu, W.; Allen, P.; Coe-Sullivan, S. Quantum Dots: The Ultimate down-Conversion Material for LCD Displays. *J. Soc. Inf. Disp.* **2015**, *23* (7), 294–305.

(10) 2018 RoHS Compliance Guide: Regulations, 10 Substances, Exemptions, WEEE http://www.rohsguide.com/ (accessed Jul 28, 2018).

(11) R. Heath, J. Covalency in Semiconductor Quantum Dots. *Chem. Soc. Rev.* **1998**, *27* (1), 65–71.

(12) Green, M. M. Solution Routes to III–V Semiconductor Quantum Dots. *Curr. Opin. Solid State Mater. Sci. - CURR OPIN SOLID STATE MAT SCI* **2002**, *6*, 355–363.

(13) Tamang, S.; Lincheneau, C.; Hermans, Y.; Jeong, S.; Reiss, P. Chemistry of InP Nanocrystal Syntheses. *Chem. Mater.* **2016**, *28* (8), 2491–2506.

(14) Cossairt, B. M. Shining Light on Indium Phosphide Quantum Dots: Understanding the Interplay among Precursor Conversion, Nucleation, and Growth. *Chem. Mater.* **2016**, *28* (20), 7181–7189.

(15) Battaglia, D.; Peng, X. Formation of High Quality InP and InAs Nanocrystals in a Noncoordinating Solvent. *Nano Lett.* **2002**, *2* (9), 1027–1030.

(16) LaMer, V. K.; Dinegar, R. H. Theory, Production and Mechanism of Formation of Monodispersed Hydrosols. *J. Am. Chem. Soc.* **1950**, *72* (11), 4847–4854.

(17) Thanh, N. T. K.; Maclean, N.; Mahiddine, S. Mechanisms of Nucleation and Growth of Nanoparticles in Solution. *Chem. Rev.* **2014**, *114* (15), 7610–7630.

(18) Gary, D. C.; Glassy, B. A.; Cossairt, B. M. Investigation of Indium Phosphide Quantum Dot Nucleation and Growth Utilizing Triarylsilylphosphine Precursors. *Chem. Mater.* **2014**, *26* (4), 1734–1744.

(19) Gary, D. C.; Terban, M. W.; Billinge, S. J. L.; Cossairt, B. M. Two-Step Nucleation and Growth of InP Quantum Dots via Magic-Sized Cluster Intermediates. *Chem. Mater.* **2015**, *27* (4), 1432–1441.

(20) Cui, J.; Beyler, A. P.; Marshall, L. F.; Chen, O.; Harris, D. K.; Wanger, D. D.; Brokmann, X.; Bawendi, M. G. Direct Probe of Spectral Inhomogeneity Reveals Synthetic Tunability of Single-Nanocrystal Spectral Linewidths. *Nat Chem* **2013**, *5* (7), 602–606.

(21) Mićić, O. I.; Nozik, A. J.; Lifshitz, E.; Rajh, T.; Poluektov, O. G.; Thurnauer, M. C. Electron and Hole Adducts Formed in Illuminated InP Colloidal Quantum Dots Studied by Electron Paramagnetic Resonance. *J. Phys. Chem. B* **2002**, *106* (17), 4390–4395.

(22) Cros-Gagneux, A.; Delpech, F.; Nayral, C.; Cornejo, A.; Coppel, Y.; Chaudret, B. Surface Chemistry of InP Quantum Dots: A Comprehensive Study. *J. Am. Chem. Soc.* **2010**, *132* (51), 18147–18157.

(23) Micic, O. I.; Sprague, J.; Lu, Z.; Nozik, A. J. Highly Efficient Band Edge Emission from InP Quantum Dots. *Appl. Phys. Lett.* **1996**, *68* (22), 3150–3152.

(24) Langof, L.; Ehrenfreund, E.; Lifshitz, E.; Micic, O. I.; Nozik, A. J. Continuous-Wave and Time-Resolved Optically Detected Magnetic Resonance Studies of Nonetched/Etched InP Nanocrystals. *J. Phys. Chem. B* **2002**, *106* (7), 1606–1612.

(25) Lovingood, D. D.; Strouse, G. F. Microwave Induced In-Situ Active Ion Etching of Growing InP Nanocrystals. *Nano Lett.* **2008**, *8* (10), 3394–3397.

(26) Siramdas, R.; McLaurin, E. J. InP Nanocrystals with Color-Tunable Luminescence by Microwave-Assisted Ionic-Liquid Etching. *Chem. Mater.* **2017**, *29* (5), 2101–2109.

(27) Adam, S.; McGinley, C.; Möller, T.; Talapin, D. V.; Borchert, H.; Haase, M.; Weller, H. Photoemission Study of Size Selected InP Nanocrystals: The Relationship between Luminescence Yield and Surface Structure. *Eur. Phys. J. - At. Mol. Opt. Plasma Phys.* **2003**, *24* (1), 373–376.

(28) Adam, S.; Talapin, D. V.; Borchert, H.; Lobo, A.; McGinley, C.; de Castro, A. R. B.; Haase, M.; Weller, H.; Möller, T. The Effect of Nanocrystal Surface Structure on the Luminescence Properties: Photoemission Study of HF-Etched InP Nanocrystals. *J. Chem. Phys.* **2005**, *123* (8), 084706–084710.

(29) Rafipoor, M.; Dupont, D.; Tornatzky, H.; Tessier, M. D.; Maultzsch, J.; Hens, Z.; Lange, H. Strain Engineering in InP/(Zn,Cd)Se Core/Shell Quantum Dots. *Chem. Mater.* **2018**, *30* (13), 4393–4400.

(30) Gong, K.; Kelley, D. F. Lattice Strain Limit for Uniform Shell Deposition in Zincblende CdSe/CdS Quantum Dots. *J. Phys. Chem. Lett.* **2015**, *6* (9), 1559–1562.

(31) Park, J. K., Sunghoon; Kim, Sungwoo; Yu, Seung Tack; Lee, Bunyeoul; Kim, Sang-Wook. Fabrication of Highly Luminescent InP/Cd and InP/CdS Quantum Dots. *J. Lumin.* **2010**, *130*, 1825–1828.

(32) Ryu, E.; Kim, S.; Jang, E.; Jun, S.; Jang, H.; Kim, B.; Kim, S.-W. Step-Wise Synthesis of InP/ZnS Core−Shell Quantum Dots and the Role of Zinc Acetate. *Chem. Mater.* **2009**, *21* (4), 573–575.

(33) Xu, S.; Ziegler, J.; Nann, T. Rapid Synthesis of Highly Luminescent InP and InP/ZnS Nanocrystals. *J. Mater. Chem.* **2008**, *18* (23), 2653–2656.

(34) Jun, S. A.; Jang, E. J.; KWON, S. K.; KIM, T. H.; LEE, W. J. Semiconductor Nanocrystal, and Method of Preparing the Same. US20140117292A1, May 1, 2014.

(35) Kim, S.; Kim, T.; Kang, M.; Kwak, S. K.; Yoo, T. W.; Park, L. S.; Yang, I.; Hwang, S.; Lee, J. E.; Kim, S. K.; et al. Highly Luminescent InP/GaP/ZnS Nanocrystals and Their Application to White Light-Emitting Diodes. *J. Am. Chem. Soc.* **2012**, *134* (8), 3804–3809.

(36) Virieux, H.; Le Troedec, M.; Cros-Gagneux, A.; Ojo, W.-S.; Delpech, F.; Nayral, C.; Martinez, H.; Chaudret, B. InP/ZnS Nanocrystals: Coupling NMR and XPS for Fine Surface and Interface Description. *J. Am. Chem. Soc.* **2012**, *134* (48), 19701–19708.

(37) Jasinski, J.; Leppert, V. J.; Lam, S.-T.; Gibson, G. A.; Nauka, K.; Yang, C. C.; Zhou, Z.-L. Rapid Oxidation of InP Nanoparticles in Air. *Solid State Commun.* **2007**, *141* (11), 624–627.

(38) Rivest, J. B.; Jain, P. K. Cation Exchange on the Nanoscale: An Emerging Technique for New Material Synthesis, Device Fabrication, and Chemical Sensing. *Chem. Soc. Rev.* **2013**, *42* (1), 89–96.

(39) Beberwyck, B. J.; Surendranath, Y.; Alivisatos, A. P. Cation Exchange: A Versatile Tool for Nanomaterials Synthesis. *J. Phys. Chem. C* **2013**, *117* (39), 19759–19770.

(40) De Trizio, L.; Manna, L. Forging Colloidal Nanostructures via Cation Exchange Reactions. *Chem. Rev.* **2016**, *116* (18), 10852–10887.

(41) Backhaus-Ricoult, M. Solid-State Reactivity at Heterophase Interfaces. *Annu. Rev. Mater. Res.* **2003**, *33* (1), 55–90.

(42) Wark, S. E.; Hsia, C.-H.; Son, D. H. Effects of Ion Solvation and Volume Change of Reaction on the Equilibrium and Morphology in Cation-Exchange Reaction of Nanocrystals. *J. Am. Chem. Soc.* **2008**, *130* (29), 9550–9555.

(43) Ott, F. D.; Spiegel, L. L.; Norris, D. J.; Erwin, S. C. Microscopic Theory of Cation Exchange in CdSe Nanocrystals. *Phys. Rev. Lett.* **2014**, *113* (15), 156803.

(44) Zheng, Z.; Sun, Y.-Y.; Xie, W.; Zhao, J.; Zhang, S. Solvent-Based Atomistic Theory for Doping Colloidal-Synthesized Quantum Dots via Cation Exchange. *J. Phys. Chem. C* **2016**, *120* (47), 27085–27090.

(45) Bothe, C.; Kornowski, A.; Tornatzky, H.; Schmidtke, C.; Lange, H.; Maultzsch, J.; Weller, H. Solid-State Chemistry on the Nanoscale: Ion Transport through Interstitial Sites or Vacancies? *Angew. Chem. Int. Ed.* **2015**, *54* (47), 14183–14186.

(46) Tessier, M. D.; Dupont, D.; De Nolf, K.; De Roo, J.; Hens, Z. Economic and Size-Tunable Synthesis of InP/ZnE (E = S, Se) Colloidal Quantum Dots. *Chem. Mater.* **2015**, *27* (13), 4893–4898.

(47) Pietra, F.; De Trizio, L.; Hoekstra, A. W.; Renaud, N.; Prato, M.; Grozema, F. C.; Baesjou, P. J.; Koole, R.; Manna, L.; Houtepen, A. J. Tuning the Lattice Parameter of InxZnyP for Highly Luminescent Lattice-Matched Core/Shell Quantum Dots. *ACS Nano* **2016**, *10* (4), 4754–4762.

(48) Xi, L.; Cho, D.-Y.; Duchamp, M.; Boothroyd, C. B.; Lek, J. Y.; Besmehn, A.; Waser, R.; Lam, Y. M.; Kardynal, B. Understanding the Role of Single Molecular ZnS Precursors in the Synthesis of In(Zn)P/ZnS Nanocrystals. *ACS Appl. Mater. Interfaces* **2014**, *6* (20), 18233–18242.

(49) Koh, S.; Eom, T.; Kim, W. D.; Lee, K.; Lee, D.; Lee, Y. K.; Kim, H.; Bae, W. K.; Lee, D. C. Zinc–Phosphorus Complex Working as an Atomic Valve for Colloidal Growth of Monodisperse Indium Phosphide Quantum Dots. *Chem. Mater.* **2017**, *29* (15), 6346–6355.

(50) De Trizio, L.; Gaspari, R.; Bertoni, G.; Kriegel, I.; Moretti, L.; Scotognella, F.; Maserati, L.; Zhang, Y.; Messina, G. C.; Prato, M.; et al. Cu3-XP Nanocrystals as a Material Platform for Near-Infrared Plasmonics and Cation Exchange Reactions. *Chem. Mater.* **2015**, *27* (3), 1120–1128.

(51) Beberwyck, B. J.; Alivisatos, A. P. Ion Exchange Synthesis of III–V Nanocrystals. *J. Am. Chem. Soc.* **2012**, *134* (49), 19977–19980.

(52) Pittala, S.; Mortelliti, M. J.; Kato, F.; Kittilstved, K. R. Substitution of Co2+ Ions into CdS-Based Molecular Clusters. *Chem. Commun.* **2015**, *51* (96), 17096–17099.

(53) Pittala, S.; Kittilstved, K. R. Cation Exchange in Small ZnS and CdS Molecular Analogues. *Inorg. Chem.* **2015**, *54* (12), 5757–5767.

(54) Kato, F.; Kittilstved, K. R. Site-Specific Doping of Mn2+ in a CdS-Based Molecular Cluster. *Chem. Mater.* **2018**.

(55) Yang, J.; Muckel, F.; Baek, W.; Fainblat, R.; Chang, H.; Bacher, G.; Hyeon, T. Chemical Synthesis, Doping, and Transformation of Magic-Sized Semiconductor Alloy Nanoclusters. *J. Am. Chem. Soc.* **2017**, *139* (19), 6761–6770.

(56) White, S. L.; Banerjee, P.; Chakraborty, I.; Jain, P. K. Ion Exchange Transformation of Magic-Sized Clusters. *Chem. Mater.* **2016**, *28* (22), 8391–8398.

(57) Gary, D. C.; Flowers, S. E.; Kaminsky, W.; Petrone, A.; Li, X.; Cossairt, B. M. Single-Crystal and Electronic Structure of a 1.3 Nm Indium Phosphide Nanocluster. *J. Am. Chem. Soc.* **2016**, *138* (5), 1510–1513.

(58) Gary, D. C.; Petrone, A.; Li, X.; Cossairt, B. M. Investigating the Role of Amine in InP Nanocrystal Synthesis: Destabilizing Cluster Intermediates by Z-Type Ligand Displacement. *Chem. Commun.* **2016**, *53* (1), 161–164.

Chapter 2. Luminescent InP Quantum Dots with Tunable Emission by Post-Synthetic Modification with Lewis Acids

Adapted with permission from the Journal of Physical Chemistry Letters. Copyright 2016 American Chemical Society.

2.1 Note Regarding Collaborator Contributions:

This work was performed in collaboration with Dr. Elizabeth Mader, who at the time was a research scientist with Professor Jim Mayer's group at Yale University. Part of this work was performed at sector 10-BM, a beamline part of the Materials Research Collaborative Access Team at the Advanced Photon Source located at Argonne National Lab. Dr. Mader had extensive training on this beamline and was able to provide training and assistance in preparing samples, data collection, and data analysis. In particular, I am grateful for her resourcefulness with regard to appropriate air-free solution vessels and her ability to extract meaningful fits from Athena and WinXAS. All of the following EXAFS quantitative fits for experimental data and reference compounds were prepared by Dr. Mader. Additionally, in an ongoing collaboration to examine the exciton dynamics upon various surface treatments, the time-resolved photoluminescence data reported in this chapter was collected by Kira Hughes, working under Professor Daniel Gamelin in the Department of Chemistry at the University of Washington.

2.2 Introduction

In order to meet the rapidly increasing global energy demand, it is important not only to find new and renewable forms of energy, but to use energy more efficiently. One market that could make a significant impact on energy consumption is solid state lighting (SSL). A switch from incandescent lighting to SSL could save 217 TWh by 2025 in the US alone.[1,2] Semiconductor quantum dots (QDs) are a promising class of chromophores for this application because their wavelength tunability and narrow luminescence linewidths have the potential to give SSL the appropriate color rendering index and correlated color temperature to compete aesthetically with incandescent lighting.[3] As such, CdSe QDs have dominated early exploration and commercial efforts in the area of down-conversion fluorophores for SSL and displays, however the toxicity of cadmium presents a marked barrier to wide-scale commercialization efforts and a significant environmental concern. Indium phosphide (InP) is an attractive alternative due to its lower toxicity, larger intrinsic extinction coefficient,[4] larger Bohr exciton radius, wider emission range, and enhanced optical stability.[5–7] However, current InP QD colloidal syntheses have photoluminescence quantum yields (PL QY) of <1% due to surface defects that introduce mid-gap trap states, and a high activation barrier for detrapping.[8–10]

One successful strategy to increase InP PL QY has been to shell InP cores with ZnS, leading to PL QYs as high as 60%.[11] The increased PL QY has been attributed to passivation of surface defects on the InP core and a relatively low lattice mismatch (7.6%) between the ZnS and InP. Shell growth is achieved through a variety of methods that range from decomposing a ZnS single-source precursor, one-pot InPZnS synthesis, or the synthesis of InP cores followed by a second discrete shell growth step.[12–18] In the case of step-wise shell growth from Zn^{2+} and S^{2-} precursors on an InP core, an increased QY (ranging up to 20%) was seen after the initial addition of zinc carboxylate.[12,14,15] A similar observation was also noted in the stepwise addition of Cd^{2+} and S^{2-} precursors for InP/CdS core-shell QDs with a 36% PL QY after addition of cadmium acetylacetonate.[19] Varied proposals have emerged to explain the improvement in PL QY including surface passivation, etching in the case of zinc,[15] or doping in the case of cadmium.[19] However, a detailed understanding of this phenomenon is lacking and more data are needed to gain insight into the mechanism of PL QY enhancement.

In this paper we report the systematic investigation of the mechanism of PL turn-on by the post-synthetic addition of metal carboxylates, specifically zinc and cadmium, to InP QDs. Although cadmium is toxic, precedent in the literature for cadmium salts to passivate quantum dot surfaces and improve photoluminescence has made it of academic interest in this study and may be used to devise a general strategy with other soft Lewis acids.[20] We hypothesize that exogenous Lewis acids bind to under-coordinated surface phosphorus atoms leading to bonding interactions that lower the energy of the relevant orbitals below the valence band edge. We have observed PL enhancement of InP particles with QYs up to 49% with the addition of cadmium oleate and up to 19% with zinc oleate. An additional feature of these treatments is the ability to tune the absorbance and emission profiles of the QDs with no apparent change in particle size. The addition of zinc oleate tunably blue-shifts the optical features of the InP while addition of cadmium oleate causes a tunable red-shift in the optical features. Given the difficulty in synthetically accessing InP of different sizes,[21,22] this observation opens up a new approach to tune the emission color of this quantum confined material.

2.3 Results and Discussion

To investigate the effect of metal carboxylates on the PL QY of InP QDs, cadmium or zinc oleate were mixed with as-synthesized InP QDs in 1-octadecene and heated. Further synthetic details and optimization experiments are included in the experimental section. The as-synthesized InP QDs exhibit weak band edge luminescence and broad, red-shifted trap emission, with an overall PL QY <1% (Figure 2.1). After addition of Zn^{2+} or Cd^{2+}, we observed quantum yields in the range of 10-20% with zinc oleate and 20-50% with cadmium oleate. This range in QY depends on the Lewis acid concentration, particle size, duration, and temperature of thermal treatment. Maximum PL QYs were obtained at 200 °C for 3 hours with 2:1 Cd:In and 1.4:1 Zn:In concentrations.

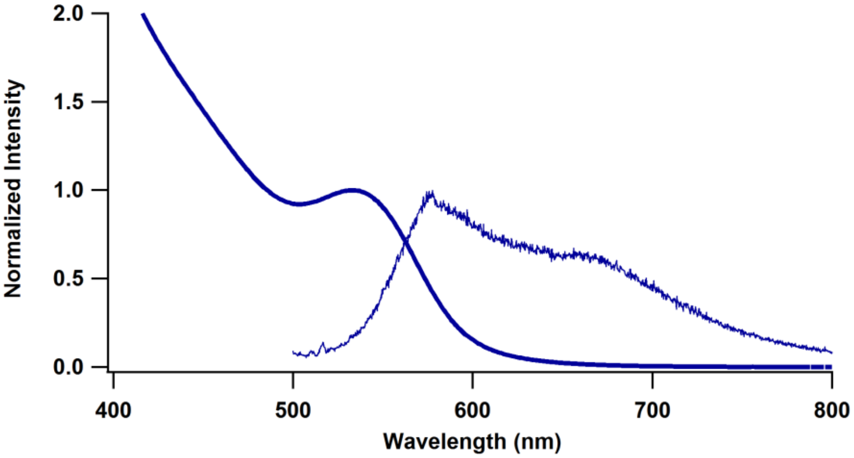

Figure 2.1. Normalized absorbance and emission of as-synthesized InP QDs. The emission profile with a quantum yield <1% is a combination of band edge luminescence at 586 nm and broad red-shifted defect emission.

A bathochromic shift was observed in the optical features of cadmium treated particles (referred to as Cd-InP) relative to the as-synthesized InP. Conversely, a hypsochromic shift in the optical features of zinc treated particles (Zn-InP) relative to as-synthesized InP was observed. The extent of these shifts were found to be a function of the amount of Lewis acid added, with larger magnitude shifts observed at higher concentrations (Figure 2.2). Figure 2.3 shows the UV-Vis and emission spectra of the initial and optimal Lewis acid-modified InP. It is important to note that the observed PL enhancement and optical tuning is not universal to all carboxylate salts or the carboxylate anion itself. Addition of indium myristate results in negligible PL enhancement, consistent with reports of poor luminescence in In-rich InP QDs,[23–25] while addition of tetrabutylammonium carboxylate has no impact on PL QY. The inability of $In(O_2CR)_3$ to completely passivate the particle surface and turn on luminescence stands in contrast to what is found for the $M(O_2CR)_2$ salts and may be associated with the higher coordination number and larger steric profile of trivalent Lewis acids with their associated anionic ligands. PL lifetimes were fit to biexponential decay kinetics yielding a weighted lifetime of 21 ns, 56 ns, and 178 ns for InP, Zn-InP, and Cd-InP, respectively (Figure 2.4). The time constant for InP is consistent with previous literature reports of InP QDs whereas the increase with either Zn-InP or Cd-InP indicates that hole traps associated with phosphorus dangling bonds are quenched through M^{2+} coordination.[16,25]

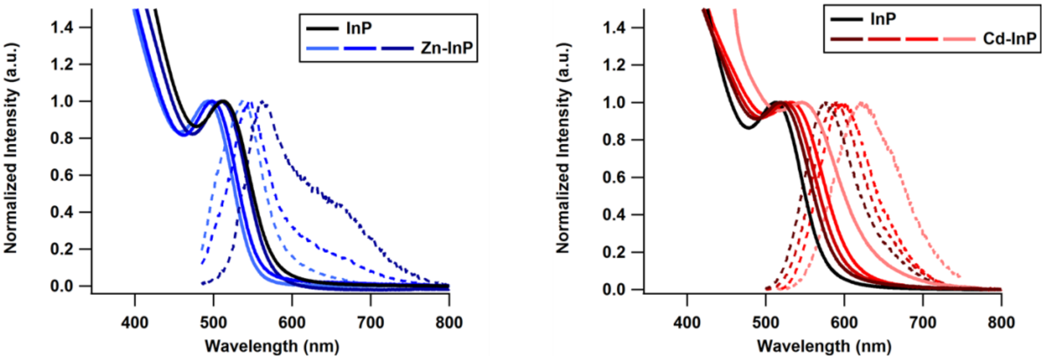

Figure 2.2. Absorbance (solid) and PL (dashed) spectra of InP QDs treated with increasing concentrations of zinc or cadmium. Zinc blue-shifts the optical properties (dark blue to light blue corresponds to increasing [Zn]), while cadmium red-shifts InP optical properties (dark red to light red corresponds to increasing [Cd].

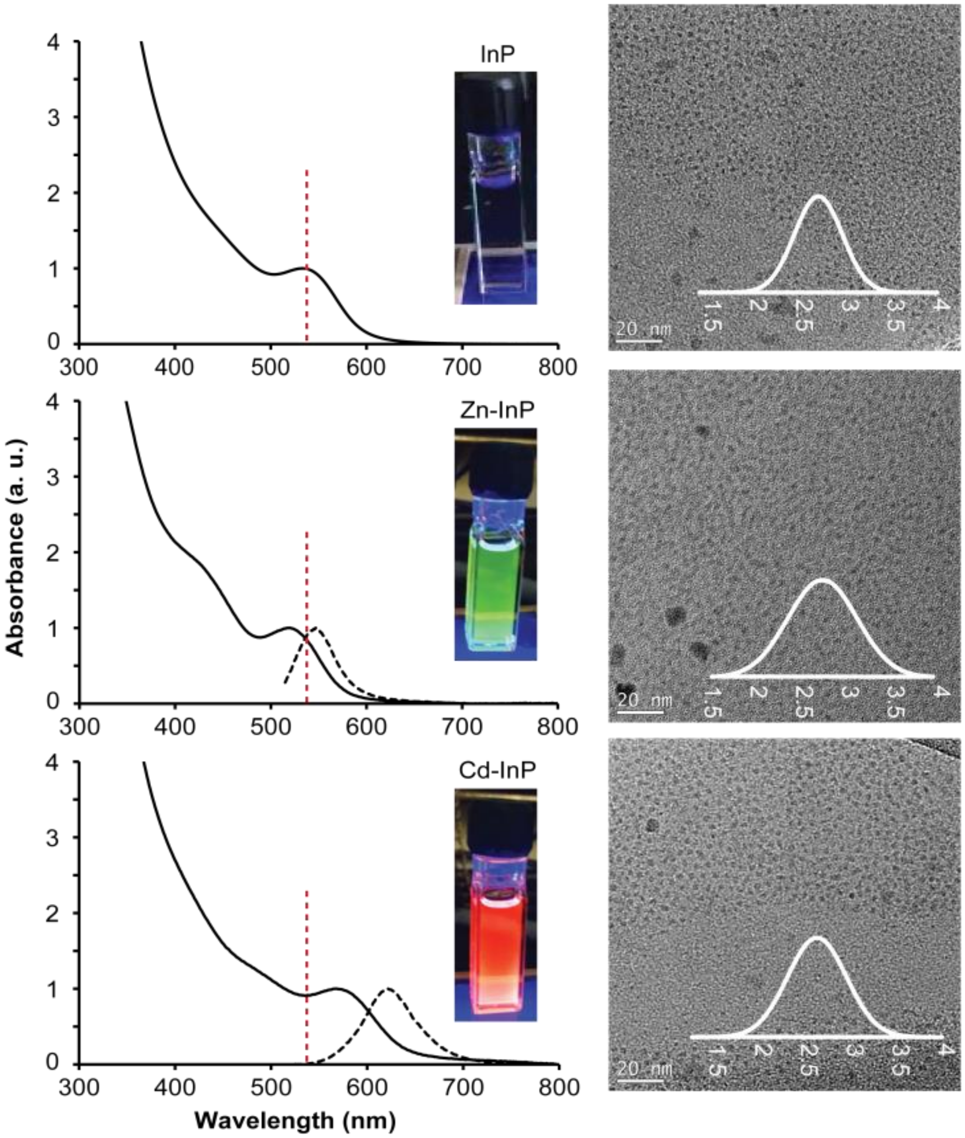

Figure 2.3. Absorbance (solid) and PL (dashed) spectra of Zn-InP (abs 498 nm, em 545 nm, PLQY 16±4%), InP, and Cd-InP (abs 530 nm, em 590 nm, PL QY 30±11%). Quantum yields represent an average of 3 independent samples. The red line indicates the lowest energy electronic transition (LEET) of the original InP QDs (513 nm). Particle sizes were determined for each sample by measuring 200 independent particles using TEM.

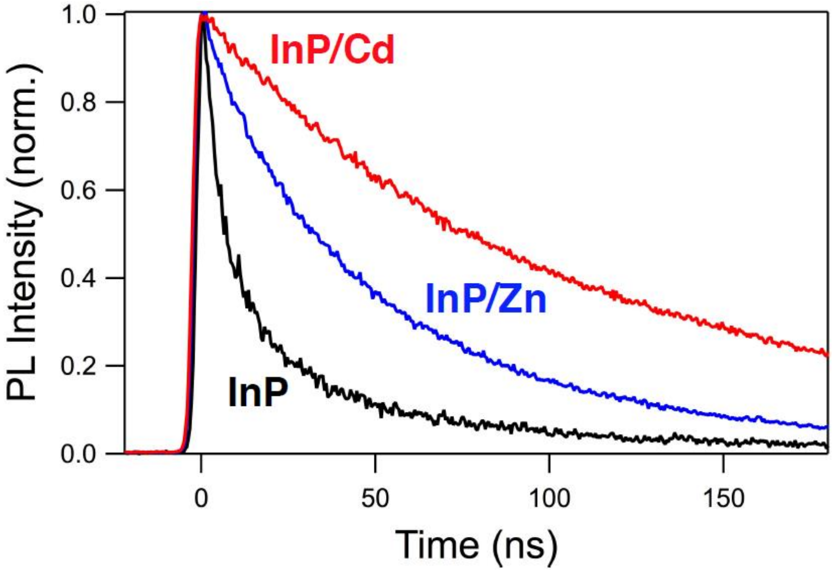

Figure 2.4. Time-resolved photoluminescence spectra of InP, InP/Zn, and InP/Cd QDs, collected and analyzed by Kira Hughes, Gamelin Lab.

To form a better understanding of the observed luminescence tuning we characterized the structure and composition of both the core and surface of the QDs using a combination of transmission electron microscopy (TEM), powder X-ray diffraction (XRD), elemental analysis, X-ray absorption spectroscopy and chemical etching. All measurements were performed on purified samples (as described in the experimental section). Notably, the PL QY of Lewis acid treated QDs is retained following purification indicating that the added metal cations are either strongly coordinated to the surface or incorporated into the crystal lattice.

TEM imaging indicates that the size of the particles remains unchanged by the Lewis acid treatment (Figure 2.3), despite the observed changes in the LEET and emission maxima that were initially attributed to the quantum confinement effect. The average size of the as-synthesized InP particles, 2.5 ± 0.4 nm, is maintained after treatment with metal carboxylates (2.6 ± 0.3 nm for Zn-InP and 2.5 ± 0.3 nm for Cd-InP). Powder X-ray diffraction data shows that In_2O_3 is generated as a coproduct upon treatment of InP with Cd^{2+} and Zn^{2+} salts (Figure 2.5). The average size of the

In_2O_3 particles in these samples was predicted to be 11.4 nm by Scherrer analysis of the In_2O_3 diffraction peak at 35° 2θ. This is consistent with TEM data where new, larger particles with an average size of 9.8 ± 1.1 nm are observed. Purification of the modified particle solutions by filtering through Celite removes most of the In_2O_3 as determined by the observed decrease of the In_2O_3 peak magnitude in the XRD patterns. The mechanism of In_2O_3 formation remains unclear, although it may result from exchange between added metal ions and surface In carboxylate where the displaced In carboxylate would have the potential to thermally decompose to In_2O_3.[26] After removing In_2O_3, the powder diffraction patterns in Figure 2.5b agree with those of nanocrystalline InP with a slight shift in the peak at 44° 2θ towards smaller diffraction angles. Since the shift is the same in both cadmium and zinc-treated samples, we attribute this to lattice strain introduced upon moving from an In^{3+} to a M^{2+} rich surface, however formation of a thin shell cannot be explicitly ruled out. In either case, significant strain is expected since the lattice constants of InP (zinc blende a = 5.86 Å) versus Zn_3P_2 (tetragonal phase a = 8.09 Å, c = 11.45 Å) and Cd_3P_2 (tetragonal phase a = 8.75 Å, c = 12.26 Å) differ considerably. Otherwise, the lack of any additional features indicates that no other crystalline compounds, such as separate populations of Zn_3P_2 or Cd_3P_2 particles, have been formed. The breadth of the InP diffraction peaks, while consistent across all samples, prevents additional commentary on expansion or contraction of the lattice that may arise from minor alloying.

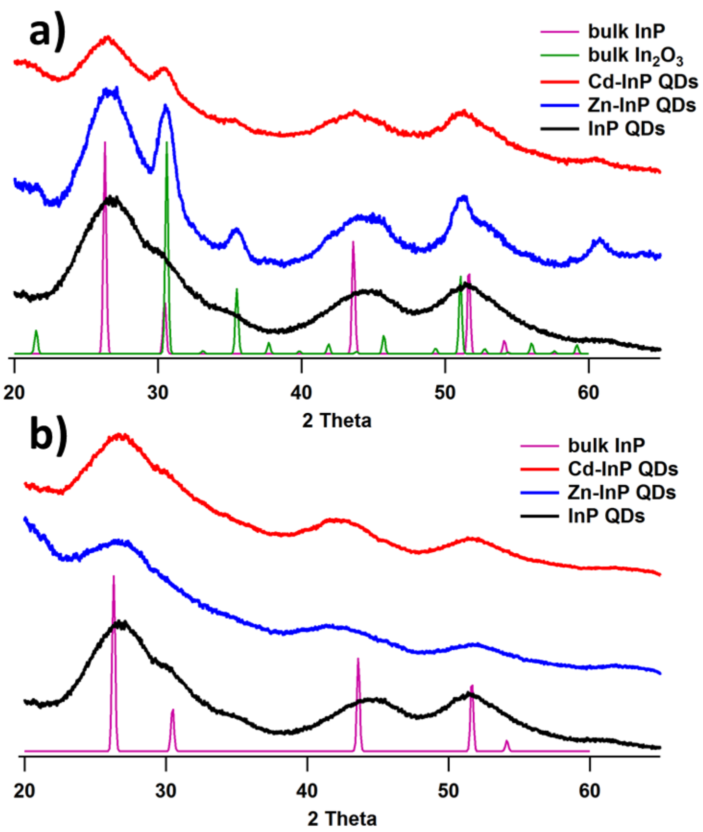

Figure 2.5. X-ray diffraction pattern of InP, Zn-InP, Cd-InP a) before filtering, b) after filtration through Celite, with bulk InP (pdf #01-070-2513 ICSD) and In_2O_3 (pdf #01-071-2194 ICSD).

The elemental composition of the as-prepared InP QDs and the Lewis acid-treated QDs were analyzed by inductively coupled plasma optical emission spectroscopy (ICP-OES). The molar ratios obtained for four different samples are shown in Table 2.1 along with a comparison of the initial M^{2+}:In ratios in the reaction. The initial molar ratios suggest the InP QDs have a stoichiometric core and an indium-rich surface. We hypothesize that the small increase of M^{2+}:In ratio in the purified samples as compared to the amount in the reaction itself confirms the displacement of $In(O_2CR)_3$, and consequent formation of In_2O_3 as M^{2+} carboxylates coordinate to the surface. The measured ratios indicate that the number of cations is in excess of what is needed to fully passivate the surface phosphorus atoms. In order to account for the large excess of M^{2+}, we additionally propose that the exogenous metal carboxylates form a disordered, interconnected surface coating given the diversity of binding modes possible.[27] This has been suggested previously for metal-rich II-VI QDs.[20,28]

Table 2.1. Molar ratios of M^{2+}:In:P added to the reaction and for purified products

	Reaction molar ratios (M^{2+}:In:P)	ICP molar ratios (M^{2+}:In:P)
InP	-	-:2:1
Cd-InP A	0.5:2:1	0.8:2:1
Cd-InP B	1:2:1	1.5:1.7:1
Zn-InP A	0.4:2:1	0.6:2:1
Zn-InP B	3:2:1	3.2:2:1

To better understand how metal carboxylates interact with InP, X-ray absorption spectra were collected in order to determine the coordination environment of In, Zn, and Cd. The indium K-edge spectra are identical in all samples indicating the local InP structure is largely retained (Figure 2.6). Extended X-ray absorption fine structure (EXAFS) data was used to examine the coordination environment of the M^{2+} ion in Zn-InP and Cd-InP. Qualitatively, examination of the EXAFS region demonstrates a contrast between InP QDs that feature a broad distribution of indium bound to phosphorous and oxygen (i.e. core and surface indium), and the Zn-InP and Cd-InP QDs that show Zn/Cd most likely exist in surface sites (Figure 2.7). The calculated bond distances and coordination numbers from EXAFS fitting results most closely resemble a combination of M—P and M—O bonding (Figure 2.8 and Table 2.2), consistent with surface-bound metal carboxylates. As the metal concentration in the purified sample increases, the ratio of

M—O: M—P increases (Table 2.2). This provides further evidence for a model of metal-passivated surface phosphorus atoms with excess metal carboxylates forming a disordered network with varied M—O binding modes.

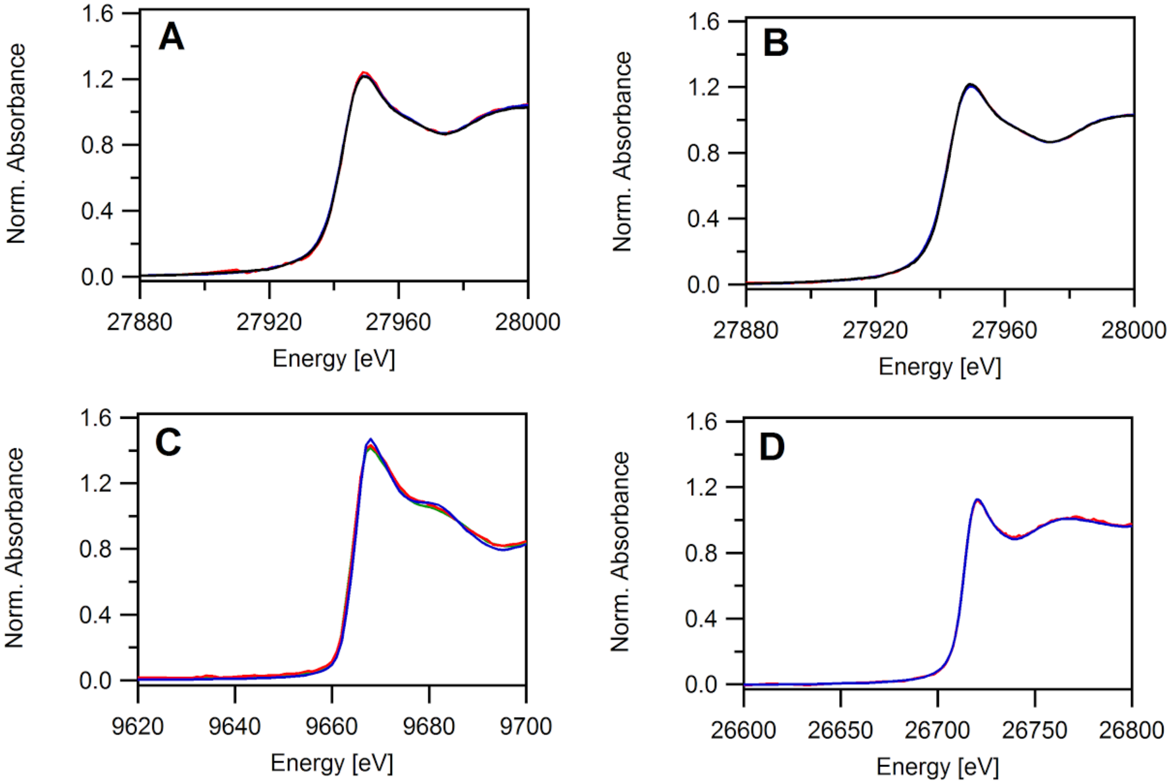

Figure 2.6. XANES region of InP with no(black), low (red), med (blue), high (green) amounts of cation added at the A) In K-edge for InP nanoparticles with Zn cations added. B) In K-edge for InP nanoparticles with Cd cations added. C) Zn K edge for InP nanoparticles with Zn cations added D) Cd K-edge for InP nanoparticles with Cd cations added.

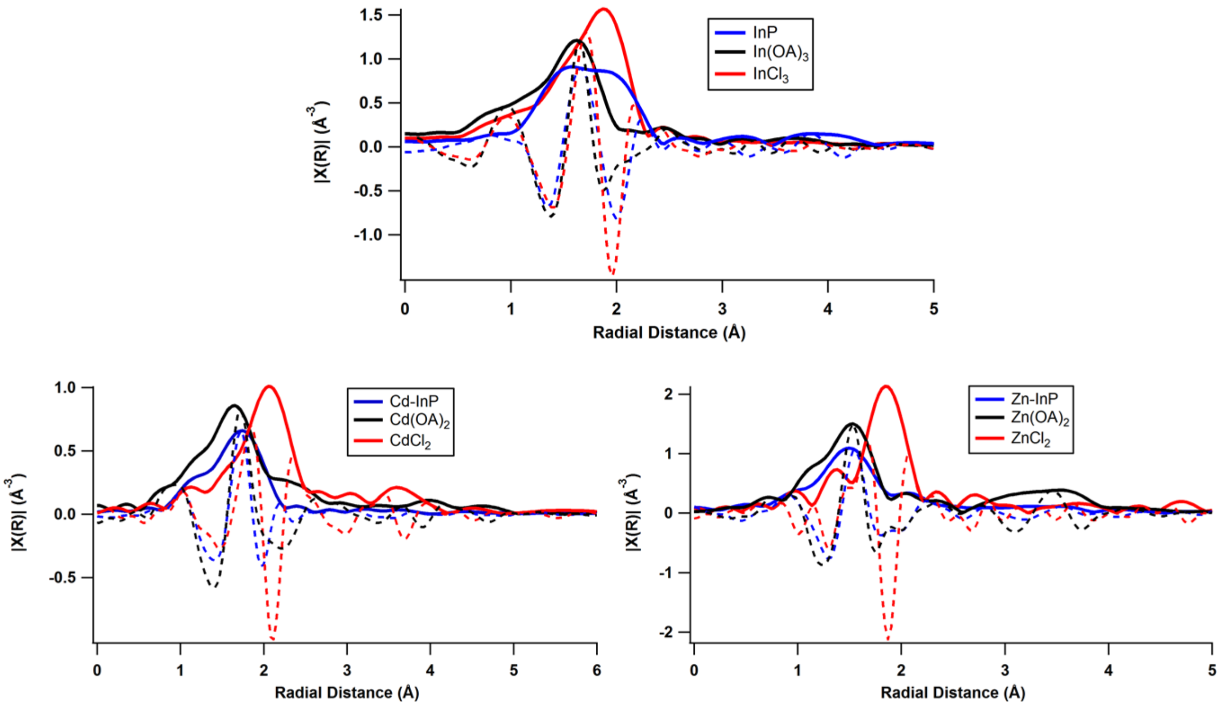

Figure 2.7. EXAFS Fourier Transform of (A) In K-edge of InP, (B) Cd K-edge, and (C) Zn K-edge. The metal chlorides are representative of metal phosphorous bond lengths. Metal oleates (OA) represent metal oxygen bond lengths.

Table 2.2. Results of EXAFS fitting.CN = coordination number, R = bond length, σ^2 = XAFS Debye-Waller factor, and E_0 = energy shift. *a: Two Zn-O bonds measured in zinc oleate standard and in Zn-InP QDs. We interpret the shorter bond length as a mixed O/P coordination environment.

Compound	Edge	Scatterer	EXAFS Fit			
			CN (±0.4)	R, Å (±0.02)	σ^2 (±0.0005)	E_0, eV (±0.2)
Zn-InP A	Zn-K	Zn-O (1)[a]	5.9	1.95	0.002	-5.1
		Zn-O (2)[a]	2.0	1.71	0.002	-7.6
		Zn-P	1.0	2.12	0.002	-7.9
	In-K	In-O	3.0	2.13	0.0008	-1.1
		In-P	3.2	2.48	0.0016	4.1
Cd-InP A	Cd-K	Cd-O	3.47	2.30	0.038	-8.67
		Cd-P	2.52	2.43	0.0075	-9.47
	In-K	In-O	3.3	2.14	0.0008	0.34
		In-P	2.9	2.48	0.0016	2.90

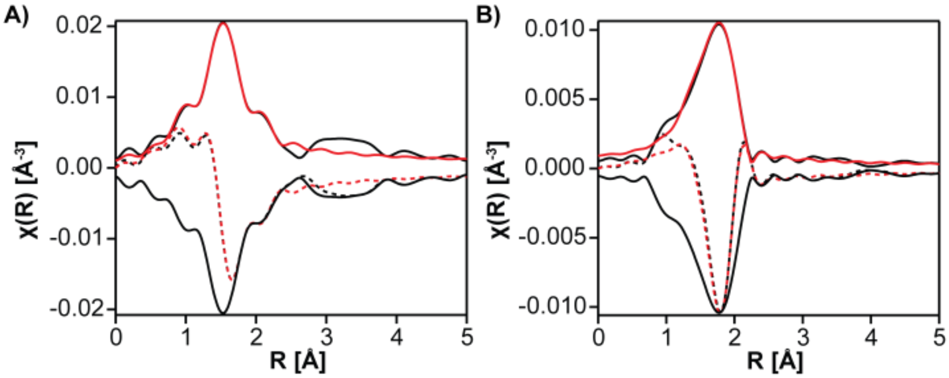

Figure 2.8. (A) Zn K-edge EXAFS region of Zn-InP and (B) Cd K-edge EXAFS region of Cd-InP. Experimental data (black) and quantitative fits (red) of the first coordination shell are shown for both the Fourier transform magnitude and inverse magnitude (—, solid lines) and imaginary components (---, dashed lines). Fitting parameters are provided in Table 2.2.

Chemical etching of the bound M^{2+} was attempted to confirm surface coordination between the cadmium and zinc carboxylates and InP. Owen *et al*. demonstrated the removal of Z-type ligands, $M(O_2CR)_2$, from CdSe nanocrystals using L-type Lewis bases.[20] They showed that N,N,N',N'-tetramethylethylene-1,2-diamine (TMEDA) displaces $Cd(O_2CR)_2$ from the surface of CdSe and hypothesized the formation of $(\kappa^2\text{-TMEDA})Cd(O_2CR)_2$. In analogy to the work by Owen *et al.*, addition of TMEDA to Cd-InP or Zn-InP QDs should serve to remove surface cadmium/zinc carboxylate, yield particles with lower photoluminescence, and shift the LEET back towards the original InP QD LEET maximum. We found that the QY of Zn-InP dropped from 18% to 4% and the LEET red shifted from 520 nm to 525 nm after addition of TMEDA (300 equiv. relative to [Zn]) to a solution of Zn-InP (Figure 2.9). Similarly, for Cd-InP the quantum yield dropped from 33% to 4% and the LEET blue-shifted from 528 nm to 522 nm after the addition of TMEDA (2600 equiv. relative to [Cd]) to a solution of Cd-InP. The difference between the concentrations of TMEDA necessary to quench PL in the two samples is consistent with an equilibrium binding model with interaction strength as predicted by Hard-Soft Acid-Base theory (HSAB); a greater excess of base may be necessary to disrupt the stronger cadmium-phosphorus interaction. Complete reversibility of the optical shifts was unachievable indicating either that some metal cations are strongly coordinated to the surface or minor alloying is occurring. Stern-Volmer analysis (Figure 2.10) shows nonlinearity in the PL as a function of TMEDA concentration in both cases, however the overall trend is consistent with a monotonic decrease in the overall luminescence intensity. Stern-Volmer analyses assume the interaction of a single quencher with the fluorophore and may not take into account the dynamic and complex nature of a quantum dot surface in which multiple quenching and fluorescence pathways exist.[29–31]

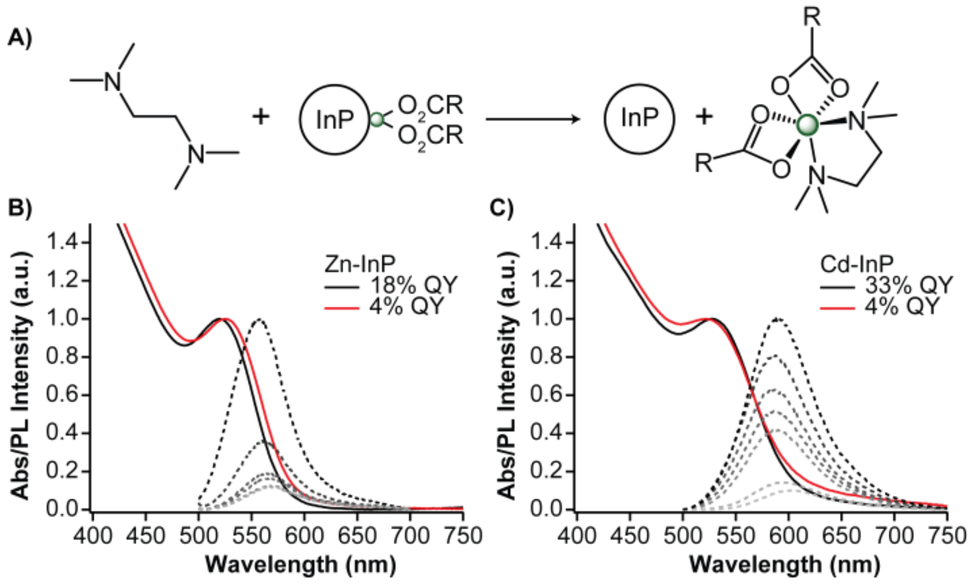

Figure 2.9. (A) Proposed reaction between TMEDA and surface metal carboxylates bound to InP QDs. The black (absorbance solid/PL dashed) traces are the Zn-InP (B) and Cd-InP (C) samples before adding Lewis base. As the concentration of TMEDA increases, the PL decreases and the absorbance shifts slightly (red solid) to resemble the original InP optical features.

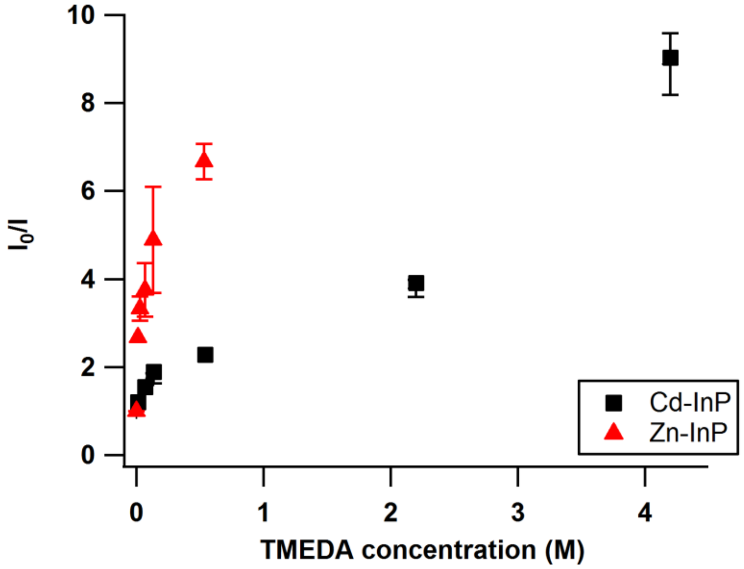

Figure 2.10. Stern-Volmer plot of PL quenching by formation of TMEDA-M(O_2CR)$_2$ complex

2.4 Conclusions

In summary, it is possible to both enhance the photoluminescence of InP QDs and tune the absorption and emission wavelengths using post-synthetic treatment with Lewis acids. Zinc oleate treated InP leads to quantum yields up to 19% while the addition of cadmium oleate results in quantum yields up to 49%. TEM, ICP, XAS, and chemical etching experiments have indicated that cadmium and zinc carboxylates predominantly displace native In^{3+} from the QD surface in order to bind to P and that this effect is largely responsible for the observed PL enhancement. A similar conclusion has been proposed by Nann and co-workers after they observed improved quantum yields (30%) of InP QDs that were synthesized by a single pot approach in which zinc carboxylates and hexadecylamine (HDA) are included in the initial InP core synthesis[14] rather than added post-synthetically as in this study. Although they hypothesize that the presence of zinc carboxylate molecules stay on the surface and confine excited electrons in the energy band, they also require the addition of HDA to observe QY's above 1% indicating that significant differences exist between these two synthetic approaches.

The origin of the optical shifts remains unresolved although we hypothesize that the QD LUMO may be significantly localized and hence its energy may be modified by the presence of surface-bound M^{2+}. Characterization methods surrounding ligand engineering of trap states in II-VI systems may be useful in the ongoing work to elucidate this phenomenon. The difference in the ability of the Lewis acids to enhance PL QY and bind the QD surface is proposed to be governed by HSAB theory but further examination of other metal ions will be essential in formulating a complete picture regarding the mechanism and scope of this effect. Importantly, the ability to color tune the luminescence of InP QDs post-synthetically without an associated change in particle size may offer a versatile new strategy to access chromophores for solid state lighting and display applications.

2.5 Experimental Methods

2.5.1 *General Considerations:*

All glassware was dried in a 160 °C oven overnight prior to use. All reactions, unless otherwise noted were run under an inert atmosphere of nitrogen using a glovebox or using standard Schlenk techniques. Indium acetate (99.99%), myristic acid (≥99%), tetrabutylammonium hydroxide (40 wt % in H_2O) and anhydrous oleic acid (99%) were purchased from Sigma-Aldrich Chemical Co. and used without further purification. Omni Trace nitric acid was purchased from EMD Millipore and used without further purification. 18.2 MΩ was collected from an EMD Millipore water purification system. Celite 545 was purchased from Sigma Aldrich Chemical Co. and heated at 150 °C under vacuum overnight and stored in a nitrogen glove box. All solvents, including 1-octadecene (≥95%), TMEDA (≥99.5%), toluene, pentane, ethyl acetate, and acetonitrile, were purchased from Sigma-Aldrich Chemical Co., dried over CaH_2, distilled, and stored over 4 Å molecular sieves in a nitrogen-filled glove box. C_6D_6 was purchased from Cambridge Isotope Labs and was similarly dried and stored. Diethyl zinc (95%) and dimethyl cadmium (97%) were purchased from Strem Chemicals and stored in a -35 °C freezer in a nitrogen-filled glove box. ^1H NMR spectra were collected on a 300 MHz Bruker Avance spectrometer. UV-Vis spectra were collected on a Cary 5000 spectrophotometer from Agilent. Fluorescence measurements were taken on a Horiba FL3021tau fluorescence spectrophotometer. Quantum yields were measured with a Hamamatsu integrating sphere. Powder XRD spectra were collected on a Bruker D8 Discover with GADDS 2-D XRD system. ICP-OES was performed using a Perkin Elmer Optima 8300. TEM images were collected on an FEI Tecnai G2 F20 microscope. Luminescence decay experiments were recorded on a PicoQuant FluoTime 100 instrument in a time-correlated single-photon-counting arrangement. $P(SiMe_3)_3$, zinc oleate, and tetrabutylammonium myristate were prepared following literature procedures.[32,33]

2.5.2 *Synthesis of InP Quantum Dot Stock Solution:*

InP QDs were synthesized following a modified preparation from Gary and Cossairt.[32] Briefly, indium acetate (4 mmol) and oleic acid (14.5 mmol) were heated at 100 °C overnight under reduced pressure in 1-octadecene (10 g). $P(SiMe_3)_3$ (2 mmol) was measured into 1-octadecene (4 g) and injected into the indium oleate at 315 °C. The temperature was lowered to 285 °C and particle growth was monitored by UV-Vis.

A known amount of InP solution was dried down to a powder and 15 mg ferrocene was added. The powder mixture was dissolved in C_6D_6 and a ^1H scan was run with a delay time of 20 seconds. The ferrocene peak at 4.0 ppm and the olefin resonance at 5.6 ppm were integrated and an approximate molar amount of indium was determined. The stock solutions had an average indium concentration of 0.2 M.

2.5.3 *Post-synthetic Modification of InP QDs*

Optimal experimental conditions (200 °C for 3 hours 2:1 Cd:In or 1.4:1 Zn:In) were determined by measuring the PL QY of M-InP stock solutions. Optimal concentrations of metal varied between batches of InP with different particle sizes. In a typical reaction, 250 μL of InP stock solution was dried and resuspended in 5 mL of 1-octadecene (ODE). The InP/ODE solution was injected into a flask containing zinc or cadmium oleate and heated up to 200 °C at a rate of 10-15 °C/minute with stirring. In order to measure absorbance and PLQY over time, aliquots were taken and injected into cuvettes containing anhydrous toluene prepared in the glovebox and sealed with a septum cap. After 3 hours, the flask was removed from the heating mantle and allowed to cool down. The solutions were purified as described in the supporting information document to remove unreacted metal carboxylates that would interfere with composition measurements. The solution was also filtered through Celite to remove any insoluble In_2O_3 particles. Variation with reaction conditions are shown in Figure S8.

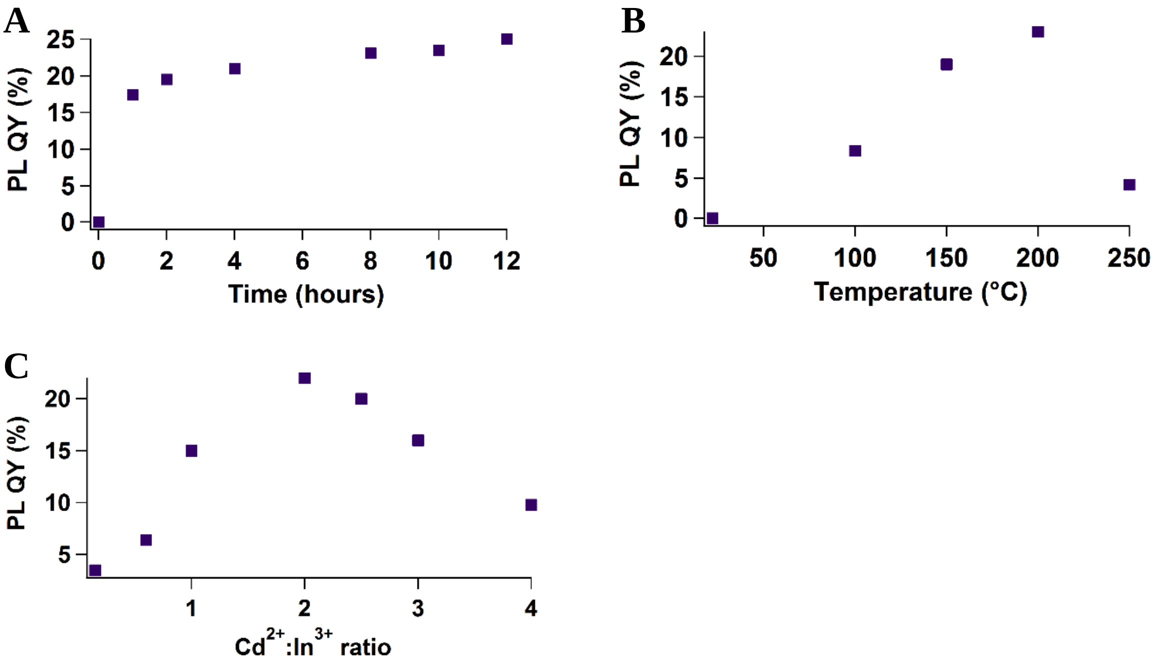

Figure 2.11. PL QY vs time (A), temperature (B), and amount of metal (C). The temperature was varied from 0-250 ˚C with a 2:1 Cd:In ratio present in each reaction. The PL was tracked over at least 4 hours at each temperature and the reaction at 200 ˚C was monitored over 12 hours. Cadmium oleate and zinc oleate ratios were varied at 200 ˚C and monitored over time.

2.5.4 *Ligand Removal Experiments*

A dried powder of each sample (20 mg InP, Zn-InP, and Cd-InP) was suspended in 15 mL toluene. In order to maintain QD concentration, aliquots were removed from these stock solutions and added to varying amounts of TMEDA and toluene. After each addition, the sample was stirred overnight to ensure equilibration of the reaction mixture. Aliquots were removed to measure UV-Vis and PL QY. TMEDA additions continued until the PL no longer changed. Formation of the (κ_2-TMEDA)M(O_2CR)$_2$ complex was associated with a sharpening of the olefin proton signal in the ^{1}H NMR spectrum.

2.5.5 *Sample Preparation for Characterization*

UV-Vis/Photoluminescence: All samples were aliquoted into dry toluene and kept at concentration values close to 0.1 absorbance due to the sensitivity of the fluorometer. Absolute quantum yields were measured with a Hamamatsu integrating sphere. *PL Decay:* A 470 nm LED with a pulse repetition rate of 500 KHz was used as the light source. The instrument response function (FWHM~1.4 ns) was collected by using a scatterer (non-dairy creamer). *ICP-OES:* An aliquot of QD solution was precipitated and centrifuged to collect solid powder. The supernatant was discarded and trace metal grade nitric acid (67%) was added to the powder and digested overnight. 18.2 MΩ was added to the sample to dilute to a total of 2% acid concentration. *TEM:* A few drops of QD solution was added to a 1:1 pentane:toluene solution. One drop of this was placed on a TEM grid (Ultrathin carbon on holey carbon support film, 400 mesh Ted Pella) and then put under vacuum overnight to remove any residual organic solvents. *XRD:* The worked up QD solution was centrifuged to provide a solid powder which was placed on a silicon <100> single crystal wafer piece as a solid paste.

2.5.6 *Scherrer Analysis*

The full-width half maximum (fwhm) of the In_2O_3 peak at 35.5 (2θ) was measured to determine the particle diameter by the following equation:[32]

$$L = \frac{0.9\lambda}{\Delta(2\theta)\cos(\theta_0)}$$

$$D = \frac{4}{3}L$$

2.5.7 *X-ray Absorption Spectroscopy*

Transmission and fluorescence X-ray absorption measurements at the Cd, In, and Zn K-edges were acquired at sector 10-BM, a bending magnet beamline that is part of the Materials Research Collaborative Access Team (MRCAT) at the Advanced Photon Source, Argonne, IL.[34] Photon energies were selected using a water-cooled, double-crystal Si(111) monochromator, which was detuned by approximately 50% to reduce harmonic reflections. The pure foils (Cd = 26713.3 eV, In = 27940.4 eV, Zn = 9660.76 eV)[35] were run concurrently with experimental samples and used for energy calibration. Measurements at the In K-edge used 5 vol% nitrogen in argon in the incident (I_o), transmission (I_t), and reference (I_{ref}) ionization chambers. Cd measurements used 15 vol% nitrogen in argon in I_o and 5 vol% nitrogen in argon in I_t and I_{ref}. Zn measurements used 40 vol% helium in nitrogen in I_o and 30 vol% argon in nitrogen in I_t and I_{ref}. Fluorescence signals were measured on a 4-element Vortex detector calibrated to a single elemental region of interest.

Fluorescence data points were acquired in five separate regions (energies relative to the elemental edge): a pre-edge region (-250 to -30 eV, 10 eV steps, dwell time = 0.25 s), the XANES region (-30 to -10 eV, 1 eV steps, dwell time = 0.25 s; and -10 to +30 eV, 0.5 eV steps, dwell time = 1 s), and the EXAFS region (2.8 $Å^{-1}$ to 6 $Å^{-1}$, 0.05 $Å^{-1}$ steps, dwell time = 0.7 s; 6 $Å^{-1}$ to 9 $Å^{-1}$, 0.05 $Å^{-1}$ steps, dwell time = 3 s; and 9 $Å^{-1}$ to 13 $Å^{-1}$, 0.05 $Å^{-1}$ steps, dwell time = 10 s). The detector settling time was 0.4 s prior to each measurement with a beam size of 1.2 mm × 0.5 mm. Signals from the four channels of the detector were summed for each scan, and at least three scans were taken per sample and averaged.

Reference spectra done in transmission mode had data points similarly acquired in five separate regions (energies relative to the elemental edge): a pre-edge region (-250 to -30 eV, 10 eV steps, dwell time = 0.5 s), the XANES region (-30 to -12 eV, 5 eV steps, dwell time = 0.5 s; and -12 to +30 eV, 0.5 eV steps, dwell time = 1 s), and the EXAFS region (2.8 $Å^{-1}$ to 6 $Å^{-1}$, 0.05 $Å^{-1}$ steps, dwell time = 0.7 s; 6 $Å^{-1}$ to 10 $Å^{-1}$, 0.05 $Å^{-1}$ steps, dwell time = 3 s; and 10 $Å^{-1}$ to 15 $Å^{-1}$, 0.05 $Å^{-1}$ steps, dwell time = 10 s). The detector settling time was 0.4 s prior to each measurement with a beam size of 0.5 mm × 0.5 mm. Three scans were taken per sample and averaged.

All sample manipulations were done in an argon-filled glovebox or glove bag. The solutions were then loaded into a PEEK cell (~ 1 cm path length) and sealed from exposure to air with a stainless steel Swagelok VCO fitting and removed from the glovebox.[36] Solid reference samples were prepared as dilute mixtures in BN containing 40% Cd or In or 13 wt% Zn. Mixtures (~ 50-100 mg) were homogenized with a mortar and pestle. A 10-15 mg aliquot was then loaded into a 4 mm diameter cylindrical stainless-steel holder and hand pressed into a self-supporting pellet. The holder was sealed in a quartz tube with kapton windows. Samples were then placed in the beamline mounted on a Parker X, Y, Z stage with µm directional resolution. An X,Y positional scan at a single energy was used to optimize the sample position.

Spectra were calibrated to the pure foil and normalized using standard procedures in Athena.[37] Edge positions were determined by locating the maximum of the first peak in the first derivative spectrum. EXAFS quantitative fitting of the first coordination sphere was done in WinXAS using the phase shifts and backscattering amplitudes from external experimental references.[38] Reference compounds (run as solids) were Na_2PdCl_4 (CN = 4 at 2.31 Å)[39] for Cd-P/Cl scatterers, 2-3 nm PdO particles (CN = 4 at 2.05 Å)[40] for Cd-O scatterers, bulk ZnO (CN = 4 at 1.98 Å)[41,42] for Zn-O scatterers, and anhydrous $ZnCl_2$ (CN = 4 at 2.05 Å)[43] for Zn-P scatterers. Indium reference compounds were $InCl_3$ (CN = 6 at 2.42 Å)[44,45] and In(Myristate)$_3$ (CN = 6 at 2.18 Å)[46]. The coordination numbers and distances were confirmed by independent fits with the

Pd references mentioned above. The EXAFS coordination parameters were obtained by a simultaneous least-squares fit in R-space of the first shell M–O/P k^2 and k-weighted Fourier-transformed data with $\Delta k = 2.43\text{-}11.1$ Å^{-1} and $\Delta R = 0.9 – 2.4$ Å. Higher-shell and multiple-scatterer scattering paths consistent with the longer-range M–C distances of the capping ligands are observed but have not been quantitatively fit.

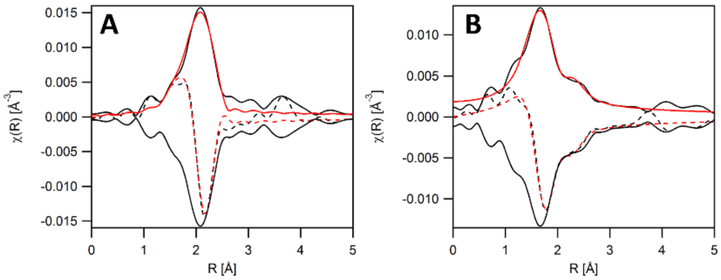

Figure 2.12. Cd K-edge EXAFS region of A) $CdCl_2$ and B) $Cd(OAc)_2•2H_2O$ as room temperature solid in BN. Experimental data (black) and quantitative fits (red) of the first coordination shell are shown for both the fourier transform magnitude and inverse magnitude (—, solid lines) and imaginary components (---, dashed lines).

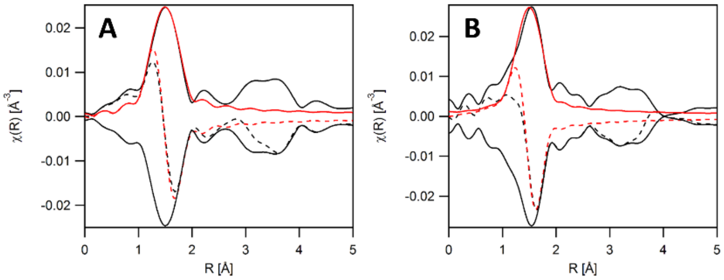

Figure 2.13. Zn K-edge EXAFS region of A) $Zn(OAc)_2•2H_2O$ and B) $Zn(Oleate)_2•2H_2O$as room temperature solid in BN. Experimental data (black) and quantitative fits (red) of the first coordination shell are shown for both the fourier transform magnitude and inverse magnitude (—, solid lines) and imaginary components (---, dashed lines).

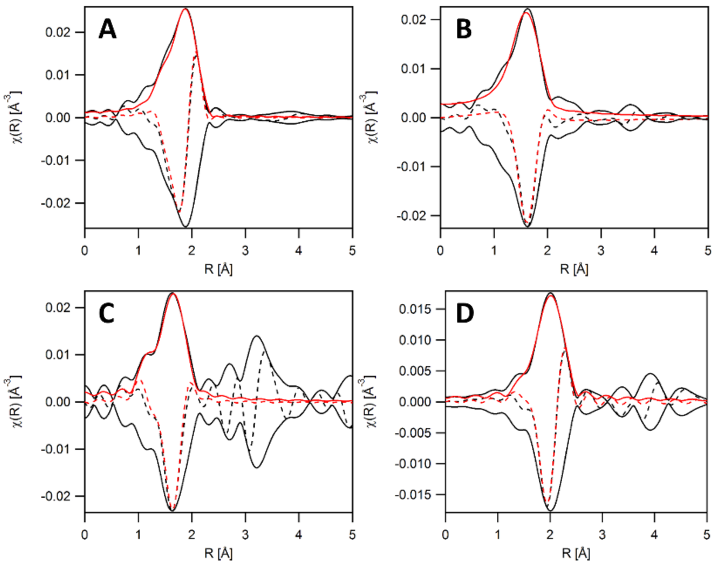

Figure 2.14. In K-edge EXAFS region of A) $InCl_3$ B) In(Myristate)$_3$ C) In_2O_3 and D) bulk InP as room temperature solid in BN. Experimental data (black) and quantitative fits (red) of the first coordination shell are shown for both the fourier transform magnitude and inverse magnitude (—, solid lines) and imaginary components (---, dashed lines).

Table 2.3. EXAFS fitting results for molecular compound solids in BN. These compounds were used to verify the choice of experimental reference.

Compound	Edge	Scatterer[a]	EXAFS Fit				Crystal Structure	
			CN (±0.4)	**R, Å (±0.02)**	**σ^2 (± 0.0005)**	**E0, eV (± 0.2)**	**CN**	**R, Å**
$CdCl_2$	Cd-K	Cd-Cl	6	2.62	0.009	-4.41	6	2.67 ± 0.04[b]
$Cd(OAc)_2 \bullet 2H_2O$	Cd-K	Cd-O	5	2.28	0.0164	-7.55	5	2.30 ± 0.01[c]
		Cd-O	2	2.63	0.0184	1.09	2	2.57 ± 0.04[c]
$Zn(OAc)_2 \bullet 2H_2O$	Zn-K	Zn-O	5.6	2.00	0.0087	-2.81	6	2.1 ± 0.1[d]
$Zn(Oleate)_2 \bullet 2H_2O$	Zn-K	Zn-O	5.1	1.94	0	-2.78	--	--
$InCl_3$	In-K	In-Cl	6.0	2.42	0.0045	-8.87	6	2.42[e]
$In(Myristate)_3$	In-K	In-O	5.5	2.18	0.0104	-8.49	6	2.18[f]
$In(OAc)_3$	In-K	In-O	5.8	2.17	0.0086	-7.2	--	--
In_2O_3	In-K	In-O	6.0	2.19	-0.0015	1.14	6	2.18[f]
Bulk InP	In-K	In-P	3.8	2.52	0.0023	-3.01	4	

[a] Fit results using single-shell standard. Where multiple scatterers are listed for the same molecule at the same edge, all single shells listed were refined simultaneously. Cd-Cl and In-Cl/P fit with experimental Pd-Cl scatterer. Cd-O fit with Pd-O scatterer. In-O fit with $In(MA)_3$ In-O experimental reference. $In(MA)_3$ coordination confirmed by independent fit with Pd-O scatterer. [b] Crystallographic distances reported in reference 47.[47] [c] Crystallographic distances reported in reference 48.[48] [d] Crystallographic distances reported in reference 49.[49] [e] Crystallographic unit cell reported in reference 47.[47] Typical In-Cl bond distances from reference 48.[48] [f] Crystallographic distances reported in reference 49.[49]

2.6 References

(1) Bardsley Consulting; Navigant Consulting, I. . R. A., Inc. .. SB Consulting; SSL Services, Inc. Solid-State Lighting Research and Development: Multi-Year Program Plan. **2012**.

(2) Navigant Consulting, I. Energy Savings Potential of SSL in General Illumination Applications 2010 to 2030. **2010**.

(3) Mushonga, P.; Onani, M. O.; Madiehe, A. M.; Meyer, M. Indium Phosphide-Based Semiconductor Nanocrystals and Their Applications. *J. Nanomater.* **2012**, *2012*, 1–11.

(4) Hens, Z.; Moreels, I. Light Absorption by Colloidal Semiconductor Quantum Dots. *J. Mater. Chem.* **2012**, *22* (21), 10406–10415.

(5) R. Heath, J. Covalency in Semiconductor Quantum Dots. *Chem. Soc. Rev.* **1998**, *27* (1), 65–71.

(6) McKittrick, J.; Shea-Rohwer, L. E. Review: Down Conversion Materials for Solid-State Lighting. *J. Am. Ceram. Soc.* **2014**, *97* (5), 1327–1352.

(7) Anc, M. J.; Pickett, N. L.; Gresty, N. C.; Harris, J. A.; Mishra, K. C. Progress in Non-Cd Quantum Dot Development for Lighting Applications. *ECS J. Solid State Sci. Technol.* **2013**, *2* (2), 3071–3082.

(8) Micic, O. I.; Sprague, J.; Lu, Z.; Nozik, A. J. Highly Efficient Band Edge Emission from InP Quantum Dots. *Appl. Phys. Lett.* **1996**, *68* (22), 3150–3152.

(9) Adam, S.; Talapin, D. V.; Borchert, H.; Lobo, A.; McGinley, C.; de Castro, A. R. B.; Haase, M.; Weller, H.; Möller, T. The Effect of Nanocrystal Surface Structure on the Luminescence Properties: Photoemission Study of HF-Etched InP Nanocrystals. *J. Chem. Phys.* **2005**, *123* (8), 084706–084710.

(10) Mićić, O. I.; Nozik, A. J.; Lifshitz, E.; Rajh, T.; Poluektov, O. G.; Thurnauer, M. C. Electron and Hole Adducts Formed in Illuminated InP Colloidal Quantum Dots Studied by Electron Paramagnetic Resonance. *J. Phys. Chem. B* **2002**, *106* (17), 4390–4395.

(11) Tamang, S.; Lincheneau, C.; Hermans, Y.; Jeong, S.; Reiss, P. Chemistry of InP Nanocrystal Syntheses. *Chem. Mater.* **2016**, *28* (8), 2491–2506.

(12) Li, L.; Reiss, P. One-Pot Synthesis of Highly Luminescent InP/ZnS Nanocrystals without Precursor Injection. *J. Am. Chem. Soc.* **2008**, *130* (35), 11588–11589.

(13) Xi, L.; Cho, D.-Y.; Duchamp, M.; Boothroyd, C. B.; Lek, J. Y.; Besmehn, A.; Waser, R.; Lam, Y. M.; Kardynal, B. Understanding the Role of Single Molecular ZnS Precursors in the Synthesis of In(Zn)P/ZnS Nanocrystals. *ACS Appl. Mater. Interfaces* **2014**, *6* (20), 18233–18242.

(14) Xu, S.; Ziegler, J.; Nann, T. Rapid Synthesis of Highly Luminescent InP and InP/ZnS Nanocrystals. *J. Mater. Chem.* **2008**, *18* (23), 2653–2656.

(15) Ryu, E.; Kim, S.; Jang, E.; Jun, S.; Jang, H.; Kim, B.; Kim, S.-W. Step-Wise Synthesis of InP/ZnS Core−Shell Quantum Dots and the Role of Zinc Acetate. *Chem. Mater.* **2009**, *21* (4), 573–575.

(16) Thuy, U. T. D.; Reiss, P.; Liem, N. Q. Luminescence Properties of In(Zn)P Alloy Core/ZnS Shell Quantum Dots. *Appl. Phys. Lett.* **2010**, *97* (19), 193104.

(17) Haubold, S.; Haase, M.; Kornowski, A.; Weller, H. Strongly Luminescent InP/ZnS Core–Shell Nanoparticles. *ChemPhysChem* **2001**, *2* (5), 331–334.

(18) Huang, K.; Demadrille, R.; Silly, M. G.; Sirotti, F.; Reiss, P.; Renault, O. Internal Structure of InP/ZnS Nanocrystals Unraveled by High-Resolution Soft X-Ray Photoelectron Spectroscopy. *ACS Nano* **2010**, *4* (8), 4799–4805.

(19) Park, J. K., Sunghoon; Kim, Sungwoo; Yu, Seung Tack; Lee, Bunyeoul; Kim, Sang-Wook. Fabrication of Highly Luminescent InP/Cd and InP/CdS Quantum Dots. *J. Lumin.* **2010**, *130*, 1825–1828.

(20) Anderson, N. C.; Hendricks, M. P.; Choi, J. J.; Owen, J. S. Ligand Exchange and the Stoichiometry of Metal Chalcogenide Nanocrystals: Spectroscopic Observation of Facile Metal-Carboxylate Displacement and Binding. *J. Am. Chem. Soc.* **2013**, *135* (49), 18536–18548.

(21) Allen, P. M.; Walker, B. J.; Bawendi, M. G. Mechanistic Insights into the Formation of InP Quantum Dots. *Angew. Chem. Int. Ed.* **2010**, *49* (4), 760–762.

(22) Franke, D.; Harris, D. K.; Xie, L.; Jensen, K. F.; Bawendi, M. G. The Unexpected Influence of Precursor Conversion Rate in the Synthesis of III–V Quantum Dots. *Angew. Chem. Int. Ed.* **2015**, *54* (48), 14299–14303.

(23) Xie, R.; Battaglia, D.; Peng, X. Colloidal InP Nanocrystals as Efficient Emitters Covering Blue to Near-Infrared. *J. Am. Chem. Soc.* **2007**, *129* (50), 15432–15433.

(24) Adam, S.; McGinley, C.; Möller, T.; Talapin, D. V.; Borchert, H.; Haase, M.; Weller, H. Photoemission Study of Size Selected InP Nanocrystals: The Relationship between Luminescence Yield and Surface Structure. *Eur. Phys. J. - At. Mol. Opt. Plasma Phys.* **2003**, *24* (1), 373–376.

(25) Kim, S.; Kim, T.; Kang, M.; Kwak, S. K.; Yoo, T. W.; Park, L. S.; Yang, I.; Hwang, S.; Lee, J. E.; Kim, S. K.; et al. Highly Luminescent InP/GaP/ZnS Nanocrystals and Their Application to White Light-Emitting Diodes. *J. Am. Chem. Soc.* **2012**, *134* (8), 3804–3809.

(26) Narayanaswamy, A.; Xu, H.; Pradhan, N.; Kim, M.; Peng, X. Formation of Nearly Monodisperse In2O3 Nanodots and Oriented-Attached Nanoflowers: Hydrolysis and Alcoholysis vs Pyrolysis. *J. Am. Chem. Soc.* **2006**, *128* (31), 10310–10319.

(27) Curtiss, A. B. S.; Bera, M.; Musie, G. T.; Powell, D. R. Synthesis and Characterization of Mono- and [Small Mu]6-Sulfato Hexanuclear Zinc Complexes of a New Symmetric Dinucleating Ligand. *Dalton Trans.* **2008**, No. 20, 2717–2724.

(28) Frederick, M. T.; Achtyl, J. L.; Knowles, K. E.; Weiss, E. A.; Geiger, F. M. Surface-Amplified Ligand Disorder in CdSe Quantum Dots Determined by Electron and Coherent Vibrational Spectroscopies. *J. Am. Chem. Soc.* **2011**, *133* (19), 7476–7481.

(29) Landes, C.; Burda, C.; Braun, M.; El-Sayed, M. A. Photoluminescence of CdSe Nanoparticles in the Presence of a Hole Acceptor: N-Butylamine. *J. Phys. Chem. B* **2001**, *105* (15), 2981–2986.

(30) Chambrier, I.; Banerjee, C.; Remiro-Buenamañana, S.; Chao, Y.; Cammidge, A. N.; Bochmann, M. Synthesis of Porphyrin–CdSe Quantum Dot Assemblies: Controlling Ligand Binding by Substituent Effects. *Inorg. Chem.* **2015**, *54* (15), 7368–7380.

(31) Morris-Cohen, A. J.; Vasilenko, V.; Amin, V. A.; Reuter, M. G.; Weiss, E. A. Model for Adsorption of Ligands to Colloidal Quantum Dots with Concentration-Dependent Surface Structure. *ACS Nano* **2012**, *6* (1), 557–565.

(32) Glassy, B. A.; Cossairt, B. M. Ternary Synthesis of Colloidal Zn3P2 Quantum Dots. *Chem. Commun.* **2015**, *51*, 5283–5286.

(33) Gary, D. C.; Cossairt, B. M. Role of Acid in Precursor Conversion During InP Quantum Dot Synthesis. *Chem. Mater.* **2013**, *25* (12), 2463–2469.

(34) Kropf, A. J.; Katsoudas, J.; Chattopadhyay, S.; Shibata, T.; Lang, E. A.; Zyryanov, V. N.; Ravel, B.; McIvor, K.; Kemner, K. M.; Scheckel, K. G.; et al. The New MRCAT (Sector 10) Bending Magnet Beamline at the Advanced Photon Source. *AIP Conf. Proc.* **2010**, *1234* (1), 299–302.

(35) Kraft, S.; Stümpel, J.; Becker, P.; Kuetgens, U. High Resolution X-ray Absorption Spectroscopy with Absolute Energy Calibration for the Determination of Absorption Edge Energies. *Rev. Sci. Instrum.* **1996**, *67* (3), 681–687.

(36) Nelson, R. C.; Miller, J. T. An Introduction to X-Ray Absorption Spectroscopy and Its in Situ Application to Organometallic Compounds and Homogeneous Catalysts. *Catal. Sci. Technol.* **2012**, *2* (3), 461–470.

(37) Ravel, B.; Newville, M. ATHENA, ARTEMIS, HEPHAESTUS: Data Analysis for X-Ray Absorption Spectroscopy Using IFEFFIT. *J. Synchrotron Radiat.* **2005**, *12* (Pt 4), 537–541.

(38) Ressler, T. WinXAS: A Program for X-Ray Absorption Spectroscopy Data Analysis under MS-Windows. *J. Synchrotron Radiat.* **1998**, *5* (Pt 2), 118–122.

(39) Fábry, J.; Krupková, R.; Vaněk, P.; Dušek, M.; Němec, I. Bis-(Tetra-methyl-ammonium) Tetra-chloro-palladate(II). *Acta Crystallogr. Sect. E 60* (7), m924–m926.

(40) Lei, Y.; Lu, J.; Zhao, H.; Liu, B.; Low, K.-B.; Wu, T.; Libera, J. A.; Greeley, J. P.; Chupas, P. J.; Miller, J. T.; et al. Resolving Precursor Deligation, Surface Species Evolution, and Nanoparticle Nucleation during Palladium Atomic Layer Deposition. *J. Phys. Chem. C* **2013**, *117* (21), 11141–11148.

(41) Vlaic, G.; Williams, C. E.; Jérome, R.; Tant, M. R.; Wilkes, G. L. Microstructure of the Ionic Aggregates in Telechelic Ionomers. *Polymer* **1988**, *29* (1), 173–176.

(42) Roberts, D. R.; Ford, R. G.; Sparks, D. L. Kinetics and Mechanisms of Zn Complexation on Metal Oxides Using EXAFS Spectroscopy. *J. Colloid Interface Sci.* **2003**, *263* (2), 364–376.

(43) Calligaris, M. Structural Inorganic Chemistry by A. F. Wells. *Acta Crystallogr. B* **1985**, *41* (3), 208–208.

(44) Rabinovich, D. Advanced Inorganic Chemistry, 6th Edition (Cotton, F. A.; Wilkinson, G.; Murillo, C. A.; Bochmann, M.). *J. Chem. Educ.* **2000**, *77* (3), 311.

(45) Jin, S.; McKee, V.; Nieuwenhuyzen, M.; Robinson, W. T.; Wilkins, C. J. Evidence on Ligand Strengths from the Crystal Structures of [InCl3(Dmf)3], [InCl3(Dma)3], [{InCl3(PhCHO)3}2]·PhCHO and [InCl3(PhCOMe)2] from Dimethylformamide (Dmf), Dimethylacetamide (Dma), Benzaldehyde and Acetophenone. *J. Chem. Soc. Dalton Trans.* **1993**, *0* (20), 3111–3116.

(46) Marezio, M. Refinement of the Crystal Structure of In2O3 at Two Wavelengths. *Acta Crystallogr. 20* (6), 723–728.

(47) Voet, A. R. D.; Noguchi, H.; Addy, C.; Zhang, K. Y. J.; Tame, J. R. H. Biomineralization of a Cadmium Chloride Nanocrystal by a Designed Symmetrical Protein. *Angew. Chem. Int. Ed Engl.* **2015**, *54* (34), 9857–9860.

(48) Harrison, W.; Trotter, J. Crystal and Molecular Structure of Cadmium Diacetate Dihydrate. *J. Chem. Soc. Dalton Trans.* **1972**, *0* (8–9), 956–960.

(49) Ishioka, T.; Murata, A.; Kitagawa, Y.; Nakamura, K. T. Zinc(II) Acetate Dihydrate. *Acta Crystallogr. C* **1997**, *53* (8), 1029–1031.

Chapter 3. Probing Surface Defects of InP Quantum Dots Using Phosphorus Kα and Kβ X-ray Emission Spectroscopy

3.1 Note for Collaborative Work

This work was performed in collaboration with William Holden, a graduate student working under Professor Gerald Seidler in the Department of Physics at the University of Washington. They developed and built a benchtop X-ray emission spectrometer that enabled these measurements that would typically require a synchrotron source. All XES measurements and XES spectra fits and analyses were performed by Will Holden. I am especially grateful to Will for valuable discussion and his willingness to restrain himself from re-fitting the data at least ten times. Furthermore, I am indebted to Amrit Venkatesh, a graduate student working under Professor Aaron Rossini in the Department of Chemistry at Iowa State University, who was responsible for collecting all the solid-state NMR data. I have run these types of acquisitions before, but without a dedicated solids instrument in the UW NMR facility, running scans for 30 consecutive days would have been a difficult feat.

3.2 Introduction

Indium phosphide (InP) quantum dots (QDs) are the leading cadmium-free emissive material for luminescence downconversion applications, such as LED-backlit displays, and lighting technologies.[1–5] Display manufacturers including Samsung, Sony, Vizio, LG, and Apple have devoted significant resources to investigating methods to narrow the size distributions of InP QD samples and increase the photoluminescence quantum yields (PL QYs) up to 100%.[6] Despite these efforts, state-of-the-art syntheses produce QD ensembles that are characterized by luminescence linewidths in the green and red region that range between 40-80 nm and quantum yields that max out at 85% in the most sophisticated shelled samples.[7–9] While minimizing defects in the core and shell materials is necessary, perhaps the most crucial aspect of design is at the core-shell interface. InP QDs have been shown to be incredibly susceptible to surface oxidation from *in-situ* and *ex-situ* sources during both core and shell syntheses, resulting in oxidized phosphorus species that likely perturb conformal shell growth.[10–12] We hypothesize that surface phosphorus oxidation plays a leading role in limiting our ability to access higher quality samples.

Even under synthetic conditions in which extreme care is taken to exclude oxygen and water, surface phosphorus oxidation often arises as the result of undesired side-reactions that occur during the nucleation, growth, and shelling of InP QDs. Although there has been debate concerning the potential benefits of an amorphous oxidized interface between an InP core and its shell material with respect to reducing lattice strain between materials,[13,14] the detrimental impact of water on particle nucleation and growth has directed efforts towards removing any source of surface oxidation.[15–17] Furthermore, oxidized phosphorus that is present at the core-shell interface may serve as an electronic trap site or prevent conformal deposition of shell material, both of which have the effect of reducing PL QYs. In this study, we chose three different synthetic methods that are expected to produce InP QDs with minimal or no oxidation. Furthermore, each InP QD sample prepared with these methods was shelled with either ZnS or ZnSe with the hypothesis that samples that are initially more oxidized or that are subjected to processes that oxidize the surface will result in particles with lower PL QYs.

X-ray photoelectron spectroscopy (XPS) and magic angle spinning solid-state NMR (MAS SSNMR) spectroscopy have been the traditional routes to measure the degree of oxidized phosphorus present in InP quantum dots.[11–13,17–19] These measurements can be challenging due to the low sensitivity of SSNMR spectroscopy which traditionally require large amounts of sample and long acquisition times. XPS analysis is generally impeded by its surface-sensitive nature and the presence of common long-chain surface ligands that further limit the escape depth of the photogenerated electrons and reduce the signal resolution.[20] Extremely high energy resolution wavelength dispersive X-ray fluorescence spectroscopy, more commonly called X-ray emission spectroscopy (XES), is an appealing alternative method for characterizing the oxidation of phosphorus in a bulk sample because it does not face these obstacles. Recent progress in benchtop XES instrumentation holds the potential to develop XES of sulfur and phosphorus into an accessible and powerful technique for probing oxidation state and bonding electronic structure, achieving synchrotron-level energy resolution and count rates with a spectrometer illuminated by only a conventional X-ray tube.[21] The same instrument was used in a recent study of sulfur speciation in biochars as a first analytical application,[22] and the present study reinforces and, in many ways, exceeds the message of that earlier work in emphasizing new potential for XES for routine application in analytical chemistry.

A number of recent studies have demonstrated the capability of synchrotron and laboratory-based XES to measure speciation in phosphorus, sulfur, and chlorine compounds.[22–27] In particular, P Kα XES has been used to quantitatively determine the fraction of phosphorus species with different local charge densities (i.e. oxidation states). The Kα emission line corresponds to a transition of an electron between the deep, atomic-like 2p and 1s orbitals. In the simplest treatment, the sensitivity of this transition to changes in the valence electron population comes from the different changes in the screening of the nuclear charge as observed from the 2p and 1s orbitals. As these effects are only weakly perturbative for phosphorus (but can be much more complex for, e.g., 3d transition metals) the Kα emission spectra typically show only a shift of the peak position from lower to higher energy with increasing oxidation state, while the spectral shape remains unchanged (Figure 3.1). For a compound containing phosphorus in multiple oxidation states, the proportion of each oxidation state can be determined quantitatively by simple linear-combination fitting to multiple line shapes, although this benefits from prior knowledge of a suitable reference spectrum set.

For information beyond oxidation state determination by the P Kα emission, P Kβ XES enables a more detailed interrogation of the electronic structure. The Kβ emission line results from electronic transitions from the 3p shell, suitably hybridized with valence and semi-core ligand electrons, to the 1s core hole. Due to the direct relevance of such a characterization of the bonding electronic density of states for chemistry, this type of valence to core (VTC) XES is seeing growing use, such as in studies of organometallic systems.[28–31] Thus, the Kβ emission has increased chemical sensitivity and can provide information about bonding, symmetry, and ligand type.[24] A full interpretation of the various spectral features requires quantum chemistry calculations.[24,28,32,33] Here, we focus on the ligand fingerprinting capability of the Kβ spectral features, specifically the Kβ' satellite feature near 2123.5 eV in the phosphate spectrum. This feature results from mixing of P valence states with an O 2s orbital,[24,34] and thus serves as a clear indicator of the presence of phosphate. P Kβ spectra are shown for reference compounds in Figure 3.1.

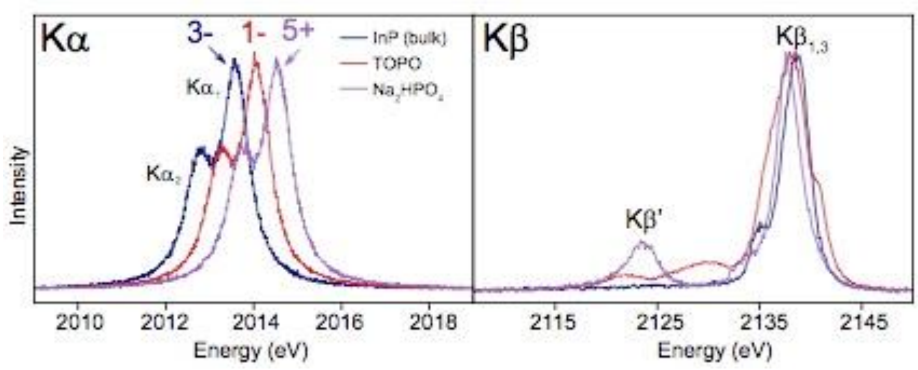

Figure 3.1. P Kα and Kβ X-ray emission spectra of reference compounds. The Kα spectra of the three compounds are nearly identical, with shifts in energy towards higher energy with increasing oxidation state. Nominal oxidation states of the reference compounds are indicated above the given spectra. The Kβ spectra is a valence to core transition, and a number of different spectral features are observed. Of particular importance is the strong Kβ' peak at 2123.5 eV in the Na_2HPO_4 spectra, which is due to mixing of the P 3p and O 2s orbitals, and thus serves as a fingerprint of P–O bonds from the phosphate.

3.3 Results and Discussion

To validate the use of Kα XES as a method to determine P speciation in InP QDs, a series of three samples was used in a head-to-head comparison of oxidation state distributions inferred from P Kα XES and from ^{31}P MAS SSNMR. Notably the InP and InP/ZnS samples have in part been previously characterized by Chaudret *et al*. via XPS and SSNMR spectroscopies with the primary conclusion that oxidation occurs during both synthesis and shell growth.[12] Here, samples including InP QDs, InP QDs that have been post-synthetically treated with zinc (InP/Zn), and InP QDs that have been shelled with ZnS (InP/ZnS) were studied. The results for all samples are presented in Table 3.4 and a comparison of the quantification of phosphorus oxidation state by both ^{31}P SSNMR and P Kα X-ray emission spectroscopy for the InP/ZnS sample is shown in Figure 3.2. Additional spectra are presented in Figure 3.3. Excellent agreement is found between the two techniques, and the results fall within the range of values reported by Chaudret *et al*.[12] The ^{31}P SSNMR spectra generally show resonances centered at ca. 0 ppm, assigned to oxidized phosphate species, and –200 ppm, assigned to the core phosphide species. Cross polarization magic angle spinning (CP-MAS) and direct excitation ^{31}P SSNMR experiments have previously demonstrated that the oxidized phosphorus species are located at the surface of the nanocrystals.[35,36] Using the fitting procedure described in the Experimental section, the P Kα XES signal for each of the three samples is fit well using two oxidation state components, one with an average $K\alpha_1$ energy position of 2013.56 eV identified as InP and one higher in energy with an average position of 2014.41 eV. Although the SSNMR identifies the oxidized species as phosphate-like, the $K\alpha_1$ energy position is somewhat lower in energy than that of the disodium phosphate reference standard used (2014.55 eV). Though phosphides and sulfides are known to have small shifts in the $K\alpha_1$ energy position due to differing degrees of covalency,[24,25] this has not previously been observed in phosphates or sulfates and could be worthy of future investigation. That being said, with the identification of phosphate from the SSNMR resonance at ca. 0 ppm and the agreement between the SSNMR and XES results, this confirms the oxidized component at 2014.41 eV corresponds to phosphate.

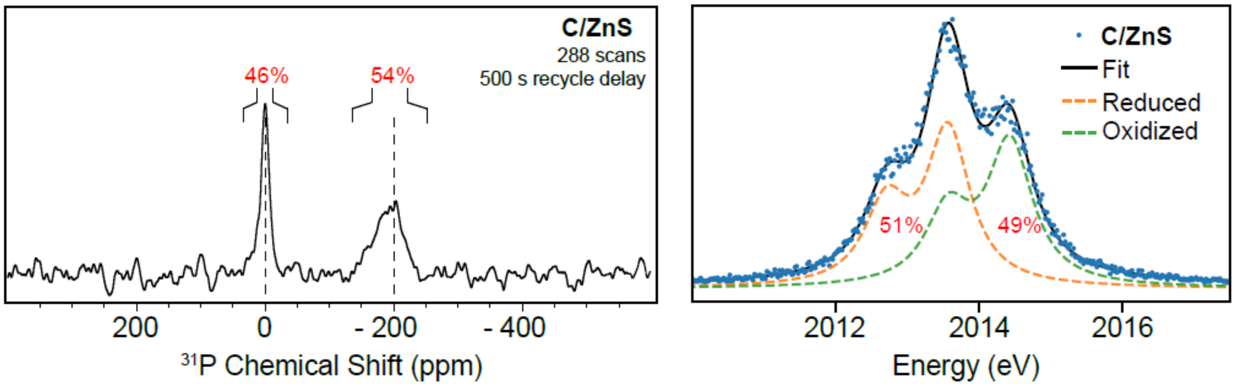

Figure 3.2. Comparison of ^{31}P SSNMR spectrum (left) and P Kα XES (right) of the same batch of InP/ZnS QDs. The SSNMR signal near 0 ppm corresponds to surface phosphate, and this component shows up at a $K\alpha_1$ energy position of ~2014.41 eV. The relative peak areas in both types of spectra are indicated as percentages.

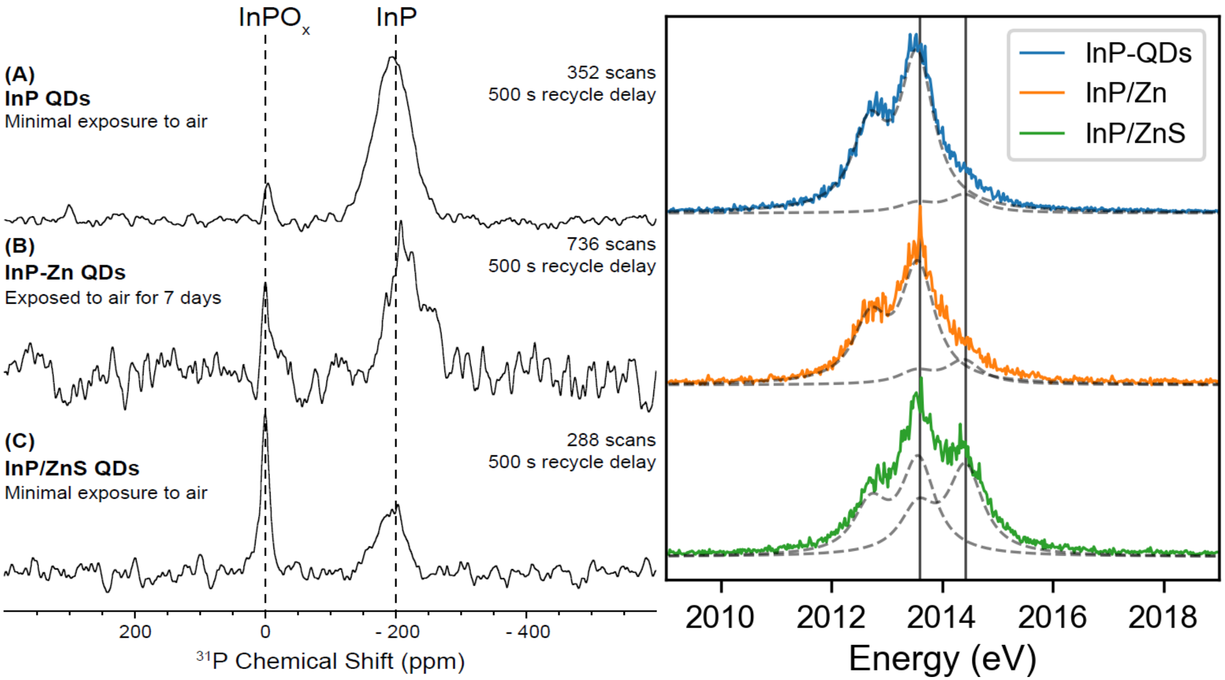

Figure 3.3. Full comparison of ^{31}P SSNMR (left) and P Kα spectra (right) collected on InP, InP/Zn, and InP/ZnS (all from **C**-InP QDs) to verify that quantitative measurements were comparable.

Table 3.4. Comparison of SSNMR and P Kα XES for Determination of Phosphorus Oxidation State in InP QDs

Sample	SSNMR (% red)	SSNMR (% ox)	P Kα XES (% red)	P Kα XES (% ox)
InP	93	7	89 ± 3	11 ± 3
InP/Zn	87	13	83 ± 4	17 ± 4
InP/ZnS	54	46	51 ± 5	49 ± 5

These measurements demonstrate that P Kα XES is a reliable tool for measuring phosphorus oxidation having significant advantages over ^{31}P SSNMR spectroscopy. Each XES measurement required <5 mg of material and speciation could be determined within the first 30 minutes, though the measurements were extended to improve the resulting spectra and monitor for possible radiation damage (Figure 3.4, Figure 3.5). The SSNMR measurements required ca. 10-20 mg of material to prepare the samples for measurements (although within the 1.3 mm rotor there is likely less than 1 mg of material). Regardless, the SSNMR spectra required multiple days of collection time to obtain spectra that can be reliably integrated. Based on this promising data, we proceeded by measuring the extent of phosphorus oxidation as a function of synthetic method using XES for rapid feedback, augmented by SSNMR and other methods when appropriate. Our goal is to obtain a uniquely detailed picture of the existence and origin of synthesis-specific adventitious phosphorus oxidation and its correlation with QD QY. A detailed understanding of phosphorus speciation and the degree of oxidation induced by different synthetic procedures is a critical first step to devising new synthetic routes to high performance InP QDs.

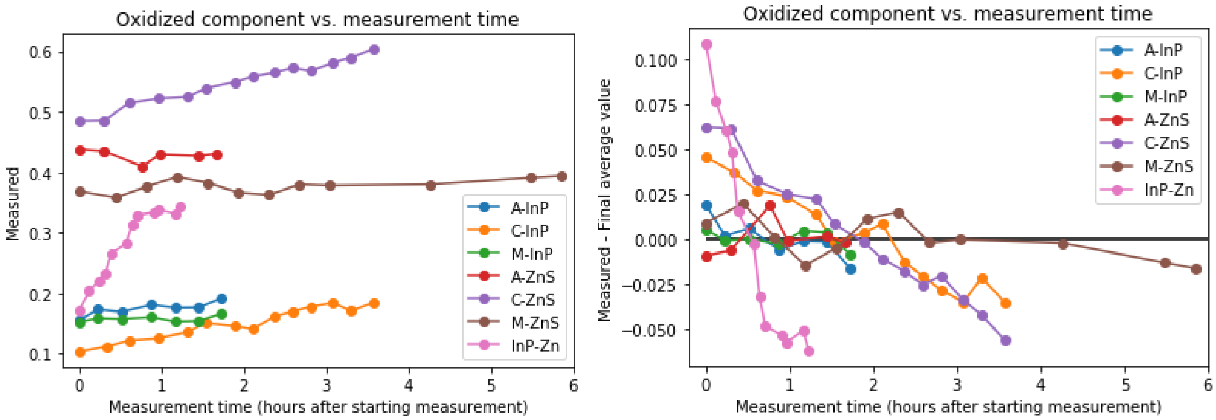

Figure 3.4. Calculated oxidized fraction versus measurement time determined by 2-component fitting, used to monitor for changes in the signal which may indicate radiation-induced damage to the sample. For samples C-InP, InP/Zn, and C/ZnS, we believe that a vacuum leak contributed to the large monotonic changes in the oxidized fraction.

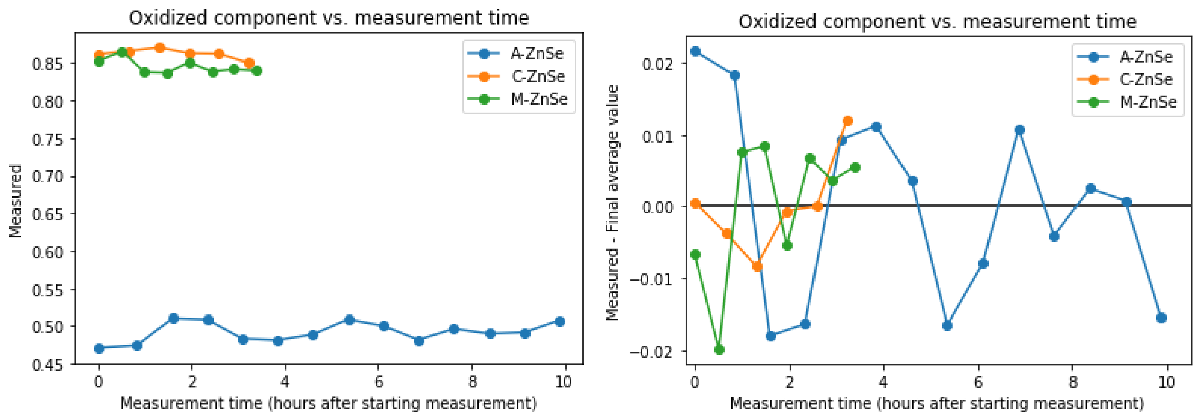

Figure 3.5. Calculated oxidized fraction for the ZnSe-shelled samples versus measurement time using three-component fitting and normalizing out the TOPO contribution.

3.3.1 *Surface Oxidation as a Function of Initial InP Synthesis*

Here, we evaluate the extent of oxidation that can occur in a core synthesis by studying InP quantum dots synthesized via three different routes. All reactions were performed under air-free conditions in a nitrogen-atmosphere glovebox or on a Schlenk line. All reagents and glassware were rigorously dried as described in the experimental section. A summary of particle characterization for this series of InP QDs including optical peak positions, composition, particle size, and powder diffraction patterns, can be found in Table 3.5 and Figure 3.6.

Table 3.5. Absorbance and emission peak positions, emission FWHM, PL QYs, particle sizes, and particle compositions are summarized for the series of InP, InP/ZnS, and InP/ZnSe samples.

Sample	Absorbance λ_{max} (nm)	Emission λ_{max} (nm)	Emission FWHM (nm/meV)[a]	PL QY (%)	Particle diameter (nm)	Molar ratios (In:P:Zn:E)
C-InP	530	579	-	<1	2.4 ± 0.4	2.3:1
M-InP	555	591	-	<1	2.2 ± 0.3	1.5:1
A-InP	573	618	-	3	2.9 ± 0.4	1:1:0.45
C/ZnS	522	578	66/213	7	2.9 ± 0.4[b]	3.7:1:4.8:3
M/ZnS	546	584	56/177	28	2.7 ± 0.3	2:1:3:1.5
A/ZnS	575	621	69/200	25	3.6 ± 0.3	2.2:1:8.7:3.2
C/ZnSe	560	600	61/206	10	8.2 ± 2.1	1:2:20:12
M/ZnSe	588	602	59/186	44	10.0 ± 1.4[c]	2:1:26:20
A/ZnSe	626	659	84/246	30	8.3 ± 1.3 11.7 ± 1.0[d]	1:1:32:27

[a] The full width at half maximum was measured in eV and is shown in both meV and nm in order to readily compare to literature reported FWHM values

[b] Sample set included larger particle aggregates on the order of 8-10 nm diameters and particle measurement reflects the InP/ZnS particles

[c] Tetrahedral particle “diameters” were measured from one vertex to the base

[d] The majority of particles were amorphous so the length and width were both measured

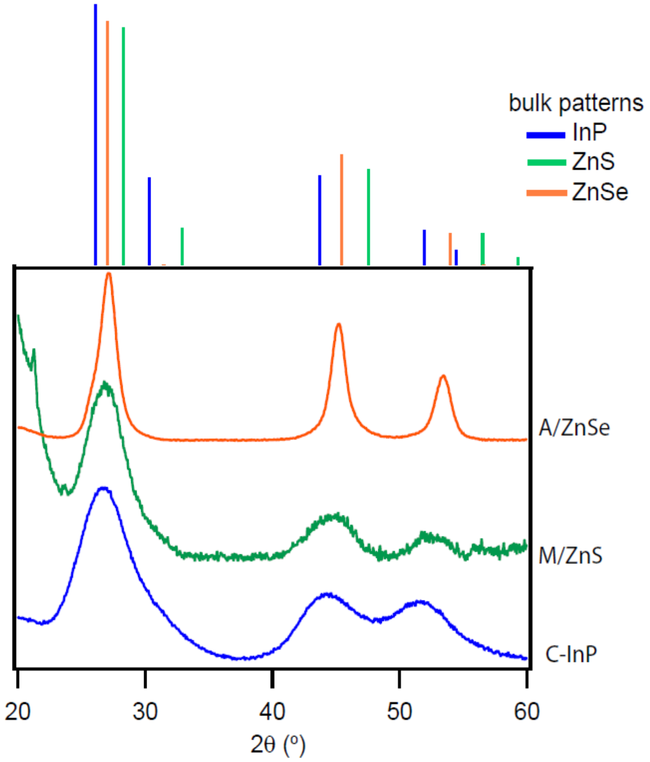

Figure 3.6. Representative powder X-ray diffraction patterns of purified InP and InP/ZnE QDs with corresponding bulk patterns

The first synthesis is the most common approach to produce crystalline InP QDs through the reaction between indium carboxylates, excess carboxylic acid, and tris(trimethylsilyl)phosphine, $P(SiMe_3)_3$, at elevated temperatures.[9,37,38] In future reference and plots, InP QDs prepared by this route (indium carboxylates + $P(SiMe_3)_3$) will be referred to as **C-InP**. Although this approach is well-established, water is generated as a by-product from carboxylic acid ketonization at elevated temperatures and thus, the InP QDs are detrimentally impacted through surface oxidation. This oxidation has previously been implicated in the inability to grow InP QDs to large diameters.[14,39] Thus far, water has been identified as the most likely primary source of oxygen atoms involved in phosphate formation.[35,40] Chaudret and co-workers characterized the amorphous surface oxide layer that is produced by the concurrent oxidation through a combination of XPS, IR, and SSNMR spectroscopy.[11]

C-InP was synthesized following a literature procedure in which $P(SiMe_3)_3$ was injected into a 300 ºC 1-octadecene (ODE) bath of indium myristate and excess myristic acid.[41] The resulting particles shown in Figure 3.7 have a lowest energy electronic transition (LEET) at 530 nm and weak emission features comprised of a peak at 579 nm and a broad red-shifted shoulder that corresponds to band edge and radiative surface defect emission, respectively. The normalized PL spectrum is shown in Figure 3.8 and corresponds to a PL QY <1%.

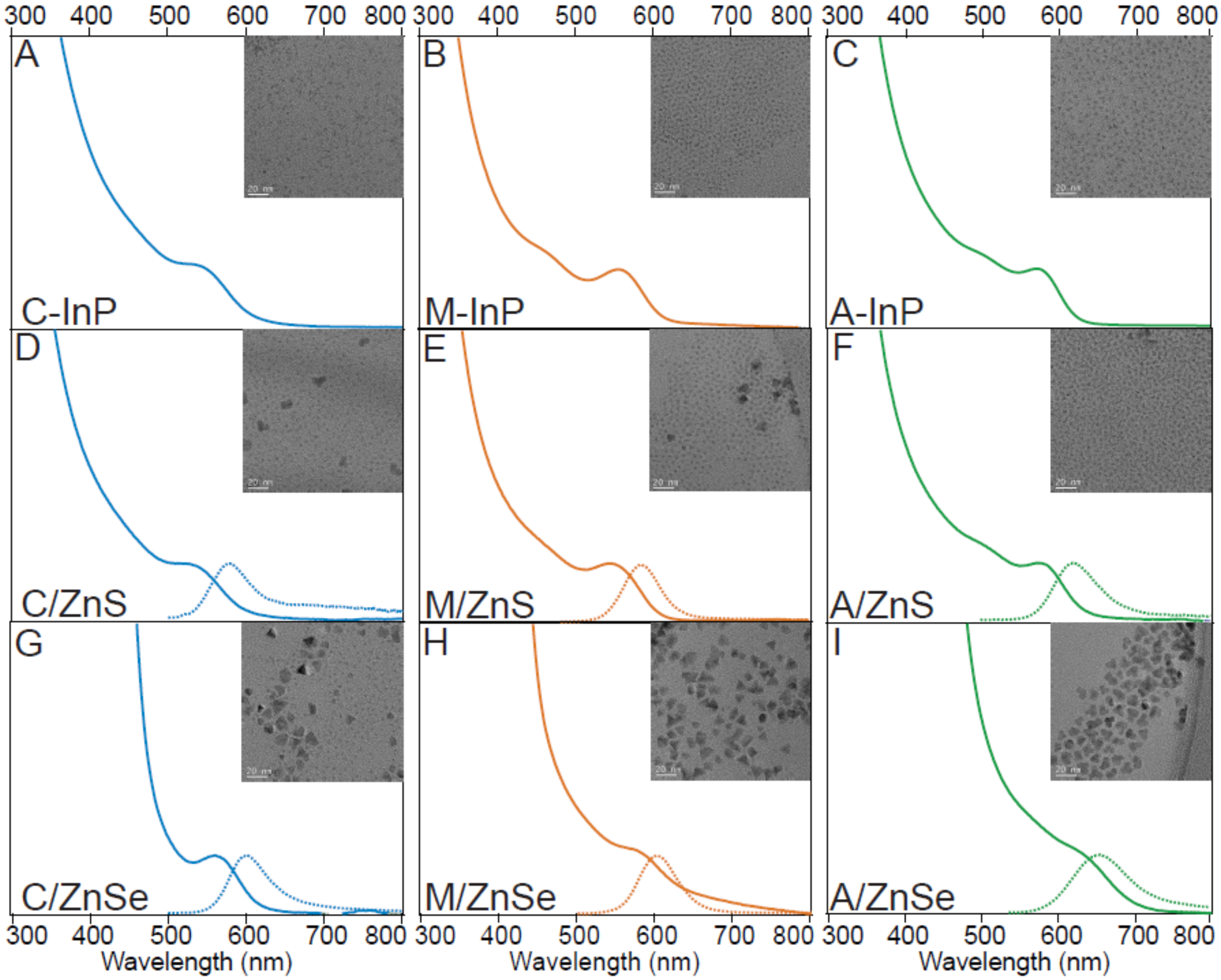

Figure 3.7. The final absorbance trace (solid) and photoluminescence (dashed) of (a) C-InP, (b) M-InP, (c) A-InP, (d) C/ZnS, (e) M/ZnS, (f) A/ZnS, (g) C/ZnSe, (h) M/ZnSe, (i) A/ZnSe with TEM image insets (20 nm scale bar) of purified material.

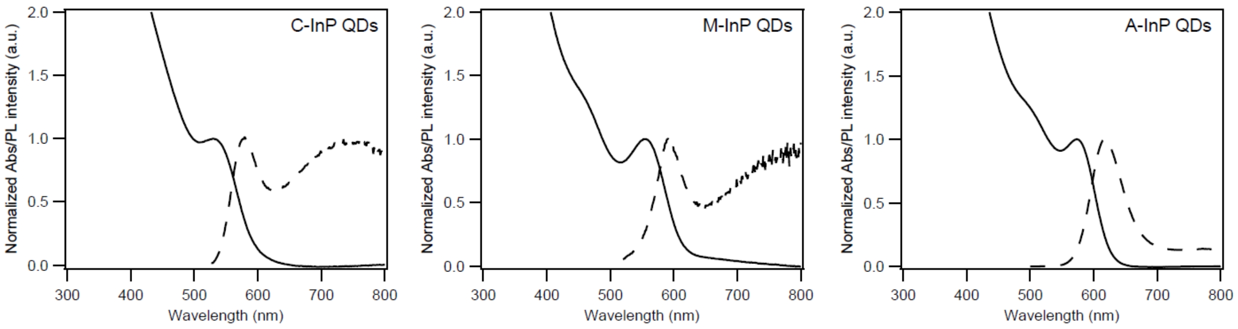

Figure 3.8. Normalized photoluminescence spectra of initial **C**, **M**, and **A**-InP QDs. PL QYs are <1% for the **C** and **M**-InP while the incorporation of zinc in the nucleation solution of **A**-InP QDs resulted in a 3% PL QY.

In the second synthesis, atomically-precise $In_{37}P_{20}(O_2CR)_{51}$ magic-sized clusters (MSCs) were used as single-source precursors.[42,43] Carboxylate-capped InP MSCs can be purified to remove any freely diffusing carboxylic acid, ensuring that the reaction solution is a homogeneous mixture of only the MSCs. We found this an appealing choice for this study since the removal of acidic protons would ideally prevent decarboxylative coupling and aqueous by-products. In future reference, the quantum dots derived from InP MSCs are referred to as **M**-InP.

The production of **M**-InP requires two steps, with the first step being the synthesis and isolation of $In_{37}P_{20}(O_2CR)_{51}$. This can be done by following the conditions to make **C**-InP QDs as described above but dropping the injection/growth temperature to 100 ºC and running the reaction in toluene.[43] The MSCs were purified through gel permeation chromatography (GPC) and analyzed by ^{1}H NMR spectroscopy to ensure the removal of excess acid (Figure 3.9). At this point, a portion of MSCs, which exist in the form of a waxy solid, can be dissolved in ODE and injected into a 300 ºC solution of ODE. Depending on the concentration of MSCs in the growth solution, particle size can be modified.[43] In this instance, a 60 mg injection of MSC produced particles with a LEET at 555 nm and emission features similar to **C**-InP with the band edge emission at 591 nm

(Figure 3.7b and Figure 3.8). The advantages to using this 2-step route over traditional indium/phosphorus monomer nucleation are two-fold in that the synthesis can be performed more reproducibly with a homogeneous precursor and the monodispersity of the resulting sample ensemble is improved. TEM images of **M**-InP QDs show this with more ordered packing due to the more uniform particle morphologies.

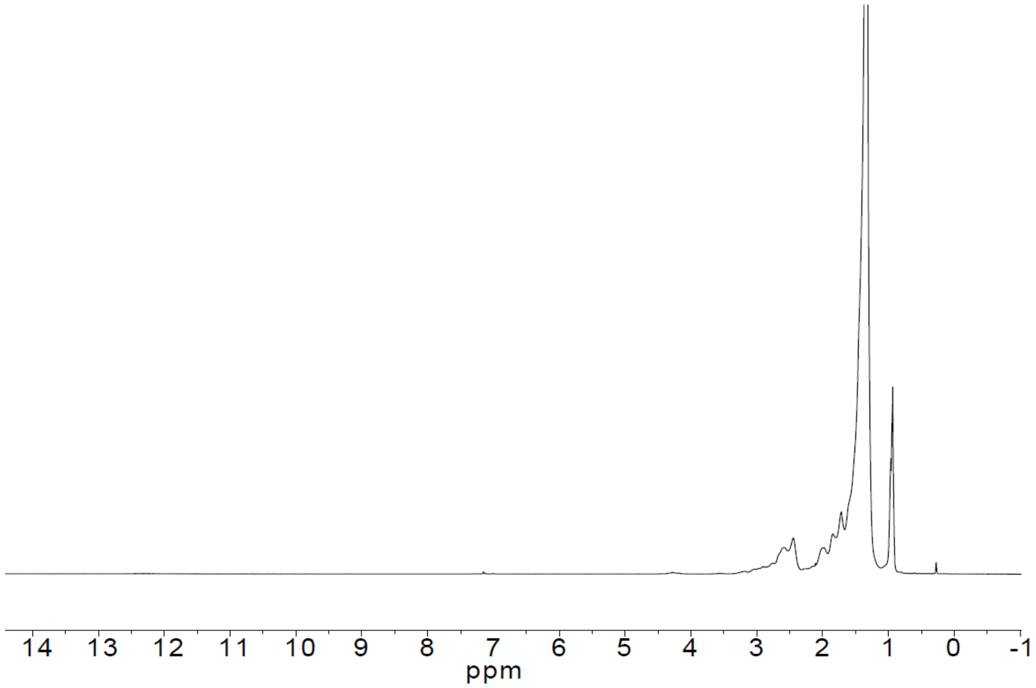

Figure 3.9. ^{1}H NMR spectrum of purified InP MSC stock taken in C_6D_6 (7.16 ppm) showing the absence of acidic proton remaining from excess acid used in synthesis.

In the final synthesis method, we examined InP QDs prepared from indium halides and aminophosphines in a primary amine solvent. Aminophosphines have been introduced as reliable phosphorus precursors for the synthesis of size-tunable InP QDs when paired with indium halides.[44] The reaction between metal halides and aminophosphines is driven by the dual role of aminophosphines as a phosphorus source and as a reducing agent.[19,45] More importantly for the present work, the aminophosphine synthesis does not involve any oxygen-containing reagents, eliminating the possibility of oxidation via reagent decomposition products. In future reference and plots, InP QDs synthesized with an aminophosphine P-source will be referred to as **A**-InP.

The aminophosphine-based InP QD synthesis diverges from indium carboxylate/silylphosphine chemistry in that the solvent, a primary amine, is coordinating and so acts as a solvent, ligand, and even plays a role in the precursor conversion reactions. Furthermore, Zn(II) was added to the precursor mixture prior to particle nucleation and has been observed to improve the resulting particle crystallinity and monodispersity. Further details can be found in the Experimental section but briefly, zinc chloride and indium chloride were heated to 180 ºC in oleylamine followed by injection of tris(diethylamino)phosphine. The final **A**-InP particles have a LEET at 573 nm and an emission peak at 618 nm (3% PL QY) shown in Figure 3.7c and Figure 3.8. Replacing carboxylates as surface ligands with chlorides and amines also impacts particle morphology by preferentially binding to the (111) face as seen by the tetrahedral shape of the resulting particles.[14]

Kα XES measurements were used to measure phosphorus speciation as described in the Experimental section. The P Kα emission spectra of **C**, **M**, and **A**-InP QDs are shown in Figure 3.10 with corresponding peak positions and speciation percentages summarized in Table 3.6. The lower energy component is described as 'reduced' and the higher energy component is described as 'oxidized'. We attribute the 11% oxidized component measured in **C**-InP to the previously characterized ketonization reaction that occurs during particle growth, which is supported by the two phosphorus resonances in the ^{31}P SSNMR spectrum (Figure 3.11). At elevated temperatures, the excess acid undergoes decarboxylative coupling in which a ketone, carbon dioxide, and water are products. Our initial expectation from the **M**-InP was to circumvent water formation through the removal of acid. As can be seen from the 16% oxidized component of **M**-InP, this process was difficult to avoid. A solution ^{13}C NMR spectrum of the **M**-InP QDs before purification shows an apparent peak in the expected region for a ketone carbon at 210 ppm (Figure 3.12); formation of ketone in the synthesis would be accompanied by the formation of water. There is a notable lack of an acidic proton in the ^{1}H NMR spectrum of the initial MSCs, suggesting no free carboxylic acid is present prior to synthesis. Furthermore, the P Kα emission spectrum of the stock MSCs shows that the starting material was not oxidized, which agrees with the single-crystal structure that is fully saturated with surface indium carboxylates (Figure 3.13).[42] However, we hypothesize that in the case of long-chain carboxylate ligands, carboxylic acid is difficult to remove due to hydrogen bonding interactions and entanglement of the aliphatic side-chains with the carboxylate ligand shell.

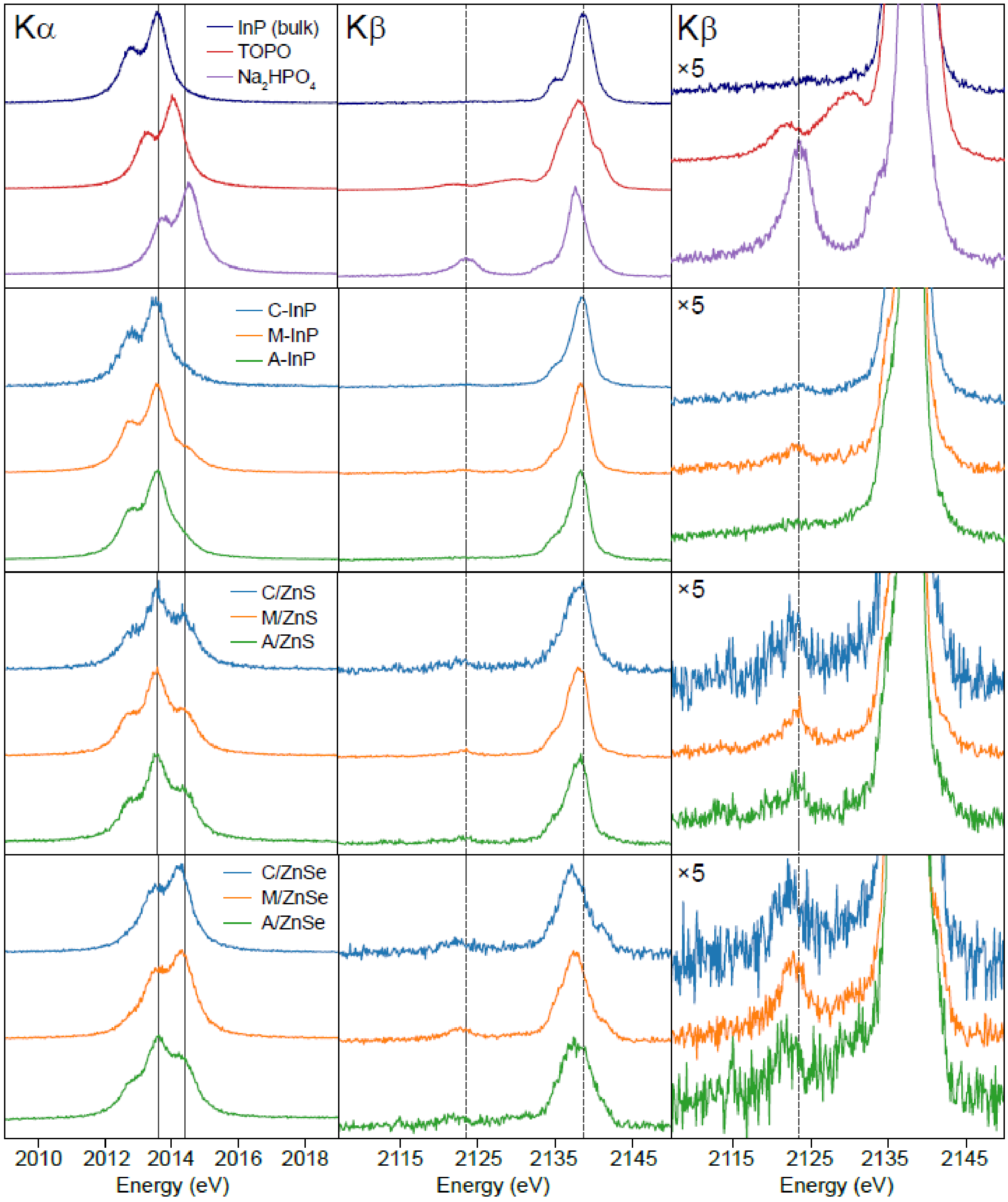

Figure 3.10. P Kα and Kβ XES spectra for the InP-QD samples. The spectra of the reference compounds are reproduced from Figure 3.1 for convenience of comparison. Solid vertical lines in the Kα spectra indicate the InP component (2013.59 eV) and the identified phosphate component (2014.41 eV). In the Kβ spectra, dashed lines indicate the Kβ’ peak of phosphate (2123.5 eV), and the $K\beta_{1,3}$ peak of bulk InP (2138.6 eV).

Table 3.6. Phosphorus Speciation as Determined by Linear Combination Fitting to Kα XES Spectra

Sample	**Main Result**		**Estimated uncertainties from different sources**						**Final Uncertainty estimate**
					Varying $K\alpha_{1,2}$ ratio (1.7-2.3)		**Varying Voigt widths (±2%)**		
	Red (%)	**Oxid (%)**	**Statistical**	**Variation over time**	**Red (%)**	**Oxid (%)**	**Red (%)**	**Oxid (%)**	
C-InP	89	11	± 1.4	--	87.8 - 90.4	9.6 - 12.2	89.2-90.7	9.3-10.8	± 2.8
M-InP	84	16	± 0.4	± 1.0	82.8 - 85.7	15.3 - 17.2	84.1-85.5	14.5-15.9	± 2.3
A-InP	83	17	± 0.6	± 2.2	80.9 - 84.5	15.5 - 19.1	82.2-84.7	15.3-17.8	± 3.7
C/ZnS	51	49	± 1.4	--	48.7 - 54.7	45.3 - 51.3	51.3-53.4	46.6-48.7	± 4.5
M/ZnS	62	38	± 0.6	± 2.3	59.6 - 65.0	35.0 - 40.4	61.9-63.9	36.1-38.1	± 4.3
A/ZnS	57	43	± 0.8	± 2.0	54.5 - 60.4	39.6 - 45.5	57.0-59.1	40.9-43.0	± 4.5
InP-Zn	17	83	± 1.8	--	80.8 - 84.7	15.3 - 19.2	82.4-84.3	15.7-17.6	± 3.9

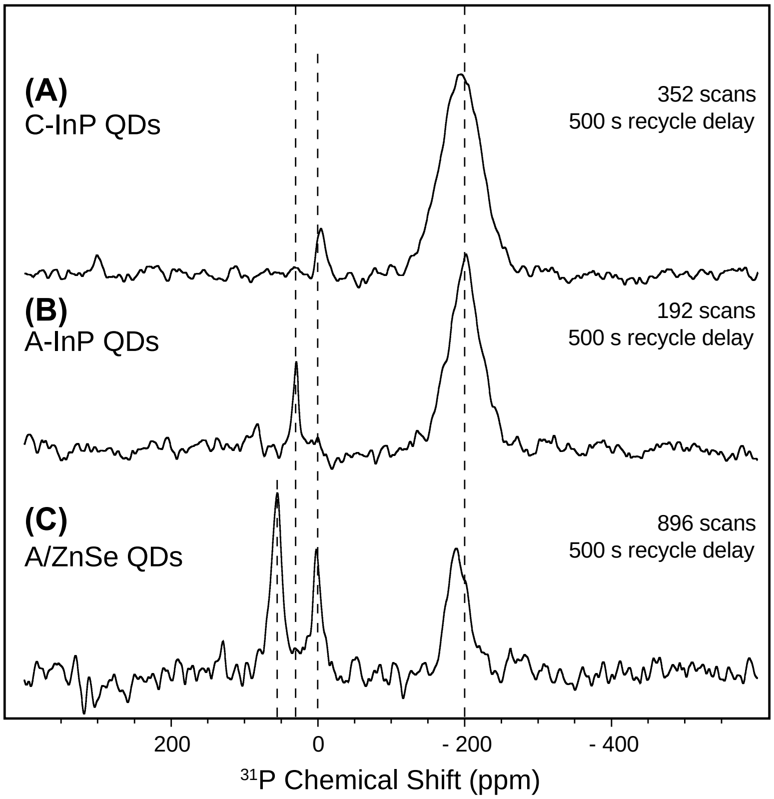

Figure 3.11. ^{31}P SSNMR spectra of (A) C-InP QDs (B) A-InP QDs and (C) A/ZnSe QDs. Dashed lines are to guide the eye to -200 ppm (phosphide resonance), 0 ppm (phosphate resonance), 30 ppm (phosphonium salt resonance), and 55 ppm (TOPO resonance).

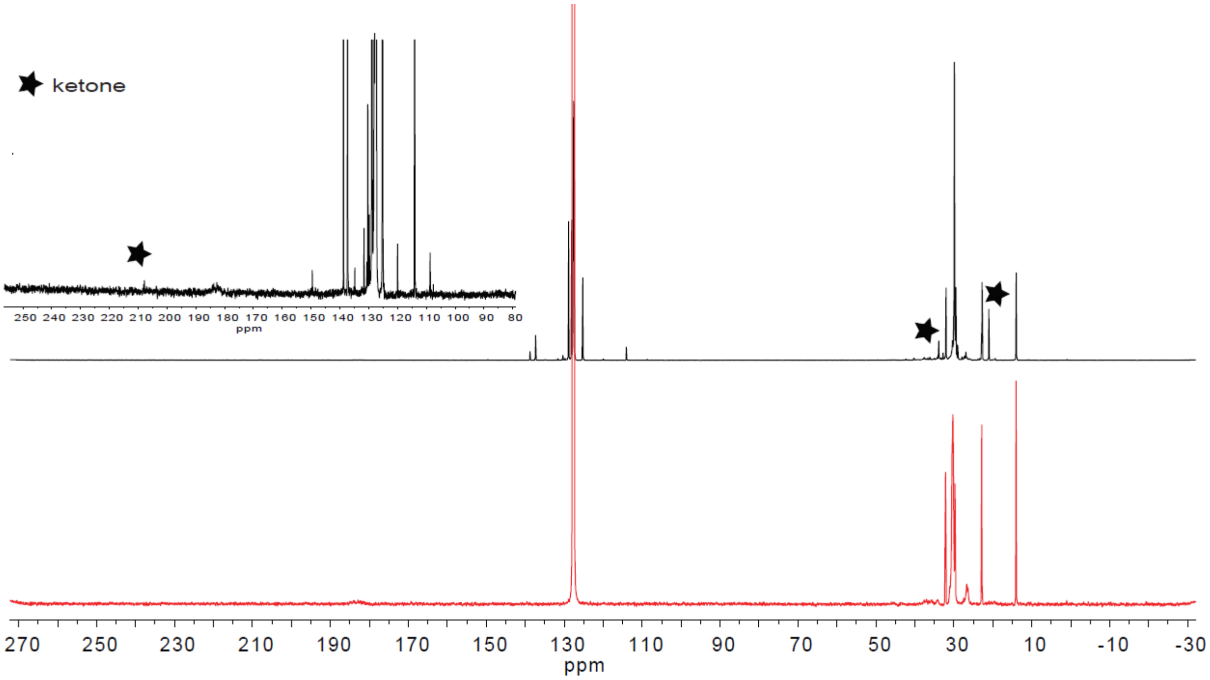

Figure 3.12. ^{13}C {^1H} NMR spectra taken at room temperature in C_6D_6 of the crude reaction of M-InP QDs (black). Unidentified peaks correspond to residual ODE and myristate ligands. For reference, the ^{13}C {^1H} NMR spectrum of purified myristate-capped InP magic-sized clusters is shown in red.

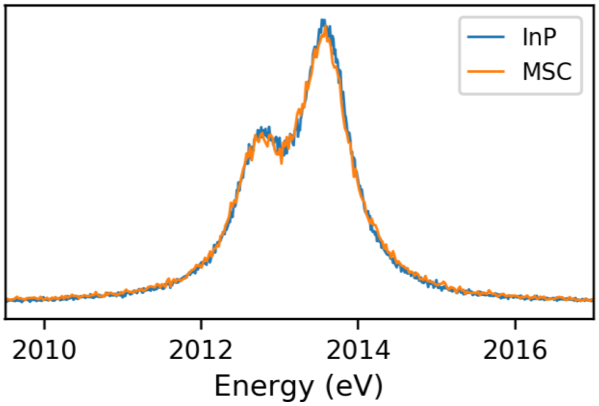

Figure 3.13. P Kα emission spectrum of InP magic-sized clusters overlaid with bulk InP to show that the oxidized population is negligible. In the first several scans, the measured P species were 100% P^{3-} but over time a 3% population of phosphate was introduced.

Unexpectedly, we measured a 17% oxidized component in the **A**-InP QDs, a synthesis lacking any oxygen-containing precursors. The Kα_1 energy position of the oxidized population was notably lower in energy than the component near 2014.41 eV identified above as phosphate, which led us to investigate further. P Kβ XES can be used for exactly this question of ligand identity. The strong Kβ' satellite feature at 2123.5 eV in the phosphate reference standard serves as a fingerprint of the presence of P–O bonds. P Kβ spectra of **C**, **M**, and **A**-InP QDs are shown in Figure 3.10. The **C**-InP and **M**-InP show clear peaks at the phosphate energy position, in qualitative agreement with their relative proportion of oxidized component (11% vs 16% respectively). In contrast, the absence of the Kβ' feature in the **A**-InP spectrum implies that the 17% oxidized component is not due to phosphate.

To investigate the identity of this component, we utilized XPS and solution ^{31}P NMR spectroscopy to aid in the detection of potential reaction by-products. Following multiple rounds of precipitation and GPC purification, we initially found that the solution ^{31}P NMR spectrum of the stock solution contained no detectable resonances. Over the period of several weeks of storage in a nitrogen atmosphere glovebox however, the solution ^{31}P NMR spectrum revealed P-containing impurities at 80 and 30 ppm (Figure 3.14). The peak at 80 ppm lies in the region of transaminated species produced during this reaction that likely exist in equilibrium with phosphonium salt by-products.[19,45] Phosphonium salts, $P(NHR)_4Cl$ in which R is an oleyl group, is the dominant reaction by-product, forming 3 equivalents for every InP unit formed, and has been previously identified in the ^{31}P NMR spectrum to have a peak at 29 ppm. Although alternative routes to remove P-containing impurities exist, of which ligand exchange with thiols has met with success, subjecting the InP particle surface to further modification was not an ideal pathway with the goal of probing the surface defects intrinsic to the synthesis. The direct excitation ^{31}P SSNMR spectrum identified that there was a mixed environment of core InP, 91%, centered at –200 ppm and phosphonium salt, 9%, at 30 ppm with a notable absence of signal at 0 ppm that would correspond to surface phosphate species (Figure 3.11). The P_{2p} XPS spectrum shown in Figure 3.15 further supports the identification of a mixed phosphide/phosphonium environment when compared to the peak position of a commercial phosphonium salt (aminotris(dimethylamino)phosphonium chloride). Lastly, we measured the P Kα XES spectrum of the commercial phosphonium salt, and observed a $K\alpha_1$ energy position at 2014.35 eV, which agrees well with the shift of $K\alpha_1$ position to lower energy for the **A**-InP sample. Taken together, this evidence supports the conclusion that the 17% oxidized component is a result of electrostatically interacting phosphonium impurities and the **A**-InP particle surface can be considered unsullied P^{3-}.

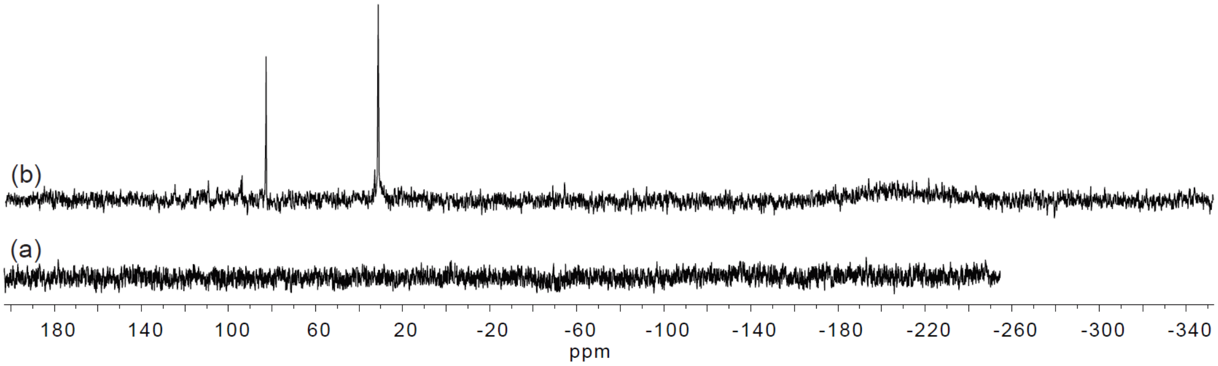

Figure 3.14. Solution ^{31}P NMR spectra of (a) A-InP QDs taken immediately following purification and (b) A-InP QD stock solution (toluene) stored in nitrogen atmosphere glovebox after 3 weeks. Molecular impurities are visible at 80 and 30 ppm and the broad resonance centered at –190 ppm corresponds to indium phosphide.

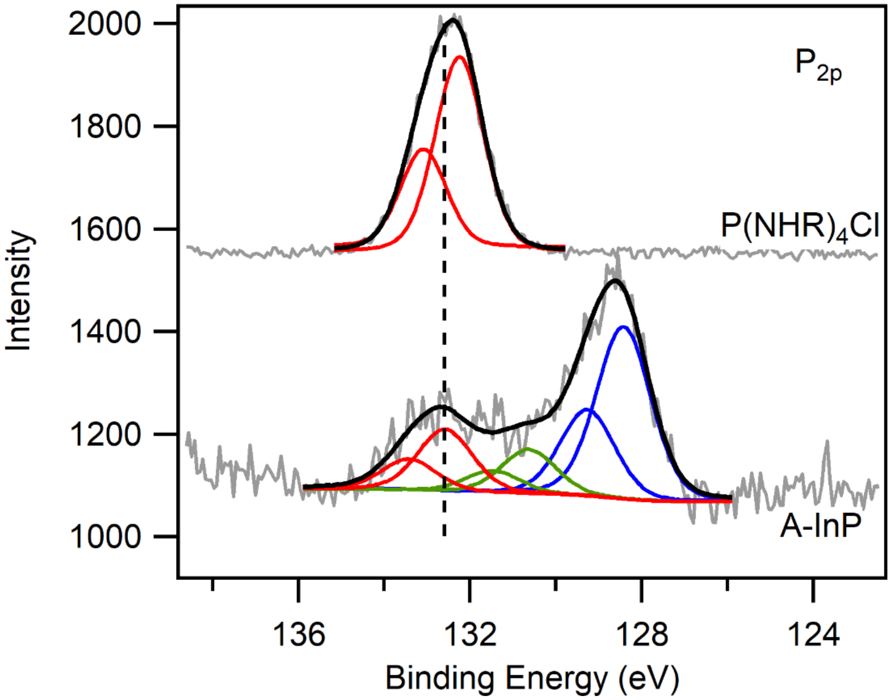

Figure 3.15. P_{2p} XPS spectra of commercial phosphonium salt (top) and **A**-InP QDs (bottom).

As demonstrated by the P Kα emission spectra of InP QDs formed in the presence of carboxylate groups (**C** and **M** samples), ketonization is difficult to prevent, even following attempts to remove excess acid in the case of MSC precursors. Alternatively, utilizing aminophosphines effectively reduces *in-situ* oxidation while also minimizing the cost and hazard of the phosphorus precursor. Progress has been made toward other oxide-free syntheses in which InP is formed by heating indium carboxylates and $P(SiMe_3)_3$ in a 1.8 bar H_2 atmosphere.[17] The authors conclude that H_2 molecules are activated at the QD surface and yield P–H bonds which protect the surface through the concurrent water-forming condensation reactions. At this point, oxidative-defect-free surfaces are accessible if running a synthesis under H_2 or utilizing aminophosphines with indium halides, while offering different options for surface chemistry or particle morphologies. The general consensus in the field of InP QD chemistry is that the presence of surface phosphorus-oxygen bonds will detrimentally impact subsequent shell growth. We extend the characterization of InP QD oxidation through the addition of ZnE (E=S, Se) shells to gauge the effect further chemical transformations may have on the optical properties and oxidized populations of the InP samples.

3.3.2 *Impact of Oxidative Surface Species on Optical Properties*

We chose to examine the resulting properties of the **C**/**M**/**A**-InP series shelled with either a thin ZnS shell or a thick ZnSe shell. With regard to the ZnS shell, we refer back to the work Chaudret and co-workers performed in characterizing the InP/ZnS interface.[12] ZnS was grown by the successive ion layer adsorption and reaction (SILAR) approach in which zinc carboxylate and sulfur powder were added separately at elevated temperatures in order to drive reaction with the InP surface and prevent nucleation of ZnS nanoparticles.[37] Through extensive optimization, thin ZnS shells (<2 nm) have been able to enhance the QYs of InP QDs up to 60-70%. The Chaudret group found that InP is even further oxidized during shell growth due to a series of side reactions. First, elemental sulfur has been observed to form hydrogen sulfide through activation by the solvent, ODE.[46] H_2S then reacts with zinc carboxylate to form carboxylic acids which promote ketonization and water production as seen in the initial InP core syntheses (**C**-InP). They found that the oxidized percentage of phosphorus in the core InP increased from 8% to 21% following shell growth. This approach to ZnS shell growth was selected to compare the impact of an established oxidation chemistry across the series of InP QDs.

The second comparison we focus on is the growth of a thick (>5 nm) ZnSe shell. In addition to minimizing the surface defects to improve the core-shell interface, selecting materials with similar lattice constants aids in reducing strain. ZnSe has a 3.4% lattice mismatch with InP, which is smaller than that of ZnS at 7.7%, and thus may improve InP optical properties. Recently, thicker

ZnSe shells have been reported in the literature to suppress the single-dot PL intermittency of InP QDs associated with nonradiative Auger processes, with QYs reaching 60%.[47,48] While the thick shell effectively cuts off carrier interaction with the environment, the compressive strain induced upon the core nanoparticle can often lead to further lattice strain-related defects.[49] Some of the detrimental effects of thick shells have been offset by alloying, particularly at the interface, or by stacking materials with a gradient lattice, as observed in chalcogenide-based materials.[50–52]

Following purification by GPC, solutions of **C**, **M**, and **A**-InP were dissolved in either ODE or squalane for shell growth. Rather than optimize conditions for maximum QY, we emphasized the comparison across initial InP syntheses by matching the concentration of the InP samples by standardizing the absorption at 310 nm across pre-shelled solutions in order to add the same amount of Zn and chalcogenide precursors. It should be noted that the particles are not precisely the same size made evident by TEM and the λ_{max}, in addition to particle polydispersity, which may contribute to differences among the observed shell thicknesses. A summary of particle characterization for this series of InP/ZnE QDs including optical peak positions, composition, particle size, and powder diffraction patterns, can be found in Figure 3.6 and Table 3.5.

ZnS shells were grown following a literature procedure in which zinc myristate and sulfur powder were added individually over 10 minute intervals to InP QDs at elevated temperatures. This layer by layer approach was performed a second time for an intended 2 monolayer ZnS shell. The resulting InP/ZnS particles exhibit a minor blue-shift in their features, which we attribute to a combination of zinc passivation and etching by H_2S produced in the synthesis (Figure 3.7). The measured PL QYs and emission linewidths for **C**/ZnS, **M**/ZnS, and **A**/ZnS were 7% (66 nm), 28% (56 nm), and 25% (69 nm), respectively. Comparatively, the emission linewidths of highly optimized core-shell InP syntheses are 40-60 nm.[9]

The P Kα emission spectra of the InP/ZnS samples demonstrate that each InP core was significantly oxidized (Figure 3.10). Peak positions, given in Table 3.6, are in line with our identified phosphate and phosphide components and show that the phosphate population for all samples increased to a range of 38-49%. The P Kβ spectrum supports the identification of the oxidized component as phosphate, with strong Kβ' peaks at 2123.5 eV (Figure 3.10). From previous reports of a shell growth-coupled oxidation event, we expected a substantial increase in phosphorus oxidation. Surprisingly, the extent of phosphorus oxidation is apparently not dependent on the initial InP surface environment. Along those lines, it is difficult to correlate the amount of oxidized defects with the optical properties since in each case a majority of the surface phosphorus were converted to phosphates. The important conclusion from this series of samples is that even when starting with an ideally oxidative defect-free surface, adventitious side reactions during shell growth will still significantly impact the InP surface and thus the core-shell interface.

With regard to InP/ZnSe, chemists have postulated that incomplete blinking suppression and low quantum yields (40-60%) originate from point defects at the core-shell interface, which was a motivating aspect of studying these samples. Similarly to the ZnS shell growth, InP QD solutions were matched in concentration across **C**, **M**, and **A** in order to reliably compare across the three. Again utilizing a SILAR approach, zinc myristate and trioctylphosphine-selenide (TOP-Se) were added to InP QDs at elevated temperatures at varying time intervals (see Experimental section for specific details). Two distinct features arise in the absorbance spectra, one of which is a significant increase in higher energy absorbance due to the ZnSe shell. Secondly, the LEET experiences a red-shift due to the near overlap of the InP and ZnSe conduction band edges (Figure 3.7). The emission linewidths range from 59 to 84 nm with the **M**-InP giving the most narrow linewidth (59 nm) likely due to the improved monodispersity of the starting InP cores.

Compared to the InP/ZnS samples, the PL QY of these un-optimized syntheses were slightly greater with a maximum of 44% from the **M**/ZnSe and 10% and 30% for **C**/ZnSe and **A**/ZnSe, respectively. At least in the case of the **C**/ZnSe, there was a mixture of thick-shelled particles and what could be partially shelled or unshelled InP QDs that limit the measured quantum yield (Figure 3.7). For a majority of the **C** and **M**/ZnSe, the morphology of the shelled particles was tetrahedral while the **A**/ZnSe appeared to shell less uniformly and typically looked bulbous, suggesting shell nucleation occurred separately at each vertex of the InP tetrahedron as opposed to conformal shell deposition on the more spherical cores observed in **C** and **M**. Shell uniformity will also play a role in optimizing emissive properties due to the detrimental impact of structural defects. Furthermore, because of the substantial shell thickness, XPS analysis of the InP/ZnSe only revealed the phosphate peak, most likely because photoelectrons generated in the core phosphide have a lower probability of escaping (Figure 3.16). In this context, XPS becomes an imprecise and unreliable technique.

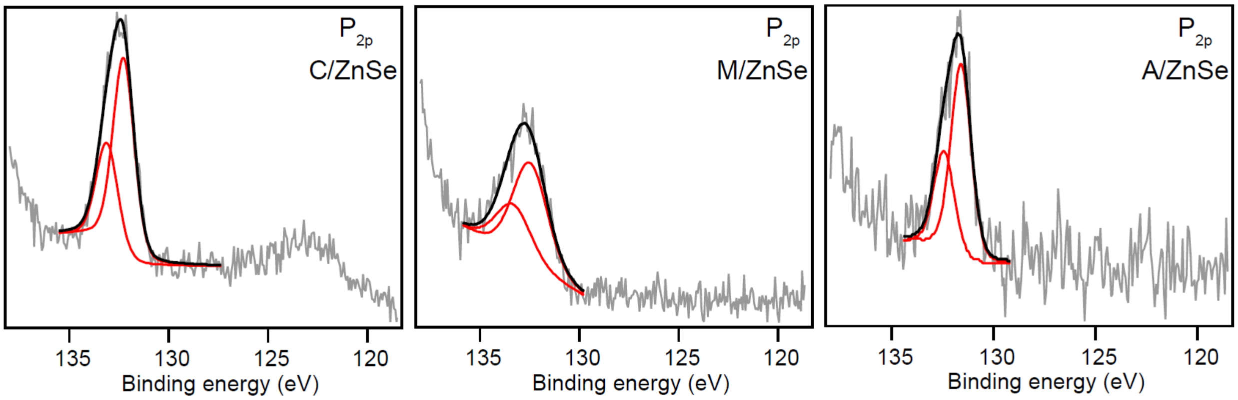

Figure 3.16. P_{2p} XPS spectrum of thick-ZnSe shelled InP QDs with a single population signal corresponding to phosphate. Any signal from core InP (128 eV) is negligible.

The P Kα emission spectra of the InP/ZnSe, shown in Figure 3.10, were distinctive in that the peak positions from two-component fitting did not overlap with our identified phosphide and phosphate components. The oxidized Kα_1 were shifted lower in energy and the reduced Kα_1 were shifted to higher energy (Table 3.7). These shifts, combined with the higher reduced-χ squared statistic of the **A**/ZnSe and **M**/ZnSe fits, suggest that the two-component fitting procedure does not sufficiently explain the observed spectra. Furthermore, we observed several differences in the Kβ emission spectra from typical InP such as the shift of the K$\beta_{1,3}$ peak to lower energies and a pronounced shoulder at 2140.5 eV (Figure 3.10).

Table 3.7. Attempted two-component fitting for the ZnSe-shelled samples

Sample	Reduced (%)	Oxidized (%)	Reduced Kα1 energy (eV)	Oxidized Kα1 energy (eV)	Reduced-χ2
C/ZnSe	15.4	84.7	2013.67	2014.27	1.12
M/ZnSe	19.6	80.4	2013.71	2014.35	1.70
A/ZnSe	47.8	52.2	2013.64	2014.37	1.80

To reconcile these clear changes in the Kα and Kβ spectra for the ZnSe-shelled samples, we considered the possibility of a third significant phosphorus species present in the sample. Fortunately, the main decomposition product of TOP-Se has been previously identified as trioctylphosphine oxide (TOPO) through precursor evolution studies of cadmium chalcogenide nanocrystals.[53,54] The Kβ emission spectrum of TOPO (shown in Figure 3.10) qualitatively matched the distinctive features observed in the InP/ZnSe samples. Although sample purification focused on the removal of excess ligands and by-products, complete removal is often complicated because of entanglement of long chain hydrocarbons, and in this case by weak binding of the TOPO to the particle surface. Thus, in order to evaluate the reduced and oxidized populations excluding the TOPO component, the Kα spectra were fit with three P K$\alpha_{1,2}$ doublets as described in the Experimental section. This procedure results in improved fits for the **A**/ZnSe and **M**/ZnSe samples (Figure 3.17) and improved Kα_1 energy positions for all three samples (Table 3.8). Our analysis was further supported by the ^{31}P SSNMR spectrum of the **A**/ZnSe sample in which three populations of phosphorus are measured; phosphide at –200 ppm, phosphate at 0 ppm, and TOPO at 55 ppm, of which the integrated areas agree qualitatively with the three-component fitting results (Table 3.8). The presence of a significant phosphate species in each of these samples also agrees qualitatively with the Kβ spectra, each of which has a significant phosphate Kβ’ peak near 2123.5 eV, much stronger in proportion than the spectral features exhibited in the TOPO spectrum.

C/ZnSe

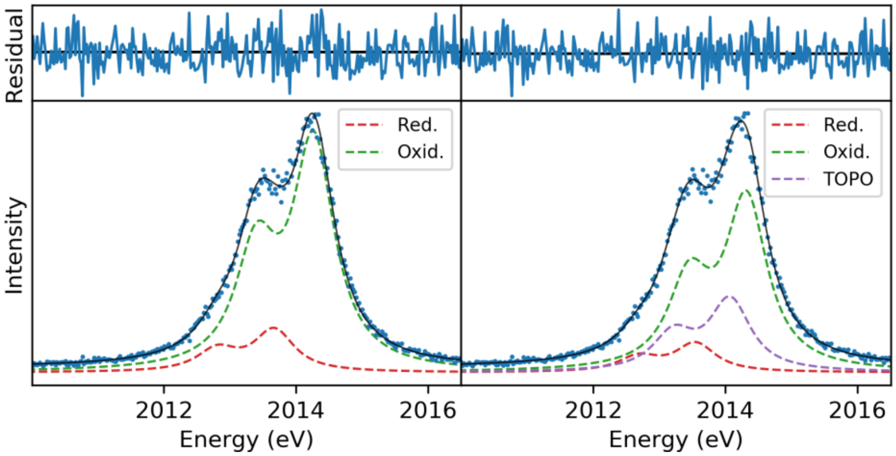

M/ZnSe

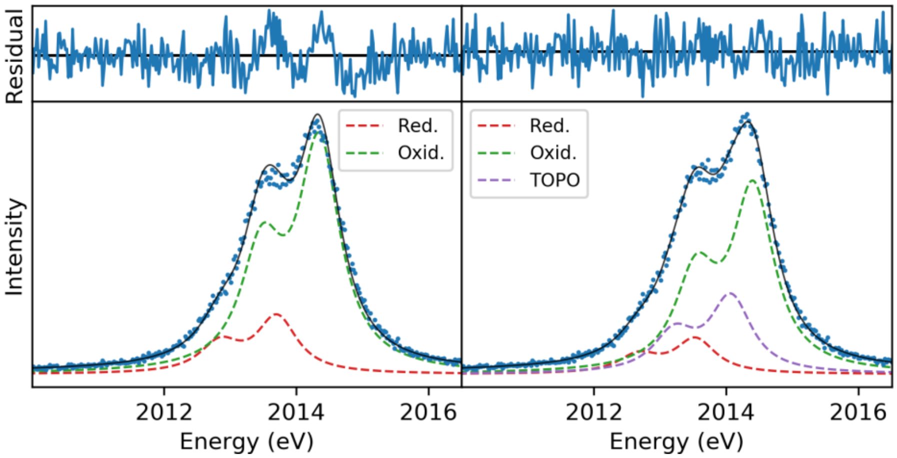

A/ZnSe

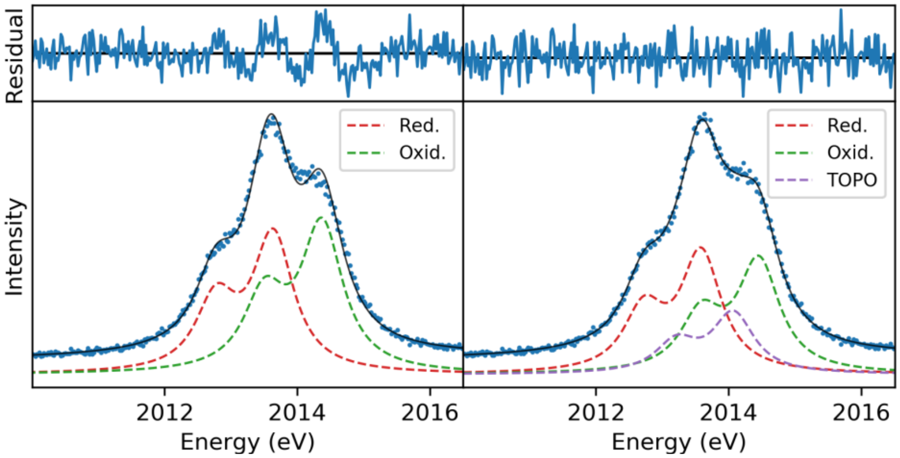

Figure 3.17. Comparison of 2-component and 3-component fitting for the InP/ZnSe samples

Table 3.8. Three-component fitting for the InP/ZnSe samples, with the third component fixed based on the measured TOPO $K\alpha_1$ energy position. Note that each value is rounded independently, so that the total may not add up to exactly 100%.

				Normalized without TOPO					
	Reduced (%)	Oxidized (%)	TOPO (%)	Reduced (%)	Oxidized (%)	Reduced Kα1 energy (eV)	Oxidized Kα1 energy (eV)	TOPO $K\alpha_1$ energy (eV)	Reduced-χ2
C/ZnSe	10	63	26	14	86	2013.55	2014.32	2014.07*	1.02
M/ZnSe	12	63	26	16	84	2013.53	2014.41	2014.07*	1.24
A/ZnSe	41	39	21	51	49	2013.58	2014.45	2014.07*	1.06

* Energy position fixed to the measured reference TOPO sample.

X-ray emission spectra of InP/ZnSe samples show very high oxidized components. In the case of the **A**/ZnSe, roughly 51% of the phosphorus remain as phosphide while a mere ~15% of the phosphide component in the **C**/ZnSe or **M**/ZnSe was retained. We estimated that the core InP particles would have roughly 55-70% of the total phosphorus exposed to the surface, thus while the pathway of oxidation during ZnSe shell growth is unknown, it is reasonable that nearly all surface sites are oxidized. Additionally, we would not expect oxidative defects to penetrate beyond the surface of the InP core so we suggest that anion diffusion occurs during shell growth (in the case of thick shells) that allows core phosphides to migrate to the surface of the shell. Evidence supporting this proposed anion diffusion mechanism was presented by Rosenthal *et al.* in which the energy dispersive X-ray chemical maps of InP/ZnSe particles demonstrate alloying of In/P atoms into the Zn/Se shell.[48] They hypothesized that alloying helps mitigate the increasing strain induced by the growth of a thick shell.

Our goal to examine the correlation between surface oxidation and luminescence properties in the InP/ZnSe samples was similarly obstructed by excessive oxidation that prevented a careful analysis of these key factors. As with the InP/ZnS particles, the core-shell interface is thoroughly oxidized regardless of the defect-free surface of the starting materials (i.e. **A**-InP). These results emphasize the importance of critically examining the chemistry occurring after the InP core growth phase, especially when rigorous care is taken to improve the quality of the core particles. There has been a growing awareness to address the issue of introducing oxidative defects during shell growth. For example, Jeong *et al.* targeted the growth of a ZnS shell in the absence of acid-containing precursors and reported a phosphate-free interface, but the PL QYs of these samples still plateaued at 60%.[14] If indeed the particles experienced no oxidation through core/shell growth, which was assessed with XPS, non-radiative recombination defect sites likely still formed as a combined result of compressive strain because of the growth of a >5 nm shell and the lattice mismatch between InP and ZnS.

3.4 Conclusions

Using a recently developed benchtop X-ray emission spectrometer, we have demonstrated the viability of phosphorus Kα XES measurements as a quantitative analytical tool to characterize the extent of oxidation in InP quantum dots through a comparative analysis with ^{31}P SSNMR spectroscopy. Complemented by measurements of the valence-to-core P Kβ emission using the same spectrometer, we were able to identify the presence of phosphate species and phosphine/phosphonium salt by-products, which was also confirmed by ^{31}P SSNMR. XES measurements gave us the capability to rapidly measure a high volume of samples with excellent resolution from only a few milligrams of deposited material. This demonstration strongly suggests a future in which benchtop XES serves a role in the routine analysis of phosphorus compounds and materials. We examined the impact of phosphorus oxidation on InP optical properties by measuring surface phosphorus oxidation as a function of synthetic method and shelling strategy. While there are routes to achieving a phosphate-free surface, these result in the specific ligation environment and particle morphology associated with indium halides and aminophosphine precursors. To expand upon the available options, it may serve the field to develop chemical methods to remove phosphate defects from InP QD surfaces. Side reactions occurring during shell growth further oxidize the interface to the extent that the initial condition of the core surface is inconsequential. Current industry patents cite the usage of the same precursors examined in this study, implicating the presence of oxidized surfaces and rationalizing the lower than expected PL QYs.[6] This strongly motivates a push towards designing shelling syntheses involving innocent precursors in an effort to minimize interfacial defect sites and optimizing conditions to prevent significant diffusion of phosphorus from the QD core.

3.5 Experimental

3.5.1 *X-ray Emission Spectroscopy*

P Kα and Kβ XES measurements were performed on a recently developed laboratory spectrometer, reported in detail in Holden *et al*.[21] The spectrometer uses a low-powered, unfocused X-ray tube (Varex VF50, 50W) to illuminate the sample, whose emitted X-rays are analyzed by a

10 cm radius of curvature cylindrical crystal analyzer and detected using a new home-made CMOS direct-exposure color X-ray camera.[21,55] The spectrometer makes use of the dispersive refocusing Rowland (DRR) geometry, in which the sample is placed within the Rowland circle and illuminated with an unfocused beam of incident radiation while a position-sensitive detector is placed tangential to the circle at the location of the refocused fluorescence. This method of illumination allows efficient collection of signal from the sample, and the entire energy region of interest is measured simultaneously by the CMOS camera functioning as a position-sensitive detector with sufficient single-photon energy resolution to reject background scatter and chamber-wall fluorescence. The wavelength dispersing component is a Si(111) cylindrically-bent Johann analyzer having a 10 cm radius of curvature (XRSTech). The Si(111) analyzer provides Bragg angles of 79° for P Kα (~2014eV) and 67.6° for P Kβ (~2138eV). To prevent air contamination during XES measurements, the sample and crystal are inside a small vacuum chamber which was pumped to <100 mTorr pressure during the measurements. For improved resolution at P Kα, the crystal analyzer was masked using aluminum foil to a 10×2 mm^2 region (along Rowland plane × out of Rowland plane). For the weaker P Kβ signal the crystal was unmasked in order to improve count rates at the expense of increased Johann error. The Johann error causes weak tails on the high-energy side of the spectrum. These distortions do not significantly affect the analysis of the P Kβ spectra used here. The energy scale of P Kα and Kβ measurements is calculated based on the instrumental geometry with Na_2HPO_4 as a reference standard having $K\alpha_1$ and $K\beta_{1,3}$ energy positions at 2014.55 eV and 2137.80 eV, respectively.[24]

The InP QD samples were prepared for XES measurements by drop-casting onto silicon wafers with a spot size ~3-4 mm in diameter with <5 mg of material. The drop-cast samples were stored in an inert nitrogen atmosphere and were briefly exposed to air during loading into the instrument. The wafers were mounted in the instrument and the drop-cast spot exposed directly to the incident beam. With the current instrumental configuration, switching between Kα and Kβ measurements requires manually repositioning the crystal analyzer and re-tuning, thus the measurements were done in batches to separately measure Kα and Kβ. Fresh InP QD samples were drop-cast for each measurement.

The P Kα emission spectra were analyzed using linear-combination fitting with the non-linear least-squares fitting Python package LMFIT.[56] With a few exceptions discussed below, spectra were fit with two oxidation state components, each consisting of two Voigt profiles representing the spin-split $K\alpha_1/K\alpha_2$ peaks. The widths and height ratios of these peak shapes were constrained to the values obtained from fitting the bulk InP and Na_2HPO_4 reference compounds, and the energy position of the two peak shapes were allowed to vary. The fits were weighted assuming Poisson statistics. The speciation was calculated from the relative intensity of the fit components.

The primary source of systematic uncertainty in this approach is due to limited prior knowledge of the number of distinct oxidation states in the sample. For the InP QDs, our primary expectation is a superposition of a low-energy $K\alpha_{1,2}$ spin-orbit split doublet representing the reduced phosphorus in the InP cores and a higher-energy $K\alpha_{1,2}$ doublet due to surface oxidized phosphorus species. If an appreciable amount of a third phosphorus species exists in an oxidation state between these two extremes, the energy positions and results of the phosphide-vs-phosphate speciation based on the erroneous two component fit will be skewed. As discussed in the Results, this effect was observed for samples where TOP-Se was used as a precursor, producing TOPO as a by-product. To analyze the spectra for those samples, linear combination fitting was performed with three components, where the energy positions of the reduced and oxidized components were allowed to vary, but the TOPO component was fixed to be at 2014.07 eV, as determined by measurement of a pure reference TOPO sample.

Another source of systematic uncertainty is variations in the detailed shape of the $K\alpha_{1,2}$ doublet for the components of the fitting procedure. Though these variations have not been reported in detail for phosphorus, variations in the $K\alpha_{1,2}$ intensity ratio in the range of 1.7-2.3 have been reported for a variety of sulfur compounds.[25] In addition, variations in the Voigt widths of the line shapes on the order of 2% are observed for the reference compounds measured here. The effect of these variations on the systematic uncertainty were estimated by performing the fitting procedure over a range of intensity ratios and widths, and the results are given in Table 3.9 and Table 3.10.

Table 3.9. Estimated uncertainties in the speciation calculation from different sources.

	Main Result		**Estimated uncertainties from different sources**						**Final Uncertainty estimate**
					Varying $K\alpha_{1,2}$ ratio (1.7-2.3)		**Varying Voigt widths (±2%)**		
Sample	**Red (%)**	**Oxid (%)**	**Statistical**	**Variation over time**	**Red (%)**	**Oxid (%)**	**Red (%)**	**Oxid (%)**	
C-InP	89	11	± 1.4	--	87.8 - 90.4	9.6 - 12.2	89.2-90.7	9.3-10.8	± 2.8
M-InP	84	16	± 0.4	± 1.0	82.8 - 85.7	15.3 - 17.2	84.1-85.5	14.5-15.9	± 2.3
A-InP	83	17	± 0.6	± 2.2	80.9 - 84.5	15.5 - 19.1	82.2-84.7	15.3-17.8	± 3.7
C/ZnS	51	49	± 1.4	--	48.7 - 54.7	45.3 - 51.3	51.3-53.4	46.6-48.7	± 4.5
M/ZnS	62	38	± 0.6	± 2.3	59.6 - 65.0	35.0 - 40.4	61.9-63.9	36.1-38.1	± 4.3
A/ZnS	57	43	± 0.8	± 2.0	54.5 - 60.4	39.6 - 45.5	57.0-59.1	40.9-43.0	± 4.5
InP-Zn	17	83	± 1.8	--	80.8 - 84.7	15.3 - 19.2	82.4-84.3	15.7-17.6	± 3.9

* **Statistical uncertainty:** Estimate based on propagation of the uncertainty of the amplitudes of the components in the fits. The uncertainty in the amplitude is estimated as 2× the standard error as estimated by the covariance matrix from the non-linear least squares fit output.

Variation over time: Uncertainty from variations in the signal during the measurement, possibly by radiation-induced damage to the sample. Numbers in the table are estimated as 2× the standard deviation of the calculated speciations vs. time shown in Figure S2.

(--) For sample C-InP, C/ZnS, and InP/Zn the large monotonic trend is believed to be accelerated radiation damage due to a vacuum leak. For those samples, only the first scan was used in the final calculation.

Varying $K\alpha_{1,2}$ ratio: Though the $K\alpha_{1,2}$ spectral shape is nearly unchanged for different oxidation states, there are some minor variations. Though these variations have not been reported in detail in the literature for phosphorus, variations of the $K\alpha_{1,2}$ intensity ratio in the approximate range of 1.7-2.3 were observed by Mori *et al.* in a study of Kα peakshapes for different sulfur compounds. The ranges are reported for a series of fits with each oxidation state component independently fixed to different values throughout the range 1.7-2.3.

Varying Voigt widths: Variation in the Voigt widths on the order of ± 2% are observed for the reference compounds measured here. The ranges are reported for a series of fits with each oxidation state component independently fixed to different values varied ± 2% relative to the peakshapes used in the main result.

Final estimate: The final estimate was obtained by adding in quadrature half the widths of the ranges from varying peakshapes along with the variation over time and then adding the result directly to the statistical uncertainty.

Table 3.10. Estimated uncertainties in the speciation calculation from different sources.

	Main Result		**Estimated uncertainties from different sources**						**Final uncertainty estimate**
			Statistical	**Variation over time**	**Varying $K\alpha_{1,2}$ ratio (1.7-2.3)**		**Varying Voigt widths (±2%)**		
Sample	**Red (%)**	**Oxid (%)**			**Red (%)**	**Oxid (%)**	**Red (%)**	**Oxid (%)**	
C/ZnSe	14	86	±1.9	±1.4	5 - 18	82 - 95	14 - 15	85 - 86	± 8.7
M/ZnSe	16	84	±1.4	±2.0	13 - 19	81 - 87	16 - 17	83 - 84	± 5.3
A/ZnSe	51	49	±1.1	±2.7	48 - 54	46 - 52	51 - 53	47 - 49	± 5.2

* After the reduced and oxidized fractions were calculated by normalizing out the contribution from the third component**,** uncertainties were estimated by the same procedures described in Table 3.9. The third component of the fit representing TOPO was fixed to the shape measured for the reference compound.

During the P Kα measurements, changes in speciation due to possible radiation damage were checked by performing the speciation calculations on subsets of the accumulated data. The results are shown in Figures S2 and S4. The majority of the samples changed speciation by less than ± 2% during the measurements and vary non-monotonically. For the three samples which show large monotonic changes, **C**-InP, **C**/ZnS, and InP/Zn, it is believed that a vacuum leak may have contributed. For those samples, only the first scan was kept for the final results. The vacuum leak was addressed before the remaining samples were measured.

To obtain a final estimate of the uncertainty from the XES fitting results, the uncertainty from signal variation over time was combined with the uncertainties estimated by varying the $K\alpha_{1,2}$ intensity ratio and Voigt widths and added to the statistical uncertainty. The full details are given in Table 3.9 and Table 3.10, and the final uncertainty estimates are given in Table 3.6.

3.5.2 *^{31}P MAS Solid State NMR Spectroscopy*

All quantum dot samples were prepared for SSNMR analysis from concentrated colloidal solutions (ca. 50 mg of dried quantum dots in 1 mL anhydrous toluene) by impregnating 150-450 µL of the colloidal solutions in 8-12 mg of boron nitride, in 50 µL aliquots. The mixture was allowed to dry on a watch glass for an hour before packing into a 1.3 mm rotor. In order to confirm that there is a minimal increase in oxidation induced by this procedure, ^{31}P SSNMR spectra were obtained from InP QDs after 10 days of air exposure (Figure S6). These tests indicated that there should be minimal oxidation over the course of several hours that are required to prepare the samples for SSNMR experiments.

MAS ^{31}P SSNMR spectra were recorded using a Bruker Avance III HD console on a wide-bore 9.4 T magnet (ν_0(^{31}P) = 162.1 MHz). All experiments were performed using a 1.3 mm fast MAS broadband HX SSNMR probe and the rotors were spun with nitrogen gas to prevent additional oxidation of the QDs during the course of the measurements. ^{31}P MAS NMR spectra were obtained using a rotor synchronized Hahn echo (90°-τ-180°-τ-acquire) pulse sequence with continuous wave ^{1}H heteronuclear decoupling applied during acquisition. The pulse widths for 90° and 180° pulses were 1.3 µs and 2.6µs, respectively (192 kHz RF field) and the rotor synchronized τ periods were set such that the total echo delay was 2 rotor cycles. The MAS frequency was 50 kHz in all cases. Fast MAS helps to provide quantitative NMR spectra by eliminating spinning sidebands and focusing signal into the isotropic peaks. The ^{1}H RF power for continuous wave heteronuclear decoupling was set to the HORROR condition [ν_1(^{1}H) = 25 kHz]. All ^{31}P SSNMR spectra were acquired with 500 s recycle delay to ensure there was adequate relaxation delay $\geq 3\times T_1$ to give quantitative SSNMR spectra. This was confirmed by acquiring a ^{31}P SSNMR spectrum of **C**-InP QDs with a 750 s recycle delay, which showed a comparable intensity for the phosphide signal. The spectral width was set to 200 kHz and the number of digitized points to 8 k, corresponding to a total acquisition time of 20.48 ms. ^{31}P spectra were acquired in steps of 32 scans (4.4 hour experiment time), and multiple spectra were acquired until the sum of all spectra provided a spectrum with reasonable signal to noise ratio. Each spectrum was processed by zero filling up to 8k real data points and by adding a simple exponential window function with 1000 Hz line broadening. All data processing was performed on Topspin 3.5.

3.5.3 *X-ray Photoelectron Spectroscopy*

All XPS spectra were taken on a Surface Science Instruments S-Probe photoelectron spectrometer. This instrument has a monochromatized Al Kα X-ray source which was operated at 20 mA and 10 kV and a low-energy electron flood gun for charge neutralization. X-ray analysis area for these acquisitions was approximately 800 μm across. Pressure in the analytical chamber during spectral acquisition was less than 5 x 10^{-9} Torr. All included figures are high-resolution spectra. The pass energy for high-resolution spectra was 50 eV, and data point spacing was 0.065 eV/step. The takeoff angle (the angle between the sample normal and the input axis of the energy analyzer) was 0°. Service Physics Hawk version 7 data analysis software was used to fit high-resolution spectra. The binding energy scale was calibrated from hydrocarbon ligands using the C 1s peak at 284.6 eV. P_{2p} peaks were analyzed using a linear background and fits were constrained with a 0.84 eV splitting value.

All InP samples were drop-cast solutions on a Si wafer while solids were brushed onto a strip of double-sided tape on a Si wafer. Sample preparation was performed in a nitrogen glovebox and transported in sealed containers to the instrument but transfer into the instrument chamber did require a minor degree of exposure to air/moisture.

3.5.4 *General Nanoparticle Characterization*

UV-vis spectra were collected on a Cary 5000 spectrophotometer from Agilent. Fluorescence and absolute quantum yield measurements were taken on a Horiba Jobin Yvon FluoroMax-4 fluorescence spectrophotometer with the QuantaPhi integrating sphere accessory. Quantum dot solids were digested in 67% nitric acid overnight and diluted in 18 MΩ water in order to collect ICP-OES compositional data using a PerkinElmer Optima 8300. Powder X-ray diffraction data was collected on solid films drop-cast onto a Si wafer using a Bruker D8 Discover diffractometer. TEM images were collected on a FEI Tecnai G2 F20 microscope. Samples for TEM imaging were prepared by spotting a 50/50 toluene/pentane solution of nanoparticles onto an ultrathin carbon on holey carbon support film purchased from Ted Pella. Solution NMR spectra were recorded on a 700 MHz Bruker Avance III spectrometer.

All glassware were dried in a 160 °C oven overnight prior to use. All reactions, unless otherwise noted, were run under an inert atmosphere of nitrogen using a glovebox or using standard Schlenk techniques. Myristic acid (≥99%), indium acetate (99.99%), anhydrous acetonitrile (99.8%), trioctylphosphine (97%), tris(diethylamino)phosphine (97%), indium chloride (99.999%), zinc chloride (99.999%), trioctylphosphine oxide (90%), InP (mesh pieces, 99.998%), sulfur powder (99.5% sublimed), and selenium powder (99.99%) were purchased from Sigma-Aldrich Chemical Co. and used without further purification. Diethyl zinc (95%) was purchased from Strem Chemicals and stored in a nitrogen atmosphere glovebox. Toluene was purchased from Sigma Aldrich Chemical Co. was collected from a solvent still and stored over activated 3 Å molecular sieves in a glovebox. 1-octadecene (90%), oleylamine (70%), and squalane (96%) were purchased from Sigma Aldrich Chemical Co. and were dried by stirring overnight with CaH_2, distilled, and stored over activated 3 Å molecular sieves in a glovebox. C_6D_6 was purchased from

Cambridge Isotope Labs and similarly dried and stored. Bio-Beads S-X1 were purchased from Bio-Rad Laboratories and were dried under vacuum before storage in a glovebox. Omni Trace nitric acid was purchased from EMD Millipore. 18.2 MΩ water was collected from an EMD Millipore water purification system. Tris(trimethylsilyl)phosphine was prepared by modifying a literature procedure in which Na-napthalene was used in place of Na/K alloy.[15] Zinc myristate was prepared from diethyl zinc and myristic acid using a modified literature procedure.[57]

3.5.5 *Synthesis of **C**-InP QDs*

C-InP QDs were prepared following a literature procedure[15] in which indium acetate (1. 167 g, 4 mmol) and myristic acid (3.31 g, 14.5 mmol) were heated to 100 °C overnight under reduced pressure in 12 mL of ODE. *$P(SiMe_3)_3$ is a very reactive and pyrophoric source of phosphorus and should be handled with care.* $P(SiMe_3)_3$ (590 μL, 2 mmol) was measured into ODE (5 mL) and injected into the indium myristate solution at 315 °C. Particle growth was maintained at 285 °C and monitored by UV-vis spectroscopy. The reaction was halted by cooling down to room temperature after ca. 20 minutes of growth and the ODE was removed through distillation under reduced pressure. The resulting QD paste was transferred into a glovebox for purification by re-dissolving in a minimal amount of toluene, centrifuging to remove insoluble products, then precipitating the particles with acetonitrile. The flocculated solution was centrifuged at 7,000 rpm and the clear supernatant was discarded. After a single precipitation to remove residual ODE, the particles were dissolved in toluene and purified by gel permeation chromatography (GPC), which has been demonstrated as an effective purification technique for these types of materials.[58,59] For all following quantum dot samples, standard purification entails the removal of high-boiling point solvents through distillation and a combination of precipitation cycles and GPC.

3.5.6 *Synthesis of InP/Zn QDs*

InP/Zn QDs were prepared following a literature procedure using **C**-InP QDs.[60] Briefly, zinc myristate (335 mg, 0.64 mmol) was heated to 80 °C in 5 mL of ODE until the solution was a cloudy white suspension. InP QDs (0.42 mmol of In) suspended in 5 mL of ODE were added to the suspension and heated to 200 °C for 3 hours. Particles were purified by the standard procedure.

3.5.7 *Synthesis of **M**-InP QDs*

First, InP magic-sized clusters (MSCs) were synthesized following a modified preparation from our lab.[43] Indium acetate (5.605 g, 19.2 mmol) and myristic acid (15.9 g, 69.6 mmol) were heated neat at 100 °C under reduced pressure overnight. Dry toluene (50 mL) was added to the reaction flask at room temperature under N_2 the following day, after which $P(SiMe_3)_3$ (2.8 mL, 9.6 mmol) was measured into 10 mL of toluene and injected into the indium myristate solution at 100 °C. Cluster growth was complete within 1 hour as indicated by the characteristic absorbance peak at 386 nm. The particles were concentrated down to a minimal volume of toluene, centrifuged to remove insoluble products, and purified by GPC. Following purification, the absence of free acid was confirmed by ^1H NMR spectroscopy and the MSCs were stored as a solid.

M-InP QDs were synthesized from InP MSCs through a modified procedure.[43] Myristate-capped InP MSCs (60 mg) were dissolved in 3 mL of ODE and transferred to a syringe. In a 3-neck flask under N_2 on a Schlenk line, 12 mL of ODE was heated to 300 °C at which point the MSCs were rapidly injected. Particle growth was held at 285 °C until complete (15-20 minutes) and then cooled down to room temperature. Particles were purified by the standard procedure.

3.5.8 *Synthesis of **A**-InP QDs*

A-InP QDs were synthesized following a modified procedure as described by Brainis *et al*.[47] Indium chloride (50 mg, 0.23 mmol) and zinc chloride (150 mg, 1.1 mmol) were stirred in oleylamine (2.5 mL, 7.5 mmol) under reduced pressure at 120 °C for an hour. The reaction was placed under N_2 and at 180 °C, tris(diethylamino)phosphine (0.23 mL, 0.8 mmol) was injected and particle growth was complete within approximately 20 minutes. After cooling down to room temperature, particles were removed from oleylamine by precipitation with ethanol. GPC purification was performed once particles were re-dissolved in toluene.

3.5.9 *ZnS Shelling of **C**, **M**, and **A**-InP QDs*

ZnS shelling of InP QDs was performed following a modified procedure as described by Peng *et al*.[37] A purified solution of InP QDs (0.04 mmol indium) was dissolved in 7 mL of ODE and heated to 150 °C under inert atmosphere. Initial solutions of InP QDs (**C**, **M**, and **A**) were standardized to each other by matching absorption at 310 nm. Stock solutions of zinc myristate (28.8 mg in 10 mL ODE, 5.6 mM) and sulfur (22.4 mg in 10 mL ODE, 0.07 M) were prepared and heated to 100 °C in Schlenk flasks in an oil bath. For the first monolayer, a 2.17 mL aliquot of the zinc myristate stock (0.012 mmol) was added to the InP particles at 150 °C. After 10 minutes, 170 µL (0.012 mmol) of the sulfur stock solution was added, then the reaction was heated at 220 °C for 30 minutes. The second monolayer was added in the same fashion with 2.89 mL (0.016 mmol) of zinc myristate and 230 µL (0.016 mmol) of sulfur. After 30 minutes at 220 °C, the reaction was cooled down and purified through the standard procedure.

3.5.10 *ZnSe Shelling of **C**, **M**, and **A**-InP QDs*

ZnSe shelling was performed following a modified procedure as described by Brainis *et al*.[47] A purified solution of InP QDs (0.04 mmol indium) was dissolved in 10 mL of squalane and heated to 180 °C. Zinc myristate (100 mg, 0.192 mmol) suspended in squalane was injected and held at 180 °C for 20 minutes. Then, a stoichiometric TOP-Se solution was prepared by sonicating 1.755 g (22.2 mmol) of selenium in 10 mL of TOP (2.23 M) and 87 µL (0.192 mmol) of this stock was slowly injected into the reaction flask. After 140 minutes, a second addition of zinc myristate was added (300 mg, 0.576 mmol). At this point, the reaction was set to 320 °C and during heat-up, the second injection of TOP-Se was added drop-wise (262 µL, 0.576 mmol). Particle luminescence was monitored at 320 °C and the reaction was cooled when the PL ceased to change (ca. 1 hour). Particles were purified using the standard procedure.

3.6 References

(1) Chopra, S. S.; Theis, T. L. Comparative Cradle-to-Gate Energy Assessment of Indium Phosphide and Cadmium Selenide Quantum Dot Displays. Environ. Sci. Nano 2017, 4 (1), 244–254.
(2) Shirasaki, Y.; Supran, G. J.; Bawendi, M. G.; Bulovic, V. Emergence of Colloidal Quantum-Dot Light-Emitting Technologies. Nat Photon 2013, 7 (1), 13–23.
(3) Supran, G. J.; Shirasaki, Y.; Song, K. W.; Caruge, J.-M.; Kazlas, P. T.; Coe-Sullivan, S.; Andrew, T. L.; Bawendi, M. G.; Bulović, V. QLEDs for Displays and Solid-State Lighting. MRS Bull. 2013, 38 (09), 703–711.
(4) Steckel, J. S.; Ho, J.; Hamilton, C.; Xi, J.; Breen, C.; Liu, W.; Allen, P.; Coe-Sullivan, S. Quantum Dots: The Ultimate down-Conversion Material for LCD Displays. J. Soc. Inf. Disp. 2015, 23 (7), 294–305.
(5) Anc, M. J.; Pickett, N. L.; Gresty, N. C.; Harris, J. A.; Mishra, K. C. Progress in Non-Cd Quantum Dot Development for Lighting Applications. ECS J. Solid State Sci. Technol. 2013, 2 (2), 3071–3082.
(6) Jun, S. A.; Jang, E. J.; KWON, S. K.; KIM, T. H.; LEE, W. J. Semiconductor Nanocrystal, and Method of Preparing the Same. US20140117292A1, May 1, 2014.
(7) Kim, S.; Kim, T.; Kang, M.; Kwak, S. K.; Yoo, T. W.; Park, L. S.; Yang, I.; Hwang, S.; Lee, J. E.; Kim, S. K.; et al. Highly Luminescent InP/GaP/ZnS Nanocrystals and Their Application to White Light-Emitting Diodes. J. Am. Chem. Soc. 2012, 134 (8), 3804–3809.

(8) Lim, J.; Bae, W. K.; Lee, D.; Nam, M. K.; Jung, J.; Lee, C.; Char, K.; Lee, S. InP@ZnSeS, Core@Composition Gradient Shell Quantum Dots with Enhanced Stability. Chem. Mater. 2011, 23 (20), 4459–4463.
(9) Tamang, S.; Lincheneau, C.; Hermans, Y.; Jeong, S.; Reiss, P. Chemistry of InP Nanocrystal Syntheses. Chem. Mater. 2016, 28 (8), 2491–2506.
(10) Jasinski, J.; Leppert, V. J.; Lam, S.-T.; Gibson, G. A.; Nauka, K.; Yang, C. C.; Zhou, Z.-L. Rapid Oxidation of InP Nanoparticles in Air. Solid State Commun. 2007, 141 (11), 624–627.
(11) Cros-Gagneux, A.; Delpech, F.; Nayral, C.; Cornejo, A.; Coppel, Y.; Chaudret, B. Surface Chemistry of InP Quantum Dots: A Comprehensive Study. J. Am. Chem. Soc. 2010, 132 (51), 18147–18157.
(12) Virieux, H.; Le Troedec, M.; Cros-Gagneux, A.; Ojo, W.-S.; Delpech, F.; Nayral, C.; Martinez, H.; Chaudret, B. InP/ZnS Nanocrystals: Coupling NMR and XPS for Fine Surface and Interface Description. J. Am. Chem. Soc. 2012, 134 (48), 19701–19708.
(13) Ramasamy, P.; Kim, B.; Lee, M.-S.; Lee, J.-S. Beneficial Effects of Water in the Colloidal Synthesis of InP/ZnS Core–Shell Quantum Dots for Optoelectronic Applications. Nanoscale 2016, 8 (39), 17159–17168.
(14) Kim, K.; Yoo, D.; Choi, H.; Tamang, S.; Ko, J.-H.; Kim, S.; Kim, Y.-H.; Jeong, S. Halide–Amine Co-Passivated Indium Phosphide Colloidal Quantum Dots in Tetrahedral Shape. Angew. Chem. Int. Ed. 2016, 55 (11), 3714–3718.
(15) Gary, D. C.; Cossairt, B. M. Role of Acid in Precursor Conversion During InP Quantum Dot Synthesis. Chem. Mater. 2013, 25 (12), 2463–2469.
(16) Xie, L.; Harris, D. K.; Bawendi, M. G.; Jensen, K. F. Effect of Trace Water on the Growth of Indium Phosphide Quantum Dots. Chem. Mater. 2015, 27 (14), 5058–5063.
(17) Baquero, E. A.; Virieux, H.; Swain, R. A.; Gillet, A.; Cros-Gagneux, A.; Coppel, Y.; Chaudret, B.; Nayral, C.; Delpech, F. Synthesis of Oxide-Free InP Quantum Dots: Surface Control and H2-Assisted Growth. Chem. Mater. 2017, 29 (22), 9623–9627.
(18) Xi, L.; Cho, D.-Y.; Besmehn, A.; Duchamp, M.; Grützmacher, D.; Lam, Y. M.; Kardynał, B. E. Effect of Zinc Incorporation on the Performance of Red Light Emitting InP Core Nanocrystals. Inorg. Chem. 2016, 55 (17), 8381–8386.
(19) Buffard, A.; Dreyfuss, S.; Nadal, B.; Heuclin, H.; Xu, X.; Patriarche, G.; Mézailles, N.; Dubertret, B. Mechanistic Insight and Optimization of InP Nanocrystals Synthesized with Aminophosphines. Chem. Mater. 2016, 28 (16), 5925–5934.
(20) Berends, A. C.; van der Stam, W.; Hofmann, J. P.; Bladt, E.; Meeldijk, J. D.; Bals, S.; de Mello Donega, C. Interplay between Surface Chemistry, Precursor Reactivity, and Temperature Determines Outcome of ZnS Shelling Reactions on CuInS2 Nanocrystals. Chem. Mater. 2018, 30 (7), 2400–2413.
(21) Holden, W. M.; Hoidn, O. R.; Ditter, A. S.; Seidler, G. T.; Kas, J.; Stein, J. L.; Cossairt, B. M.; Kozimor, S. A.; Guo, J.; Ye, Y.; et al. A Compact Dispersive Refocusing Rowland Circle X-Ray Emission Spectrometer for Laboratory, Synchrotron, and XFEL Applications. Rev. Sci. Instrum. 2017, 88 (7), 073904.
(22) Holden, W.; Seidler, G. T.; Cheah, S. Sulfur Speciation in Biochars by Very High Resolution Benchtop Kα X-Ray Emission Spectroscopy. J. Phys. Chem. A 2018.
(23) Petric, M.; Kavčič, M. Chemical Speciation via X-Ray Emission Spectroscopy in the Tender X-Ray Range. J. Anal. At. Spectrom. 2016, 31 (2), 450–457.

(24) Petric, M.; Bohinc, R.; Bučar, K.; Žitnik, M.; Szlachetko, J.; Kavčič, M. Chemical State Analysis of Phosphorus Performed by X-Ray Emission Spectroscopy. Anal. Chem. 2015, 87 (11), 5632–5639.
(25) Alonso Mori, R.; Paris, E.; Giuli, G.; Eeckhout, S. G.; Kavčič, M.; Žitnik, M.; Bučar, K.; Pettersson, L. G. M.; Glatzel, P. Electronic Structure of Sulfur Studied by X-Ray Absorption and Emission Spectroscopy. Anal. Chem. 2009, 81 (15), 6516–6525.
(26) Kavčič, M.; Petric, M.; Vogel-Mikuš, K. Chemical Speciation Using High Energy Resolution PIXE Spectroscopy in the Tender X-Ray Range. Nucl. Instrum. Methods Phys. Res. Sect. B Beam Interact. Mater. At. 2018, 417, 65–69.
(27) Kavčič, M.; Karydas, A. .; Zarkadas, C. Chemical State Analysis of Sulfur in Samples of Environmental Interest Using High Resolution Measurement of Kα Diagram Line. Nucl. Instrum. Methods Phys. Res. Sect. B Beam Interact. Mater. At. 2004, 222 (3–4), 601–608.
(28) Pollock, C. J.; DeBeer, S. Insights into the Geometric and Electronic Structure of Transition Metal Centers from Valence-to-Core X-Ray Emission Spectroscopy. Acc. Chem. Res. 2015, 48 (11), 2967–2975.
(29) Kowalska, J.; DeBeer, S. The Role of X-Ray Spectroscopy in Understanding the Geometric and Electronic Structure of Nitrogenase. Biochim. Biophys. Acta BBA - Mol. Cell Res. 2015, 1853 (6), 1406–1415.
(30) Pollock, C. J.; DeBeer, S. Valence-to-Core X-Ray Emission Spectroscopy: A Sensitive Probe of the Nature of a Bound Ligand. J. Am. Chem. Soc. 2011, 133 (14), 5594–5601.
(31) Lancaster, K. M.; Roemelt, M.; Ettenhuber, P.; Hu, Y.; Ribbe, M. W.; Neese, F.; Bergmann, U.; DeBeer, S. X-Ray Emission Spectroscopy Evidences a Central Carbon in the Nitrogenase Iron-Molybdenum Cofactor. Science 2011, 334 (6058), 974–977.
(32) Mori, R. A.; Paris, E.; Giuli, G.; Eeckhout, S. G.; Kavčič, M.; Žitnik, M.; Bučar, K.; Pettersson, L. G. M.; Glatzel, P. Sulfur-Metal Orbital Hybridization in Sulfur-Bearing Compounds Studied by X-Ray Emission Spectroscopy. Inorg. Chem. 2010, 49 (14), 6468–6473.
(33) Lee, N.; Petrenko, T.; Bergmann, U.; Neese, F.; DeBeer, S. Probing Valence Orbital Composition with Iron Kβ X-Ray Emission Spectroscopy. J. Am. Chem. Soc. 2010, 132 (28), 9715–9727.
(34) Bergmann, U.; Horne, C. R.; Collins, T. J.; Workman, J. M.; Cramer, S. P. Chemical Dependence of Interatomic X-Ray Transition Energies and Intensities – a Study of Mn Kβ″ and Kβ2,5 Spectra. Chem. Phys. Lett. 1999, 302 (1–2), 119–124.
(35) Baquero, E. A.; Ojo, W.-S.; Coppel, Y.; Chaudret, B.; Urbaszek, B.; Nayral, C.; Delpech, F. Identifying Short Surface Ligands on Metal Phosphide Quantum Dots. Phys. Chem. Chem. Phys. 2016, 18 (26), 17330–17334.
(36) Tomaselli, M.; Yarger, J. L.; Bruchez, M.; Havlin, R. H.; deGraw, D.; Pines, A.; Alivisatos, A. P. NMR Study of InP Quantum Dots: Surface Structure and Size Effects. J. Chem. Phys. 1999, 110 (18), 8861–8864.
(37) Xie, R.; Battaglia, D.; Peng, X. Colloidal InP Nanocrystals as Efficient Emitters Covering Blue to Near-Infrared. J. Am. Chem. Soc. 2007, 129 (50), 15432–15433.
(38) Battaglia, D.; Peng, X. Formation of High Quality InP and InAs Nanocrystals in a Noncoordinating Solvent. Nano Lett. 2002, 2 (9), 1027–1030.
(39) Ramasamy, P.; Ko, K.-J.; Kang, J.-W.; Lee, J.-S. Two-Step “Seed-Mediated” Synthetic Approach to Colloidal Indium Phosphide Quantum Dots with High-Purity Photo- and Electroluminescence. Chem. Mater. 2018.

(40) Cervilla, A.; Pérez-Pla, F.; Llopis, E.; Piles, M. Unusual Oxidation of Phosphines Employing Water as the Oxygen Atom Source and Tris(Benzene-1,2-Dithiolate)Molybdenum(VI) as the Oxidant. A Functional Molybdenum Hydroxylase Analogue System. Inorg. Chem. 2006, 45 (18), 7357–7366.
(41) Gary, D. C.; Glassy, B. A.; Cossairt, B. M. Investigation of Indium Phosphide Quantum Dot Nucleation and Growth Utilizing Triarylsilylphosphine Precursors. Chem. Mater. 2014, 26 (4), 1734–1744.
(42) Gary, D. C.; Flowers, S. E.; Kaminsky, W.; Petrone, A.; Li, X.; Cossairt, B. M. Single-Crystal and Electronic Structure of a 1.3 Nm Indium Phosphide Nanocluster. J. Am. Chem. Soc. 2016, 138 (5), 1510–1513.
(43) Gary, D. C.; Terban, M. W.; Billinge, S. J. L.; Cossairt, B. M. Two-Step Nucleation and Growth of InP Quantum Dots via Magic-Sized Cluster Intermediates. Chem. Mater. 2015, 27 (4), 1432–1441.
(44) Tessier, M. D.; Dupont, D.; Nolf, K. D.; Roo, J. D.; Hens, Z. Economic and Size-Tunable Synthesis of InP/ZnE (E = S, Se) Colloidal Quantum Dots. http://pubs.acs.org/doi/abs/10.1021/acs.chemmater.5b02138 (accessed Feb 28, 2018).
(45) Tessier, M. D.; De Nolf, K.; Dupont, D.; Sinnaeve, D.; De Roo, J.; Hens, Z. Aminophosphines: A Double Role in the Synthesis of Colloidal Indium Phosphide Quantum Dots. J. Am. Chem. Soc. 2016, 138 (18), 5923–5929.
(46) Li, Z.; Ji, Y.; Xie, R.; Grisham, S. Y.; Peng, X. Correlation of CdS Nanocrystal Formation with Elemental Sulfur Activation and Its Implication in Synthetic Development. J. Am. Chem. Soc. 2011, 133 (43), 17248–17256.
(47) Chandrasekaran, V.; Tessier, M. D.; Dupont, D.; Geiregat, P.; Hens, Z.; Brainis, E. Nearly Blinking-Free, High-Purity Single-Photon Emission by Colloidal InP/ZnSe Quantum Dots. Nano Lett. 2017, 17 (10), 6104–6109.
(48) Reid, K. R.; McBride, J. R.; Freymeyer, N. J.; Thal, L. B.; Rosenthal, S. J. Chemical Structure, Ensemble and Single-Particle Spectroscopy of Thick-Shell InP–ZnSe Quantum Dots. Nano Lett. 2018, 18 (2), 709–716.
(49) Gong, K.; Kelley, D. F. Lattice Strain Limit for Uniform Shell Deposition in Zincblende CdSe/CdS Quantum Dots. J. Phys. Chem. Lett. 2015, 6 (9), 1559–1562.
(50) Nasilowski, M.; Spinicelli, P.; Patriarche, G.; Dubertret, B. Gradient CdSe/CdS Quantum Dots with Room Temperature Biexciton Unity Quantum Yield. Nano Lett. 2015, 15 (6), 3953–3958.
(51) Jeong, B. G.; Park, Y.-S.; Chang, J. H.; Cho, I.; Kim, J. K.; Kim, H.; Char, K.; Cho, J.; Klimov, V. I.; Park, P.; et al. Colloidal Spherical Quantum Wells with Near-Unity Photoluminescence Quantum Yield and Suppressed Blinking. ACS Nano 2016, 10 (10), 9297–9305.
(52) Bae, W. K.; Padilha, L. A.; Park, Y.-S.; McDaniel, H.; Robel, I.; Pietryga, J. M.; Klimov, V. I. Controlled Alloying of the Core–Shell Interface in CdSe/CdS Quantum Dots for Suppression of Auger Recombination. ACS Nano 2013, 7 (4), 3411–3419.
(53) Frenette, L. C.; Krauss, T. D. Uncovering Active Precursors in Colloidal Quantum Dot Synthesis. Nat. Commun. 2017, 8 (1), 2082.
(54) Liu, H.; Owen, J. S.; Alivisatos, A. P. Mechanistic Study of Precursor Evolution in Colloidal Group II−VI Semiconductor Nanocrystal Synthesis. J. Am. Chem. Soc. 2007, 129 (2), 305–312.

(55) Holden, W. M.; Hoidn, O. R.; Seidler, G. T. A Color X-Ray Camera for 2 – 6 KeV Using a Back-Illuminated Mass-Produced CMOS Sensor. J Instrum 2018, In preparation.

(56) Newville, M.; Stensitzki, T.; Allen, D. B.; Ingargiola, A. Lmfit: Non-Linear Least-Square Minimization And Curve-Fitting For Python. Zenodo September 21, 2014.

(57) Glassy, B. A.; Cossairt, B. M. Ternary Synthesis of Colloidal Zn3P2 Quantum Dots. Chem. Commun. 2015, 51, 5283–5286.

(58) Shen, Y.; Gee, M. Y.; Tan, R.; Pellechia, P. J.; Greytak, A. B. Purification of Quantum Dots by Gel Permeation Chromatography and the Effect of Excess Ligands on Shell Growth and Ligand Exchange. Chem. Mater. 2013, 25 (14), 2838–2848.

(59) Roberge, A.; Stein, J. L.; Shen, Y.; Cossairt, B. M.; Greytak, A. B. Purification and In Situ Ligand Exchange of Metal-Carboxylate-Treated Fluorescent InP Quantum Dots via Gel Permeation Chromatography. J. Phys. Chem. Lett. 2017, 8 (17), 4055–4060.

(60) Stein, J. L.; Mader, E. A.; Cossairt, B. M. Luminescent InP Quantum Dots with Tunable Emission by Post-Synthetic Modification with Lewis Acids. J. Phys. Chem. Lett. 2016, 7 (7), 1315–1320.

Chapter 4. Cation Exchange Induced Transformation of InP Magic-Sized Clusters

Article was adapted with permission from Chemistry of Materials. Copyright 2017 American Chemical Society

4.1 Note for Collaborative Work

My undergraduate student at the time, Molly Steimle, was an immense help in the initial stages of this project. She spent countless hours preparing and purifying sample for me and was an excellent companion to have for the summer. All theoretical calculations were performed by Dr. Alessio Petrone, working under Professor Xiaosong Li in the Department of Chemistry at the University of Washington. Alessio was a true pleasure to work with and his efforts are greatly appreciated. PDF measurements and analysis were performed by Maxwell Terban working under Professor Simon Billinge, in the Department of Applied Physics and Applied Mathematics at Columbia University. PDF measurements were conducted at Brookhaven National Laboratory.

4.1 Introduction

Cation exchange is a widely-utilized tool for accessing colloidal nanomaterials with unique or emergent properties that may be difficult to directly synthesize using conventional nucleation and growth mechanisms. This facile reaction employs the anionic sublattice as a template while cations partially or fully exchange, typically retaining the original crystallite size and shape. Experimental conditions have been developed to access a wide variety of doped nanocrystals,[1–4] anisotropic structures,[5–8] alloyed nanocrystals,[4,9,10] nanocrystalline heterostructures,[10–13] and semiconductor nanocrystals that are synthetically challenging to produce *via* a direct route.[14]

Chemists have continued to develop this technique by extracting general design principles through examination of ion exchange thermodynamics and consideration of the shared similarities with solid-state ion exchange occurring over a reaction zone, and by probing mechanism using a combination of theory, dynamic simulations, and experiment.[15–23]

Magic-sized clusters (MSCs) represent the interface between small molecules and quantum-confined nanostructures. MSCs are atomically-precise clusters with elevated thermodynamic stability compared to structures of similar size that can play a role in nanocrystal nucleation and growth.[24] MSCs may serve as a unique tool for studying both the mechanism and structural consequences of cation exchange in nanoscale materials because of their perfect monodispersity and the homogeneity of their surface chemistry. Utilizing clusters as models to provide insight into the nature of cation exchange in nanocrystals has most recently been demonstrated by the Jain group in their examination of the progression of CdSe MSCs to Cu_2Se clusters.[25] Due to the presence of a metastable cluster intermediate, they demonstrated that the Cd^{2+} sublattice experienced reorganization to a six-coordinate structure upon initial introduction of Cu^+ dopant ions. The six-coordinate structure had a greater affinity for further Cu^+ dopants, supporting the co-operative nature of cation exchange observed in the analogous nanocrystal-scale reaction.[25,26] This work adds to the growing body of information on cation exchange in metal chalcogenide lattices,[16,18] however much remains to be explored with other lattice types.

Among the few reports of cation exchange in non-chalcogenide lattices,[11,27–29] Beberwyck and Alivisatos reported the use of Cd_3P_2 and Cd_3As_2 quantum dots as templates to In/Ga pnictides through cation exchange and highlighted the significant differences that exist between ion exchange reactions in nanocrystal lattices with different levels of ionic and covalent character.[14] While many II-VI ion exchange reactions can be performed reversibly at room temperature, the

III-V reactions shown in their work were irreversible and required sequential exchanges at higher temperatures to drive the reaction to completion, with Cd^{2+} cations remaining in the final material even under optimized conditions. Interested in learning more about cation exchange in phosphide lattices, we sought to extend the MSC approach to this system.

Recently, a diffraction quality single crystal of $In_{37}P_{20}(O_2CCH_2Ph)_{51}$, an InP MSC, was isolated and structurally characterized to reveal a strained $[In_{21}P_{20}]^{3+}$ inorganic core ligated by 16 additional indium atoms and an interconnected network of 51 bidentate and mostly bridging carboxylate ligands.[30] Our lab has observed that the InP MSC displays site selective reactivity when exposed to moist air, leading to a carboxylate ligand shift (bidentate to monodentate) in order to accommodate a water molecule bound to an indium. To explore this site-selective modification further, we examined the reactivity of the InP MSC in the presence of other Lewis bases; exposure to primary amines indicated that these ligands initiate indium carboxylate desorption and ultimately lead to structural rearrangement of the cluster.[31] Thus, utilizing InP MSCs as templates for cation exchange reactions towards new cluster materials with the ability to predict the progression of the reaction was of great interest to us.

4.2 Results and Discussion

Herein we report the transformation of InP MSCs to Cd_3P_2 MSCs at room temperature where full conversion to Cd_3P_2 can be achieved at a 500:1 excess of cadmium carboxylate per InP cluster. The final product is physically and electronically indistinguishable from the Cd_3P_2 MSC prepared independently from molecular precursors (Figure 4.1).[32] The Cd_3P_2 MSC is characterized by narrow absorption and emission features at 450 and 455 nm, respectively, and weak band-edge photoluminescence (<3% quantum yield). Although the crystal structure of Cd_3P_2 MSCs is unknown, it is characteristically different from the bulk tetragonal crystal.[32,33] To probe potential intermediates during this cation exchange process, the reaction between $In_{37}P_{20}(O_2CCH_2Ph)_{51}$, ($O_2CCH_2Ph$ = PA), with stoichiometric amounts of cadmium carboxylate was monitored. Using a combination of optical and nuclear magnetic resonance (NMR) spectroscopy together with a variety of structural and analytical characterization tools, we outline the step-wise mechanism by which InP MSCs undergo cation exchange with Cd^{2+} (Figure 4.2).

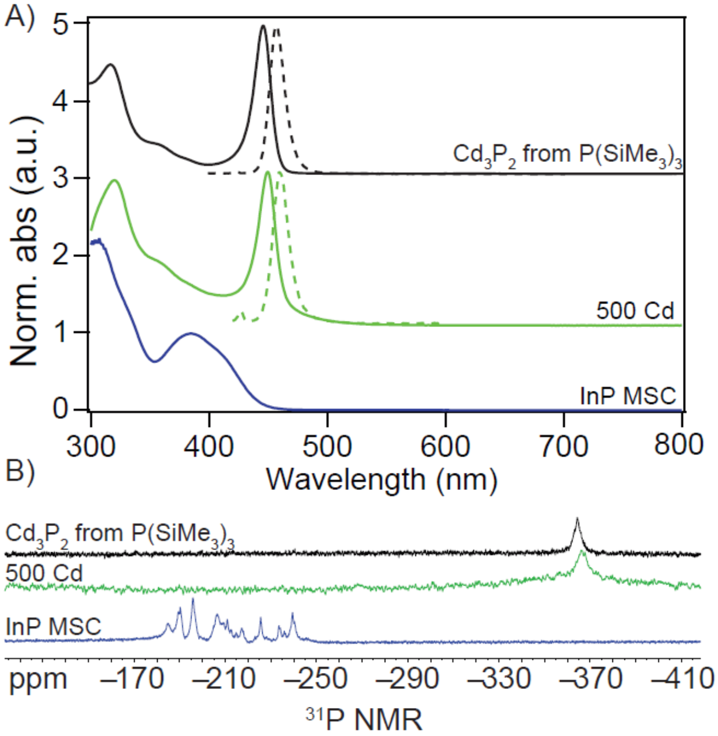

Figure 4.1. UV-Vis and ^{31}P NMR spectra of Cd_3P_2 synthesized via injection of $P(SiMe_3)_3$, Cd_3P_2 via cation exchange, and InP MSCs. Structurally, the ^{31}P NMR of Cd_3P_2 clusters via $P(SiMe_3)_3$ injection and cation exchange have a peak at –366 and –364 ppm, respectively, which demonstrates the similarity in phosphorus environments.

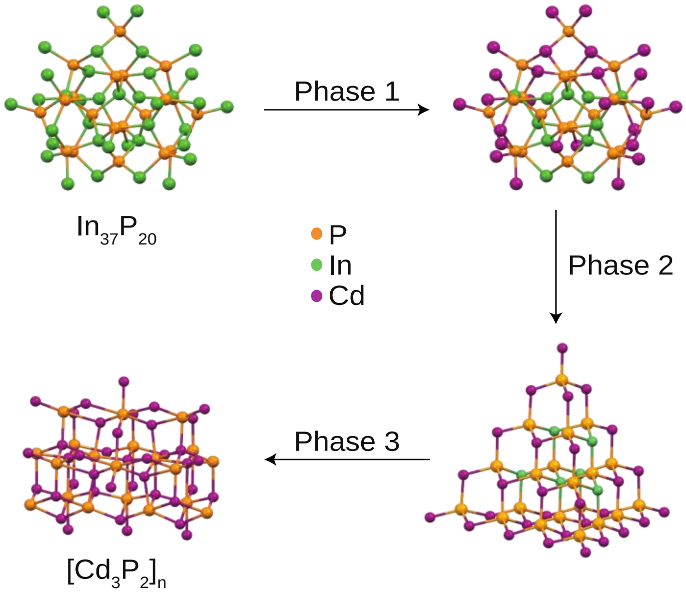

Figure 4.2. Proposed mechanism of the conversion of InP MSCs to Cd_3P_2 MSC *via* cation exchange. Three distinct phases are proposed: phase 1 is a topotactic process that is dominated by Z-type ligand exchange, phase 2 involves a relaxation of the strained cluster lattice on further incorporation of cadmium, and phase 3 is the final structural transformation that accompanies complete exchange of cadmium for indium in the lattice. The Cd_3P_2 MSC has an unknown crystal structure, thus the authors have chosen to visually represent the final structure as a tetragonal portion derived from the bulk Cd_3P_2 lattice (pdf #01-070-3099 ICSD).

We propose that cation exchange is initiated through Z-type ligand exchange between indium and cadmium carboxylates. Z-type ligands (Lewis acids or two-electron acceptors) have been shown to reversibly bind and exchange with anionic sites on nanocrystal surfaces with no impact on crystal structure or strain, although both examples are isovalent cases in which ligand density remains unchanged.[34,35] This initial topotactic phase (phase 1) conserves the structure of the $In_{21}P_{20}$ charged core while the metal carboxylates on the surface undergo exchange. We then observe relaxation of the crystal lattice to a structure consistent with a zinc blende assignment, which we designate as phase 2. Through the addition of excess Cd^{2+}, we hypothesize that increasing amounts of cadmium replacing indium in the core induces structural relaxation of the initially strained pseudo-tetrahedral coordination environments. Finally, phase 3 is characterized by the distinct transition to Cd_3P_2 which can occur abruptly with no indication of an intermediate product.*Phase 1: Topotactic Cation Exchange*

The evolution of the absorption spectra as cadmium phenylacetate ($Cd(PA)_2$) was progressively added to a solution of $In_{37}P_{20}(PA)_{51}$ is shown in Figure 4.3. Each spectrum in this titration represents the thermodynamic endpoint of the reaction between the two reagents at a given cadmium concentration at room temperature. Although absorbance measurements do not provide insight on the precise structural changes occurring, they are a diagnostic fingerprint of the cluster evolution. During phase 1, the InP MSC peak at 386 nm is broadened with a more pronounced shoulder at 430 nm that is present up to 37 equivalents of $Cd(PA)_2$. ^{31}P NMR has proven to be a useful tool to examine structural evolution of the cluster because the unique phosphorus environments in the *pseudo*-C_2-symmetric $In_{37}P_{20}(O_2CCH_2Ph)_{51}$ cluster have allowed peak assignment based on chemical shielding arguments and integration, and may be telling of specific site reactivity with cadmium.[31] With one equivalent of cadmium, the original anionic sublattice appears to be maintained with slight changes in the chemical shielding tensors as is expected upon a change in surface ligation (Figure 4.4). The addition of up to 5 equivalents lead to a broadening and slight upfield shift of all resonances. In accordance with the characteristic chemical shift of Cd_3P_2 MSCs at –364 ppm, we suggest that the upfield shift is evidence for the formation of cadmium-phosphorus bonds.

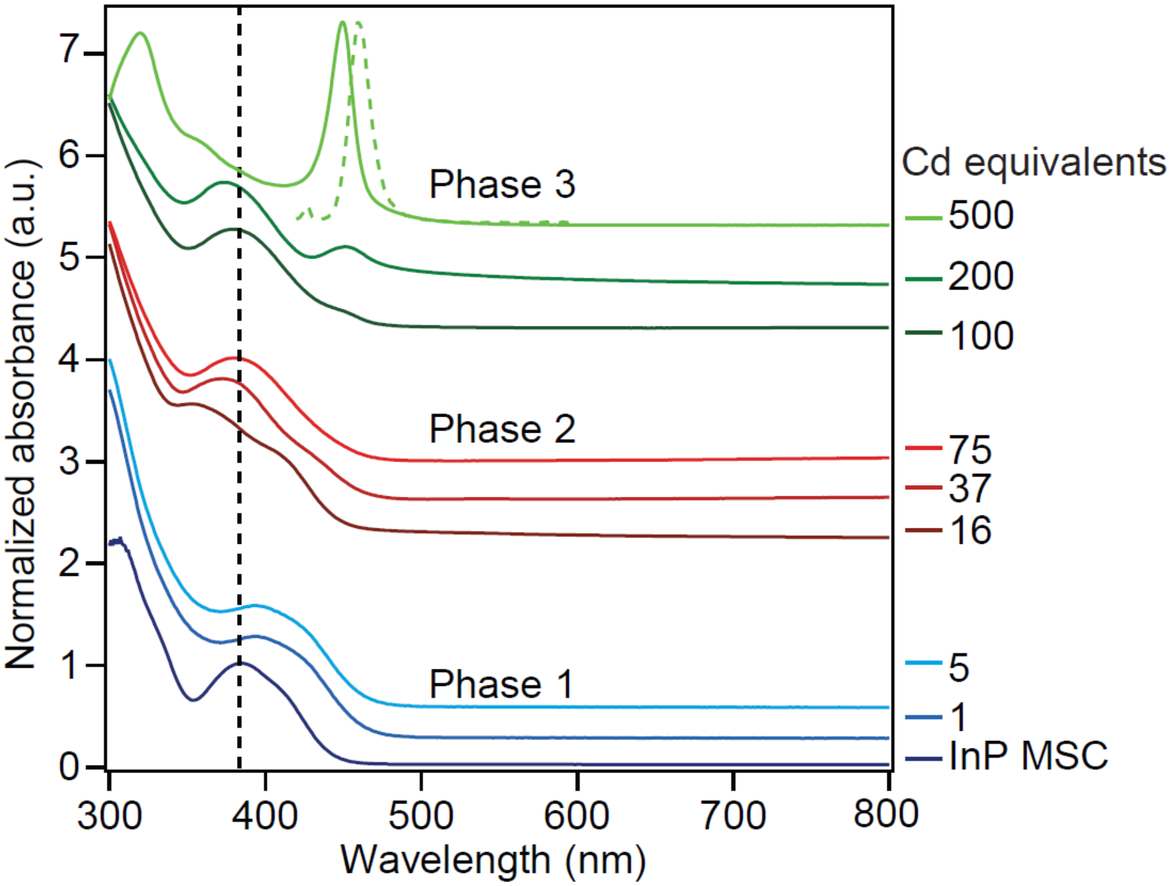

Figure 4.3. UV-Vis absorbance traces (solid, offset) of InP MSCs exposed to increasing equivalents of $Cd(PA)_2$ relative to a single InP MSC. Photoluminescence of Cd_3P_2 final product (dashed). The dashed black line is to direct the eye towards the shift from the initial InP MSC peak at 386 nm.

Elemental analysis was necessary to help corroborate the spectroscopic data and more importantly, to confirm that cadmium was coordinating to the cluster. To purify the samples of excess metal carboxylate, multiple rounds of gel permeation chromatography were carried out with the purification endpoint confirmed by unchanging molar ratios upon analysis by inductively coupled plasma optical emission spectrometry (ICP-OES). The molar ratios extracted from ICP-OES analysis are shown in Table 3.4 and have all been normalized to 20 P to allow comparison with the composition of the initial $In_{37}P_{20}$ cluster. These data support the hypothesis that the core $[In_{21}P_{20}]^{3+}$ composition is maintained up to the addition of 16 equivalents of $Cd(PA)_2$ with the surface indium atoms being progressively replaced by cadmium.

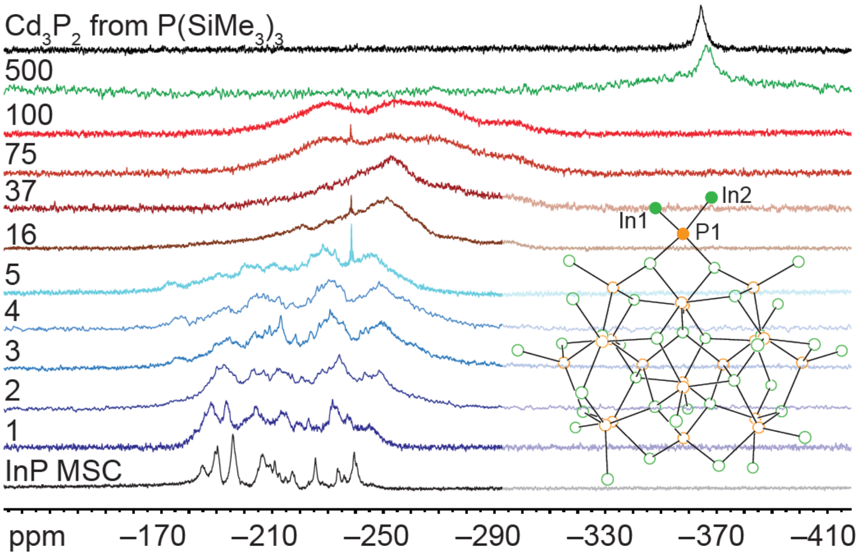

Figure 4.4. ^{31}P NMR (283.5 MHz, C_6D_6) spectra of clusters and increasing cadmium equivalents taken at room temperature. Trace colors correspond to the assignment of phase 1, 2, or 3. The sharp peak at –240 ppm is a PH_3 impurity (< 0.1% of total P). Inset of $In_{37}P_{20}(PA)_{51}$ crystal highlighting apical indium atoms with ligands removed for clarity

Table 4.11. Molar ratios of InP, intermediate, and Cd_3P_2 cluster species by ICP-OES.

Sample	**Cd**	**In**	**P**
$In_{37}P_{20}$	0	40	20
1	1.8	46	20
5	12	34	20
16	28	28	20
37	55	36	20
75	82	33	20
100	68	28	20
200	69	5	20
Cd_3P_2 **via $P(SiMe_3)_3$**	60	0	20

Additionally, matrix-assisted laser desorption/ionization coupled with time-of-flight mass spectrometry (MALDI-TOF) was performed on the InP MSC and on the Cd-treated intermediates (Figure 4.5). Due to the unknown nature of how the clusters fragment, the broad distributions of fragment masses were analyzed with Gaussian fits to extract characteristic trends (

Table 4.12). The InP MSC shows a parent fragment ion with m/z 8570, as seen in similar ranges previously for mass spectral characterization of InP clusters,[36] with the narrowest Gaussian distribution (FWHM = 980). The mass of an intact fully ligated cluster is 11,759 g/mol so we expect that a portion of the surface ligands are lost in fragmentation. While the mass distribution consistently broadens, the addition of ≤16 equivalents of Cd^{2+} results in no significant change in the parent fragment ion mass. Consistent with the ICP-OES interpretation, this suggests the parent fragment ion is unaffected by initial surface cation exchange. While the former data certainly suggest that the original cluster crystal remained intact, more precise structural characterization was necessary to ascertain whether this phase was topotactic in nature.

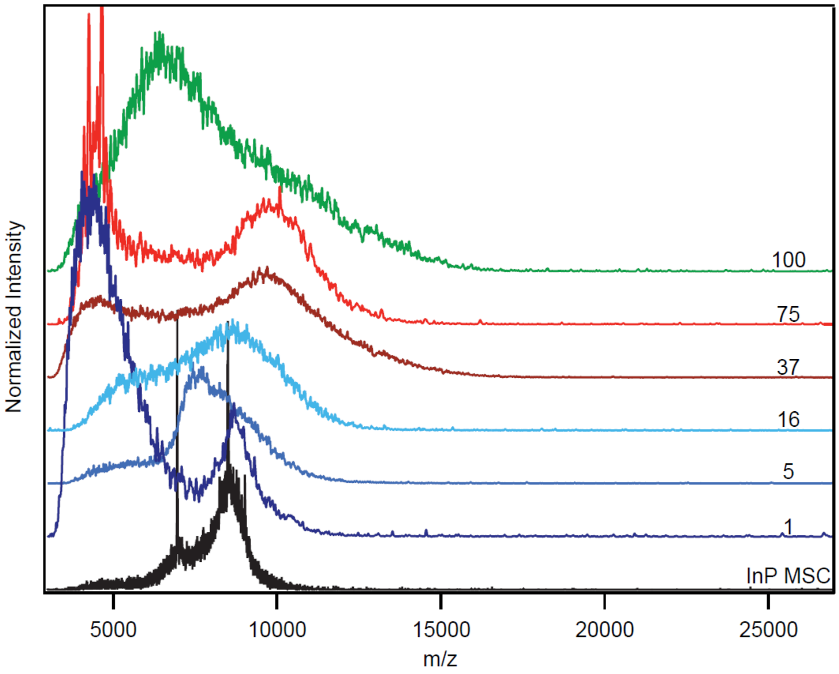

Figure 4.5. Low-mass MALDI-TOF spectra of purified InP MSC and cluster intermediates. No signal was measured for Cd_3P_2. The InP MSC has a distinct and reproducible single peak at 8500 m/z that we hypothesize corresponds to a $[In_{31}P_{20}(O_2CCH_2Ph)_{32}]^+$ fragment.

Table 4.12. Gaussian fit results performed on MALDI-TOF mass spectra.

Sample	**Peak position (m/z)**	**FWHM**
$In_{37}P_{20}$	8570	980
1	8638	2031
5	8390	2752
16	8573	3679
37	9531	4873
75	9786	3053
100	9398	5841

Comparing the physical structures of cadmium-coated or cadmium-alloyed intermediates is possible through powder X-ray diffraction (pXRD) and atomic pair distribution function (PDF) analysis. PDF has previously been used to reveal that InP MSCs with different ligand sets (phosphonate terminated vs carboxylate terminated) have very different internal structures.[37] PDF analysis of $In_{37}P_{20}$ and the resulting Cd-treated products demonstrates that the core structure is maintained up to the addition of 16 equivalents of $Cd(PA)_2$ (Figure 4.6, Figure 4.7). Furthermore, we used the predicted structure of $Cd_{16}In_{21}P_{20}$, in which the 16 surface indium were exchanged with cadmium, to simulate the PDF. This computed pattern correctly predicts many of the minor changes experimentally measured by the cluster reacted with 16 equivalents of cadmium (Figure S4). Direct analysis of the pXRD data demonstrates that no shifts are present that would correspond to additional lattice strain/relaxation or alloying. In fact, the powder diffraction pattern of InP MSCs already differs from larger QDs and bulk InP due to the low-symmetry and strain present in the core thus pXRD can be very telling of changes in the InP cluster lattice.[30]

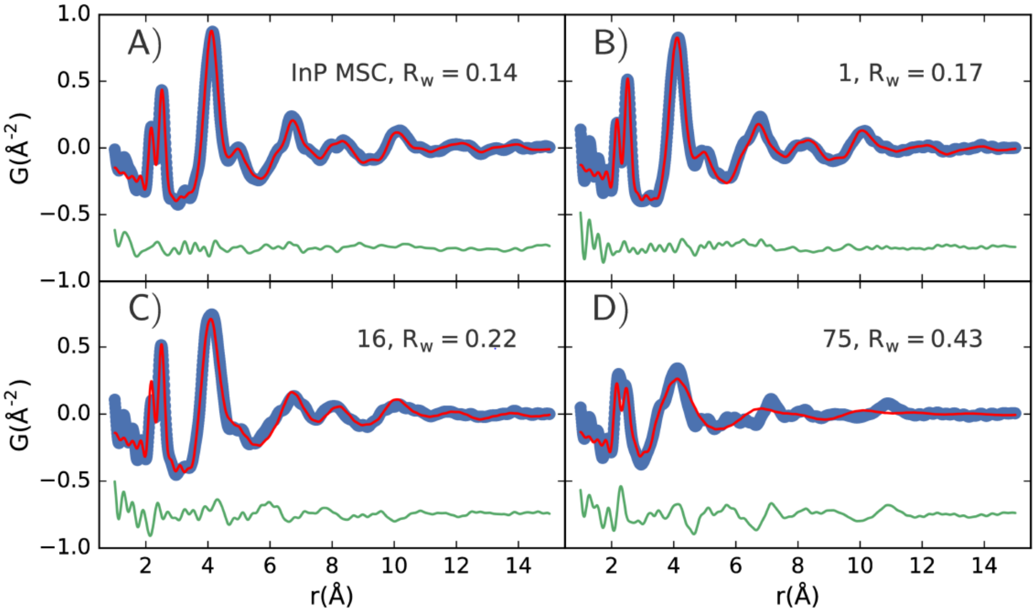

Figure 4.6. Comparison of simulated PDFs from refinement of the InP cluster structure to the measured samples A) pure InP MSC, B) 1 equiv. Cd^{2+}, C) 16 equiv., and D) 75 equiv. The fit is very good for the pure InP clusters but becomes less good for 1 and 16 respectively. This shows that while the overall structure is maintained, some reorientation is taking place as a small amount of cadmium is exchanged. For 75 equivalents, it is clear that the fit is very poor, indicating that some critical concentration of Cd^{2+} has been exchanging inducing a drastic restructuring of the InP cluster structure.

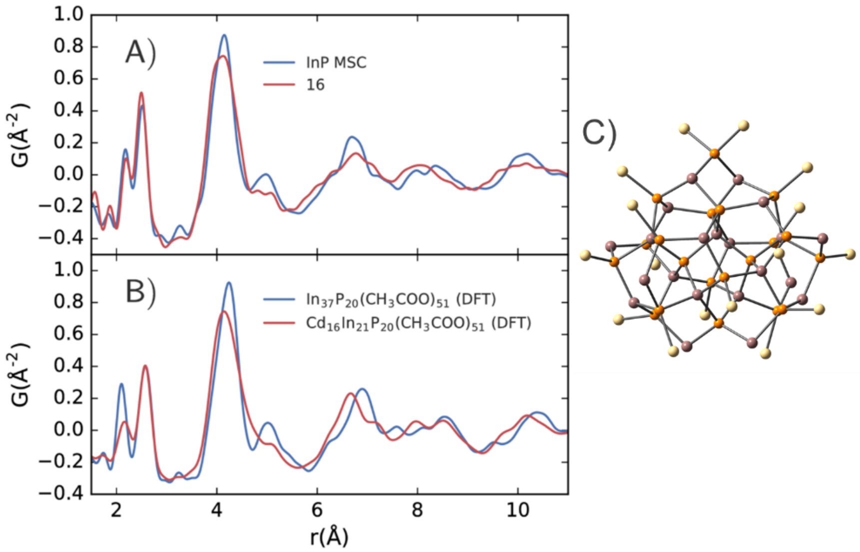

Figure 4.7. Comparison of the structural changes from pure InP to 16 equivalents Cd^{2+} (A) shown by changes in the measured PDF and compared to (B) the simulated PDFs from structures predicted using the HSE06/LANL2DZ $Cd_{16}In_{21}P_{20}(O_2CCH_3)_{35}(HO_2CCH_3)_2$ optimized cluster (C). For the PDF from the 16 Cd-containing optimized cluster, we see that it correctly predicts an up-shift and loss of intensity in the first peak at about 2.17 Å (the O-In or O-Cd peak). It also predicts the down-shift and broadening of the large peak at 4.1 Å, and significant broadening of the smaller one at 5.0 Å. The higher regions also match fairly well in the broadening and slight downshift of the peaks at about 8.5 Å and 10.0 Å. Ball and stick representation of the HSE06/LANL2DZ $Cd_{16}In_{21}P_{20}$ optimized cluster has ligands removed for clarity (Cd-yellow, In-grey purple, P-orange).

The data thus far suggests that cation exchange occurs in a topotactic fashion, conserving the structure of the inorganic core. We expect that the exchange initially takes place at the most reactive indium sites, especially because these reactions are performed at room temperature. More specifically, based on our prior work with the addition of Lewis bases to InP MSCs,[31] we envision cation exchange beginning with Z-type ligand exchange to replace the apical indium atoms (In1/2 in Figure 4.4).

Computational analysis of an InP cluster with cadmium replacing the apical indium (In1/In2) resulted in a slight red-shifted absorbance shoulder, consistent with our experimental observations (Figure 4.8). In comparison, the model where equatorial indium atoms were exchanged by cadmium leads to a calculated absorbance spectrum with a significantly red-shifted lowest energy electronic transition (Figure 4.8). In this last model, the Cd^{2+} atoms are now situated in the physical region where most of the electronic density of the HOMO is spatially localized (Figure 4.9) and therefore the two electronic transitions responsible for the first peak absorption (HOMO-1 to LUMO and HOMO to LUMO) are strongly impacted. These data are indicative that cation exchange likely begins by Z-type ligand exchange at these apical sites while the structure of the phosphide sublattice is largely unperturbed. Without a diffraction quality single crystal, it is difficult to identify whether some cadmium has intercalated into the $[In_{21}P_{20}]^{3+}$ core before stoichiometric exchange on the surface has completed but we hypothesize that it would be a minor amount before the next phase of the cation exchange process occurs, which involves a structural rearrangement (phase 2).

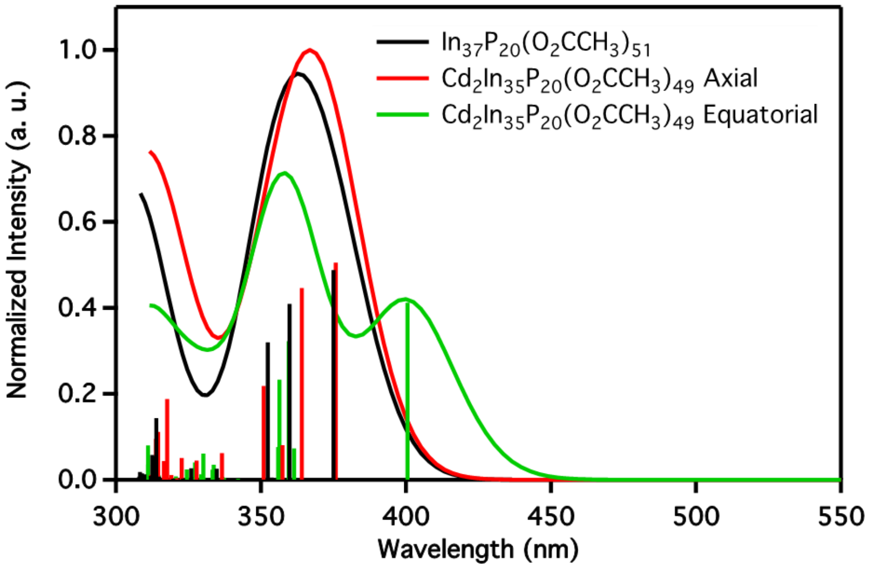

Figure 4.8. TD-HSE06/LANL2DZ optical spectra obtained from the first 10 individual optical transitions for the optimized acetate analog structures $In_{37}P_{20}(O_2CCH_3)_{51}$ (black) and the ones where two In were replaced by two Cd atoms and two carboxylate ligands, the closest to the substituted atoms, were removed to preserve the charge compensation, $Cd_2In_{35}P_{20}(O_2CCH_3)_{49}$. The substitution strategy mostly retained the molecular symmetry, therefore in the resulting models two In atoms, located either on top of the pseudo C_2 symmetry axis (namely axial and spectrum in red) of the molecule or in the plane (namely equatorial and spectrum in green) orthogonal to this axis, were replaced by two Cd atoms, respectively. A Gaussian smoothing function (width 0.12 eV) has been used and all intensities are normalized respect to the highest peak in the figure. Only the transitions relative to the first peaks have been shown for clearness.

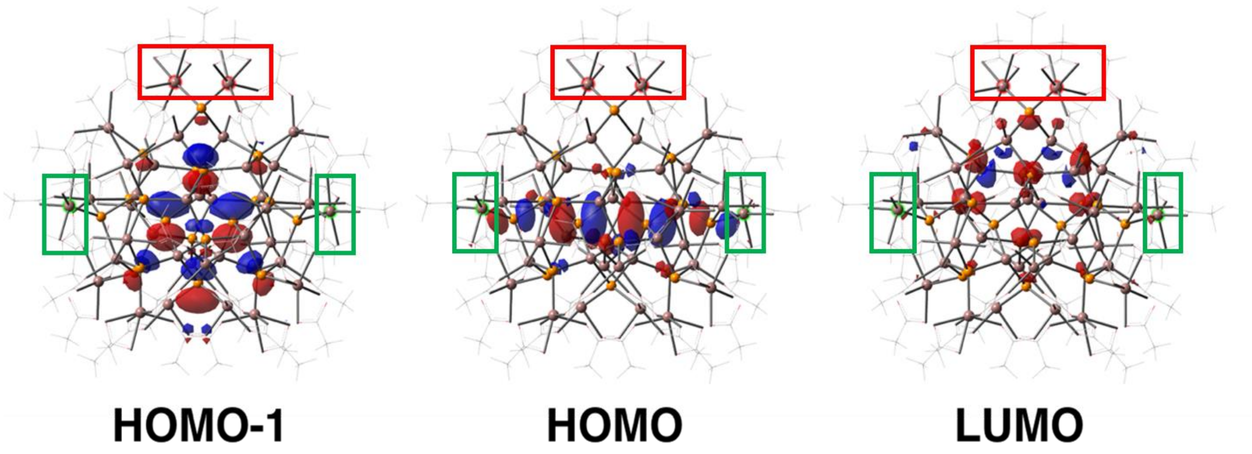

Figure 4.9. HSE06/LANL2DZ molecular orbital (MO) diagrams of the occupied (HOMO-1 and HOMO) and unoccupied (LUMO) orbitals involved in the two brightest transitions calculated for the optimized acetate analog structure $In_{37}P_{20}(O_2CCH_3)_{51}$. The positions used to build the Cd doped models are also highlighted in red (axial) and green (equatorial) in the figure, respectively. The MOs were plotted with an isosurface value of 0.025.

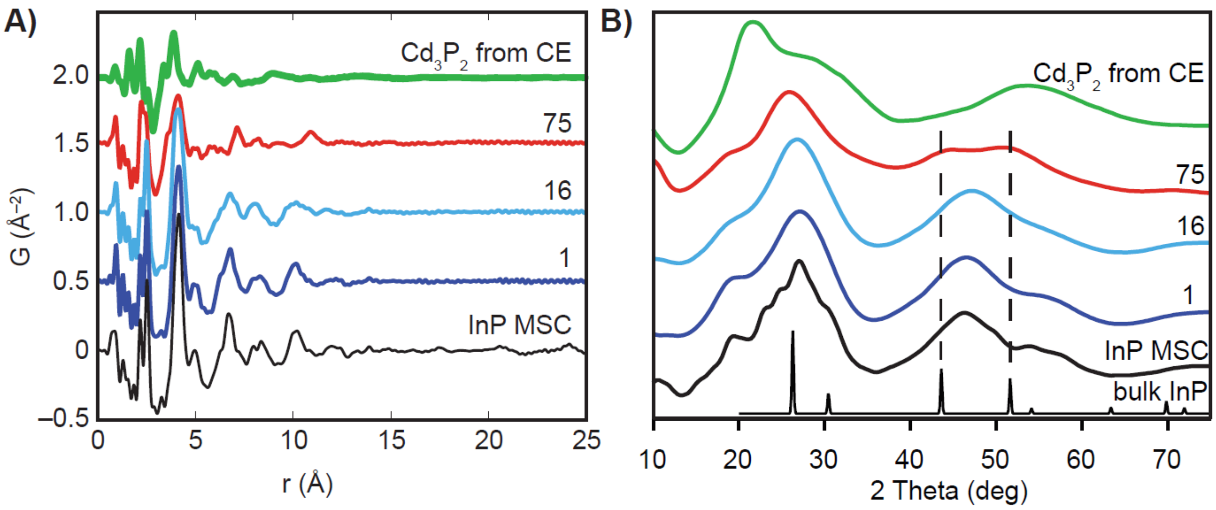

Figure 4.10. (A) Measured PDFs for the series of InP MSCs with increasing equivalents of cadmium added starting with pure InP. (B) powder X-ray diffraction patterns of corresponding PDF samples with bulk InP (pdf #01-073-1983 ICSD).

4.2.2 *Phase 2: Structural Relaxation*

We categorize phase 2 as a distinct event due to the structural changes observed by PDF and XRD. By 75 equivalents of Cd^{2+}, alteration of the scattered intensities and drastic changes in the PDF signal indicate structural reconstruction, suggesting the exchange of cadmium into the core (Figure 4.10). Furthermore, this PDF matches well with a zinc blende tetrahedron containing 35 Cd and 20 P atoms, similar to that seen for CdSe MSCs (Figure 4.11).[38] PXRD analysis suggests that the lattice has relaxed to a zinc blende structure (represented by the bulk InP powder diffraction pattern) with major reflections at 26, 43.6 and 51.6 2θ, correlating with the PDF fits.

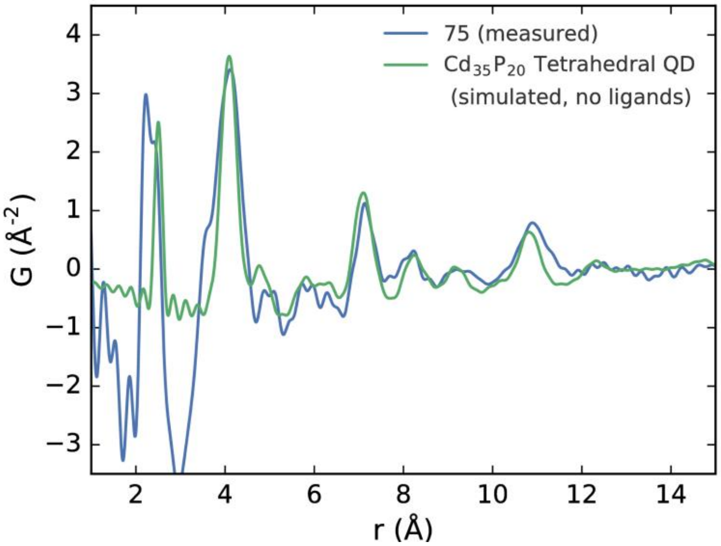

Figure 4.11. The measured PDF for the 75 Cd^{2+} cluster sample compared to the PDF simulated from the CdSe tetrahedral structure[38] where Se atoms have been replaced with P, and the structure has been isotropically contracted to best match the measured signal. We see that it matches the measurement well, while the missing peaks at low-*r* likely result from O-Cd and O-P correlations from the ligands.

Absorbance measurements show that above 37 equivalents of cadmium, the excitonic feature blue-shifts to an intermediate that is reproducibly observed between 360-370 nm depending on the specific identity of the ligand (Figure 4.3). By ^{31}P NMR spectroscopy, this phase is not characterized by precisely defined phosphorus chemical environments, rather we observe a continuous upfield shift and broadening of all resonances as the cadmium content in the phosphide sublattice continues to increase (Figure 4.4). This may indicate that cadmium exchange into the core is non-selective, giving rise to a range of structures in which varying specific indium atoms have been replaced by cadmium. Quantitative ^{31}P NMR spectroscopy indicates that the amount of phosphorus contained in these cluster species is conserved through the course of the cation exchange, supporting an anionic rearrangement step without anion loss (Figure 4.12). The presence of additional cadmium is verified by compositional analysis in which the molar ratios show an increasing amount of cadmium. Further interpretation of the ICP data is somewhat unclear (likely due to the presence of a large excess of cation loosely interacting with the cluster surface),[39,40] but suggests that significant concentrations of indium remain in the sample with super-stoichiometric addition of $Cd(PA)_2$. Mass spectrometry supports the incorporation of additional cadmium at higher concentrations in which a domain of larger masses is observed, relative to the phase 1 mass distributions (Figure 4.5, Table 4.12,). The mass of the parent fragment ion rises by approximately 1 kDa and remains nearly invariable thereafter, consistent with a structural change initiated above 16 equivalents of Cd^{2+} that impacts the cluster fragmentation.

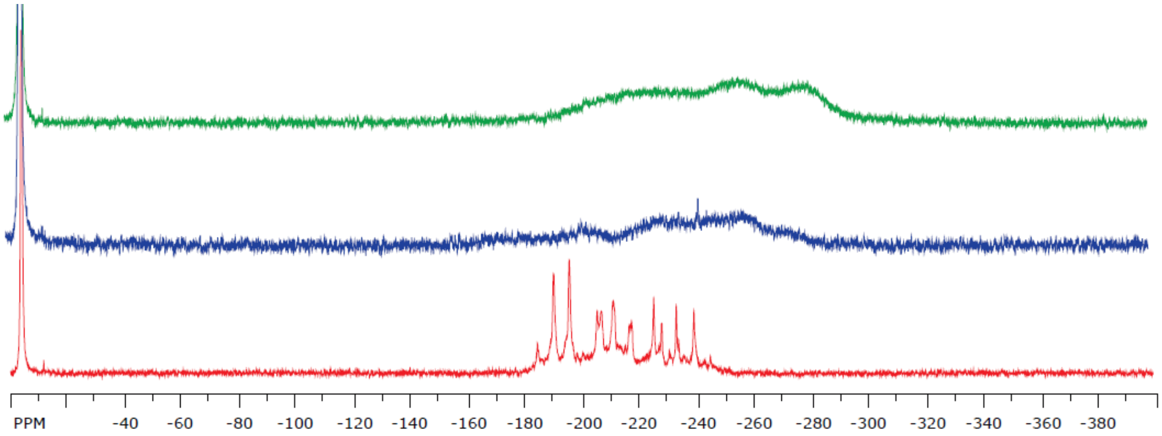

Figure 4.12. ^{31}P NMR (283.5 MHz, room temperature, C_6D_6) spectra taken of InP MSC (red), 5 equivalents Cd^{2+} (blue), and 75 equivalents Cd^{2+} (green) with triphenylphosphine. Delay time was 20 seconds. Integrated areas corresponded to $3.53x10^{-5}$, $2.63\ x10^{-5}$, and $2.98\ x10^{-5}$ moles of phosphorus in the InP MSC, 5 equiv. Cd^{2+}, and 75 equiv. Cd^{2+}, respectively, demonstrating the majority of P remains in the cluster species.

Although we attribute the progression of cluster species in phase 2 as a continuation of cation exchange between core indium and cadmium that results in structural reorganization to a relaxed zinc blende species, the pathway by which this occurs is still unknown. Accounting for the difference in charge additionally introduces complications in assigning a diffusion pathway, beyond surface-related exchanges, through interstitial sites or by a vacancy-assisted mechanism.[7,15,23] The extent of a detailed mechanistic examination is beyond the scope of this current study but certainly of interest to the authors.

4.2.3 *Phase 3: Reconstruction to Cd_3P_2*

At high equivalents of $Cd(PA)_2$ (100, 200, and 500 equivalents), a new absorbance feature at 450 nm appears in the UV-Vis spectrum (Figure 4.3), which is characteristic of a known Cd_3P_2 MSC.[32] The InP cluster has negligible room temperature photoluminescence (PL) but once conversion to Cd_3P_2 is complete, weak band-edge PL (<1% quantum yield) is measured. In order to compare the Cd_3P_2 produced *via* cation exchange (CE), Cd_3P_2 clusters were independently synthesized following the literature procedure described by Yu and co-workers with slight modifications.[32] Briefly, cadmium carboxylate was dissolved in toluene and $P(SiMe_3)_3$ was injected at room temperature. The reaction proceeded at room temperature but could be carried out up to 120 °C.

Monitoring the *in-situ* growth of Cd_3P_2 following $P(SiMe_3)_3$ injection supports a homogeneous growth mechanism with a continuous increase in cluster size towards the thermodynamically stable product with an absorption maximum at 450 nm (Figure 4.13a). Slight shifts in the absorption maxima occur depending on the precise identity of the supporting ligands (oleate or phenylacetate). Monitoring the *in-situ* synthesis of Cd_3P_2 *via* introduction of 500 equivalents Cd^{2+} to InP MSCs also shows a continuous transition from the InP MSCs to the Cd_3P_2 MSCs with no observable intermediates (Figure 4.13b) and demonstrates that InP MSCs do not re-dissolve to form new Cd-P monomers. This continuous growth appeared to conflict with the evolution of absorbance features at <100 equivalents Cd^{2+}, but we hypothesize that a supersaturated solution of Cd^{2+} with InP MSCs likely precludes the buildup of any kinetic products and that rapid exchange and rearrangement occurs without cluster dissolution. Notably, if the stable phase 2 intermediate with diagnostic UV-Vis absorption at 360/370 nm formed by addition of 75 equivalents Cd^{2+} is treated with additional Cd^{2+}, a continuous progression towards Cd_3P_2 is observed, demonstrating that the intermediates are viable precursors on the pathway towards Cd_3P_2 (Figure 4.14). The alternative possibility that clusters re-dissolve in the presence of excess cadmium to form a short-lived monomer species was strongly considered, but the lack of spectroscopic evidence, especially from *in-situ* absorbance measurements, lead us to the conclusion that the crystal lattice is conserved during rearrangement.

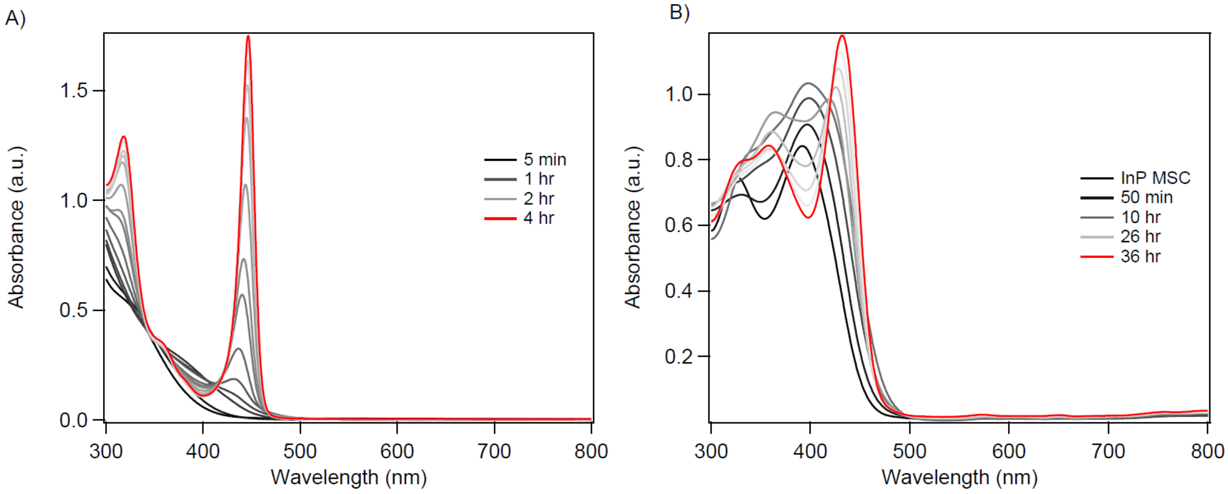

Figure 4.13. (A) In-situ UV-Vis measurements of Cd_3P_2 demonstrating that growth proceeds through continuous size increases. Clusters were synthesized by room-temperature injection of $P(SiMe_3)_3$ into $Cd(OA)_2$ (OA = oleate) dissolved in toluene. (B) In-situ monitoring of InP MSC in the presence of 200 excess $Cd(OA)_2$ also shows a continuous red-shift towards Cd_3P_2 without any apparent dissolution of clusters

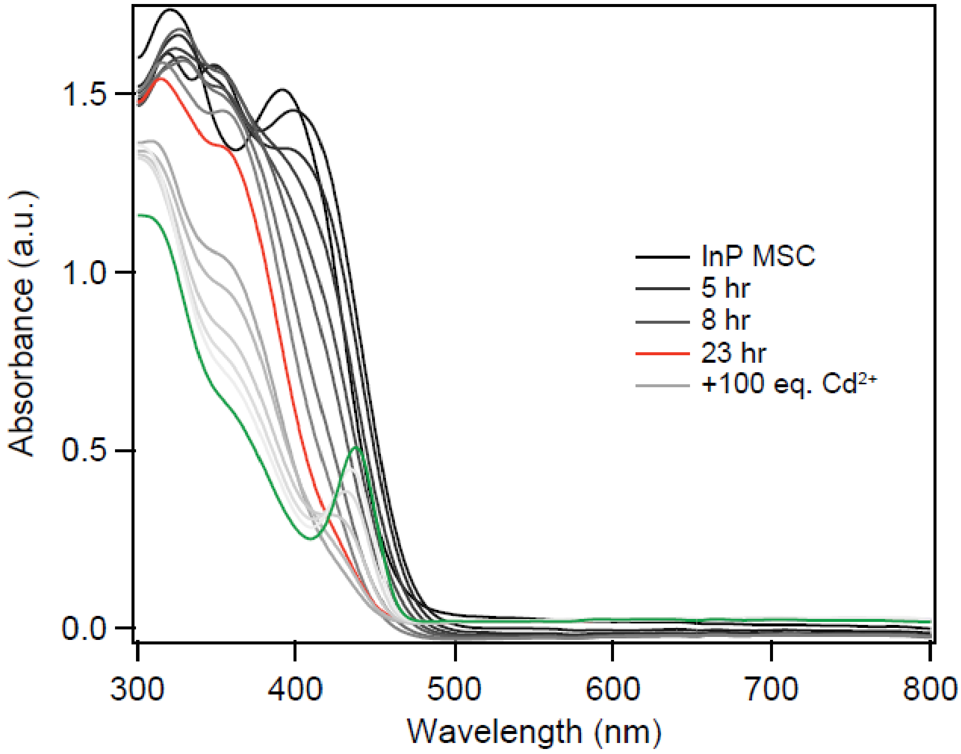

Figure 4.14. In-situ UV-Vis measurements showing that intermediate cluster species are likely on-path to Cd_3P_2 formation. 75 equivalents of $Cd(OA)_2$ are added to InP MSCs which formed a stable intermediate at 360 nm (red). After allowing the reaction to equilibrate, 100 equivalents of $Cd(OA)_2$ dissolved in toluene was added to the solution (dilution decreased the measured intensity) which drove the product towards Cd_3P_2 (green).

Structurally, the two products are comparable by ^{31}P NMR spectroscopy (Figure 4.1). Cd_3P_2 clusters synthesized by $P(SiMe_3)_3$ injection show a single peak in the ^{31}P NMR spectrum at –364 ppm, consistent with literature reports,[32] which indicates that the Cd_3P_2 cluster has a very symmetric structure with contributions to the broad linewidth likely arising from differences in surface and core Cd-P environments. The final Cd_3P_2 product produced by cation exchange has a single peak at –366 ppm demonstrating that there are likely no residual In-P bonds remaining. As expected, following purification, the composition of *in-situ* synthesized and cation exchange produced Cd_3P_2 are nearly identical with the presence of a negligible amount of indium in the cation exchange sample (Table 4.11).

Since the bulk and cluster phosphorus NMR differ greatly, it is no surprise that by pXRD the measured pattern does not overlay well with the reported bulk Cd_3P_2 patterns (Figure 4.15).[32,33] This is consistent with previous characterization of the Cd_3P_2 cluster, which shows a similarly broad powder pattern.[32,41] Previous measurements of Zn_3P_2 nanocrystal powder diffraction patterns, which shares the tetragonal lattice, have shown a divergence from the bulk structure at small nanocrystal sizes, consistent with the complexity of the 40-atom tetragonal unit cell.[42,43] Furthermore, PDF analysis indicates that the final product of cation exchange is demonstrably different from the other measured samples, indicating a final structural transformation has occurred on complete conversion to Cd_3P_2 (Figure 4.10, Figure 4.16). Although the use of transmission electron microscopy (TEM) would help reveal changes in particle morphology throughout this transformation, the poor contrast of InP and sub-2 nm particles limits the application of this technique.[37,44]

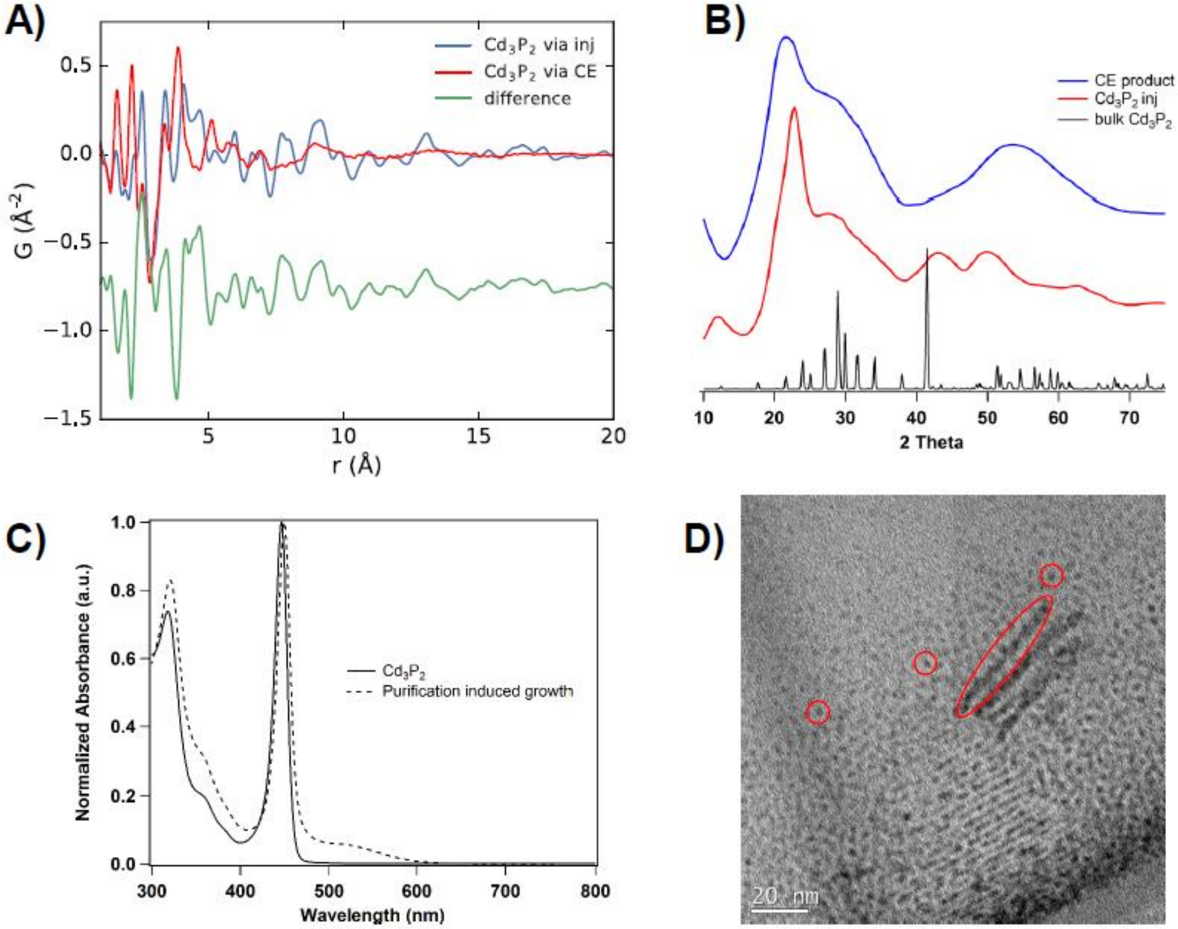

Figure 4.15. (A) PDF measurement of two Cd_3P_2 samples. Cd_3P_2 via CE is consistent with the expected cluster size with the signal diminishing by 15-20 angstroms. The sample produced via monomer injection has signal corresponding to larger nanocrystalline content. During purification, multiple re-dissolution and precipitation cycles can unintentionally induce growth to larger nanoparticles as seen by a color change and red-shifted shoulder in the absorbance spectrum (C). (C) and (D) are measurements of Cd_3P_2 via $P(TMS)_3$ injection but the same type of partial growth was observed for Cd_3P_2 clusters produced via cation exchange after several cycles of purification. Assumedly, ligand binding strength on Cd_3P_2 is weak enough that purification strips off stabilizing ligands. The powder diffraction pattern (B) of these samples also shows less broad

peaks indicating larger particles are present. Some features similar to the cluster are conserved in this pattern (broad peak 30-35 2θ) but the pattern still does not overlay with bulk Cd_3P_2. D) TEM images of the purified nanocrystalline Cd_3P_2 particles (representative examples highlighted in red) shows striations in the dispersity of particles and even nanorods (outlined in red) that appear to have formed as a result of cluster assembly. We hypothesize that Cd_3P_2 anisotropic shapes are a product of both ligand removal and irradiation under the electron beam and the resulting dipole induces preferential coordination among opposite facets.

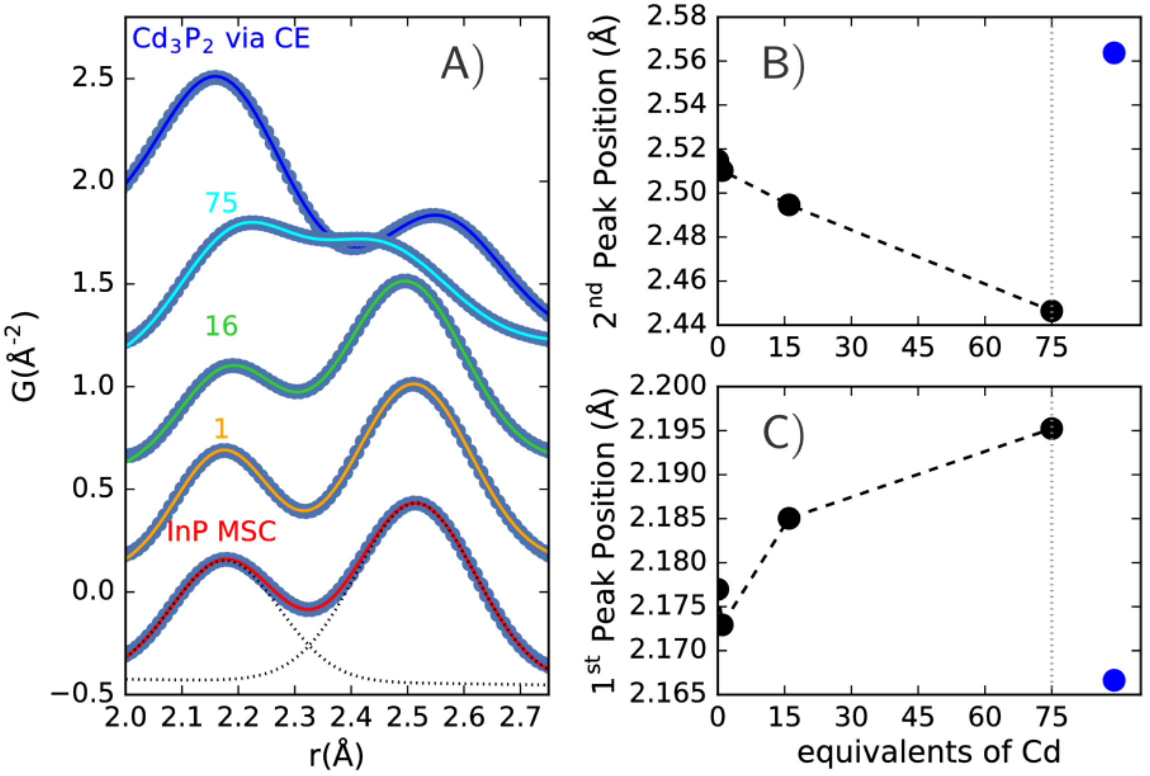

Figure 4.16. (A) The first two peaks in the measured PDFs shown for the sample series InP, 1, 16, 75, and Cd_3P_2. The two peaks have been fit with two Gaussians and a sloping baseline to track the change of the bond lengths with Cd^{2+} exchange. The peak positions found from the fitting are shown for the second peak (B) and first peak (C). We see a roughly monotonic change from InP through 75 Cd^{2+}, but there is a drastic change going to Cd_3P_2.

4.2.4 *Unique Reactivity of InP MSC*

In many examples of cation exchange reactions, hard-soft acid-base theory is used to design experimental conditions that will favor the extraction of the Lewis acid from the solid to solution in cases where the formation energy of the desired product is favored.[15,18] This technique was utilized by Beberwyck and Alivisatos to irreversibly produce InP QDs from Cd_3P_2 QDs at high temperatures in tandem with the addition of soft Lewis bases.[14] In our work, the formation of Cd_3P_2 occurs at room temperature from InP MSCs, which we propose is driven by the formation of the more stable Cd_3P_2 cluster. Under harsher synthetic conditions, the structural integrity of the cluster anionic sublattice is completely disrupted. Analogous to the room temperature reactions, varying concentrations of cadmium heated to 100 °C with InP MSCs produce what are likely alloyed nanoparticles due to the decrease of the bandgap with increasing amounts of cadmium (Figure 4.17). The distinction between InP MSC and QDs is that the inherent strain present in the InP MSC lattice likely lends itself to significantly different reactivity relative to a crystalline QD. Each phase discussed previously involves to some degree a surface reorganization or structural reconstruction that we propose corresponds to an energetic stabilization from the distorted InP MSC lattice.

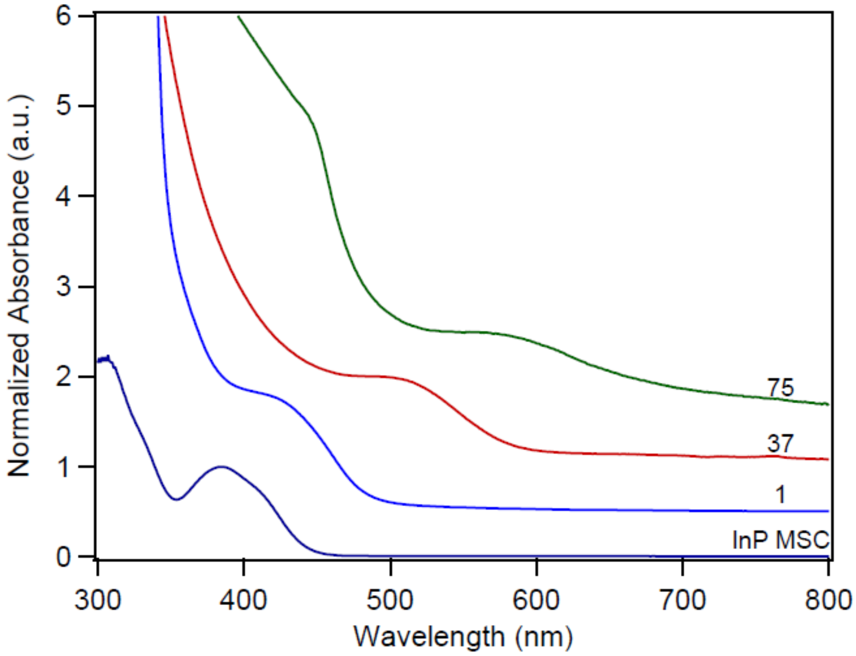

Figure 4.17. Stacked UV-Vis traces of final reaction products of 1 (blue), 37 (red), and 75 (green) equivalents of cadmium oleate were added to InP MSC at room temperature in toluene and immediately heated to 100 °C. This series of reactions demonstrates the difference in products if heat is added and shows the loss of clusters in favor of polydisperse nanocrystalline products. The band gap differences between InP (1.34 eV) and Cd_3P_2 (0.55 eV) support our hypothesis that increasing the cadmium content leads to alloyed nanoparticles.

Evidence for the presence of significant strain in the InP MSC in provided by analysis of the metrical parameters from the single crystal X-ray diffraction data and is consistent with observed shifts in the measured powder diffraction pattern which show that the lattice is only pseudo-tetrahedral.[30] X-ray photoelectron spectroscopy (XPS) demonstrates the differences between nanocrystalline and cluster-sized InP as well. The In 3d region shown in Figure 4.18 shows a distinct asymmetric peak shape with a main peak at 445.4 eV and a shoulder at 448.0 eV, diverging from the typical Gaussian line shape common to InP QDs.[45,46] This is mirrored in the second feature resulting from spin-orbit splitting, indicating these features arise from the indium core electrons. As more Cd^{2+} reacts with the cluster, the shoulder shifts to lower binding energies and diminishes. This trend is also observed in the Cd 3d spectra (Figure 4b). Previous reports of core/shell and alloyed structures have described a similar shoulder peak, in which the presence of peak asymmetry corresponds to the presence of a different "surface" component as seen in InP/ZnS[47] and multiple other materials.[48–50]

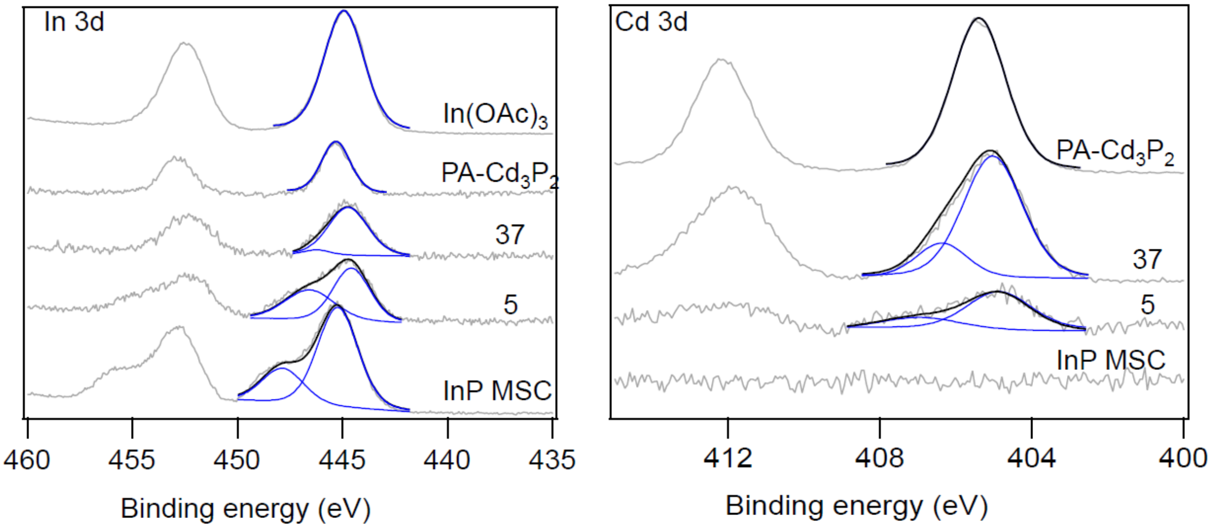

Figure 4.18. Experimental intensity (black dashed) and fitted profile (red/blue solid) of core level In 3d and Cd 3d. Samples are InP MSCs, 5 and 37 equivalents of Cd^{2+}, and PA-Cd_3P_2 is a product of cation exchange with 200 equivalents of $Cd(PA)_2$. Peak fits and atomic percentages are in Table 4.13.

Table 4.13. XPS fits (binding energy and atomic percentage) of In 3d and Cd 3d spectra.

	In 3d		**Cd 3d**	
	BE	atomic %	BE	atomic %
$In(O_2CCH_3)_3$	444.9	100		
InP	445.4	73.5		
	448	26.5		
5 Cd	444.7	57.1	405	70.3
	446.7	42.9	407.1	29.7
16 Cd	445.2	75.6		
	447.2	24.4		
37 Cd	444.8	93.9	405	80.6
	446.3	6.1	406.4	19.3
PA-Cd_3P_2	445.4	100	405.5	100

We hypothesize that the inherent strain of the $[In_{21}P_{20}]^{3+}$ core contributes to diversifying the surface and core components. As structural rearrangement proceeds towards a more symmetric, and presumably less strained Cd_3P_2 structure, the differences between core and surface environments is significantly reduced, leading to coalescence of the signal to one peak in the final Cd_3P_2 MSC. It should be noted that while the final phenylacetate-ligated Cd_3P_2 cluster obtained by CE exhibits some signal from indium, compositional analysis of this sample indicates almost negligible concentrations of indium in the sample, which is likely present as loosely associated metal carboxylates.

The reversibility of the cation exchange reaction has been examined as well, further supporting our claim that InP MSCs exist in a higher energy state and re-formation of the original structure is unlikely. Interestingly, addition of In^{3+} to solutions of purified Cd_3P_2 clusters does lead to reaction consistent with indium incorporation, but the observed products are distinct from the intermediates we've characterized here likely due to the nature of the structural evolution described in Scheme 1 (Figure 4.19, Figure 4.20).

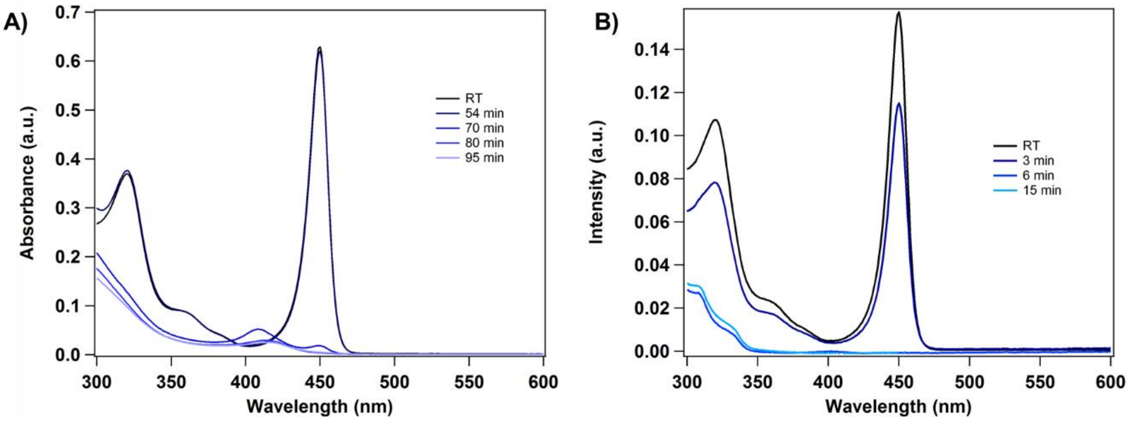

Figure 4.19. UV-Vis spectra of $In(OA)_3$ (A-approx. a 1:1 In:Cd molar ratio, B-100:1 In:Cd) added to a solution of purified Cd_3P_2 MSCs at room temperature then heated to 100 °C. Although other absorbance features appeared during the reaction, there was no formation of InP MSCs.

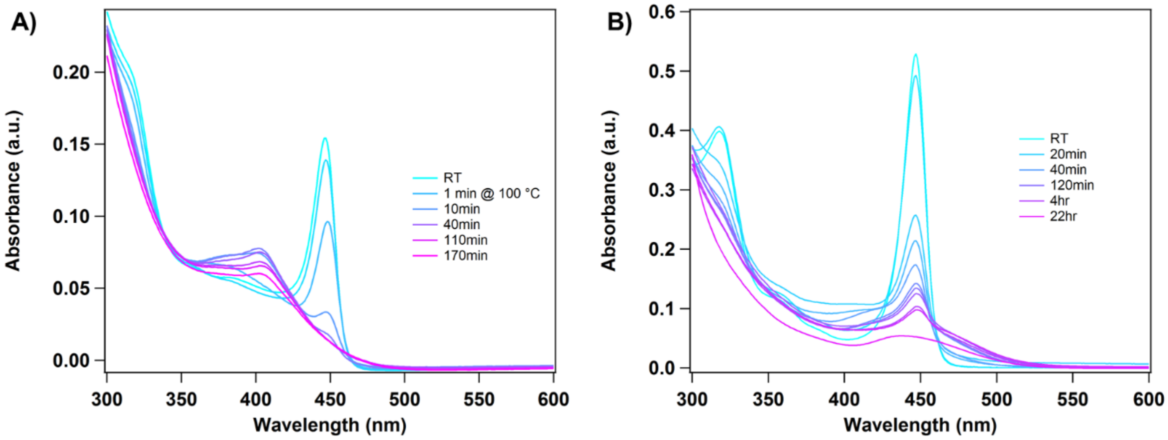

Figure 4.20. UV-Vis spectra of InP MSCs and Cd_3P_2 clusters mixed at room temperature in an approximate 1:1 Cd:In (A) and 10:1 Cd:In molar ratio (B) then heated to 100 °C. The peak broadness of the final product indicates there is a mixture of undetermined cluster species present.

4.3 Conclusions

From the combined data, we suggest the conversion of InP MSCs into Cd_3P_2 MSCs proceeds according to the mechanism depicted in Scheme 1. Up to 16 surface indium cations are progressively and stoichiometrically replaced by cadmium cations with a requisite lowering in the total ligand density at the cluster surface that is not accompanied by significant structural changes (phase 1). Beyond this point, a large excess of cadmium in solution is required to push progressive exchange with core indium and that this exchange is accompanied by a structural relaxation to the zinc blende structure (phase 2). During titration with Cd^{2+}, we observe that the structural rearrangement to a tetragonal lattice occurs in an abrupt, and potentially irreversible step, with subsequent cation exchange being rapid, leading to the diagnostic optical signatures of the Cd_3P_2 MSC (phase 3). These identifiable steps can be bypassed through the addition of a considerable excess of cadmium to the InP MSCs, which prevents the formation of intermediate kinetic products and progresses directly to Cd_3P_2.

With respect to previous work on III-V cation exchange in which the reverse reaction of Cd_3P_2 quantum dots to give InP was designated irreversible,[14] we consider the differences in quantum dot and cluster structure to be significant. The strain inherent in the InP MSC lattice likely leads to significant differences in its relative reactivity with Cd^{2+} versus a crystalline zinc blende QD. However, the general principle that stoichiometric Z-type exchange with ligand reorganization precedes thermodynamically-driven cation exchange is likely to be conserved in these systems.

4.4 Experimental

4.4.1 *General Considerations*

All glassware was dried in a 160 °C oven overnight prior to use. All reactions, unless otherwise noted were run under an inert atmosphere of nitrogen using a glovebox or using standard Schlenk techniques. *Warning: dimethyl cadmium is a volatile and extremely toxic reactant and was handled with care within a nitrogen glovebox. Both dimethyl cadmium and $P(SiMe_3)_3$ are pyrophoric, extremely reactive, and should be handled with caution.* Indium acetate (99.99%), anhydrous oleic acid (≥99%), phenylacetic acid (99%), and *trans*-2-[3-(4-tert-Butylphenyl)-2-methyl-2-propenylidene]malononitrile (DCTB) (≥99.0%) were purchased from Sigma-Aldrich Chemical Co. and used without further purification. Dimethyl cadmium (97%) was purchased from Strem chemicals and stored in a nitrogen glovebox. Bio-Beads S-X1 were purchased from Bio-Rad Laboratories. Omni Trace nitric acid was purchased from EMD Millipore and used without further purification. 18.2 MΩ was collected from an EMD Millipore water purification system. All solvents, including toluene, pentane, ethyl acetate, and acetonitrile were purchased from Sigma-Aldrich Chemical Co., dried over CaH_2, distilled, and stored over 4 Å molecular sieves in a nitrogen-filled glove box. C_6D_6 was purchased from Cambridge Isotope Labs and was similarly dried and stored. $P(SiMe_3)_3$ was prepared following literature procedures.[51]

^{31}P NMR spectra were collected on a 700 MHz Bruker Avance spectrometer. UV-Vis spectra were collected on a Cary 5000 spectrophotometer from Agilent or in-situ with an Ocean Optics TI300-Series absorbance dip probe. Data collected from the dip probe were smoothed in Igor Pro with binomial smoothing algorithms. Fluorescence and quantum yield measurements were taken on a Horiba Jobin Yvon FluoroMax-4 fluorescence spectrophotometer with the QuantaPhi integrating sphere accessory. ICP-OES was performed using a Perkin Elmer Optima 8300. TEM images were collected on an FEI Tecnai G2 F20 microscope using an ultrathin carbon film on holey carbon purchased from Ted Pella Inc.

4.4.2 *Synthesis of InP MSCs*

InP MSCs were synthesized following a modified preparation from Gary *et al.*.[37] Briefly, indium acetate (934 mg, 3.2 mmol) and phenylacetic acid (1.58 g, 11.6. mmol) were heated at 100 °C overnight under reduced pressure. Dry toluene (10 mL) was added to the reaction flask at room temperature the following day. $P(SiMe_3)_3$ (465 μL, 1.6 mmol) was measured into 5 mL of toluene and injected into the indium phenylacetate at 110 °C. Cluster growth was typically complete within 20-40 minutes. Purification of the particles was achieved through successive precipitation/re-dissolution cycles using toluene and pentane as the solvent and non-solvent, respectively.

4.4.3 *Cadmium Phenylacetate Synthesis:*

Dimethyl cadmium (559 μL, 7.8 mmol) was added dropwise to a chilled solution of phenylacetic acid (2.12 g, 15.6 mmol) in a 4:1 pentane/toluene mixture. After 3 hours of stirring, volatile solvents were removed under vacuum and the product was washed 3 more times with pentane. The same procedure was used to synthesize cadmium oleate with oleic acid in place of phenylacetic acid and product washes were performed with ethyl acetate instead of pentane.

4.4.4 *Cd^{2+} Titrations*

Stoichiometric amounts of cadmium oleate dissolved in toluene, or cadmium phenylacetate dissolved in acetonitrile, were added to solutions of InP stirring at room temperature. Solutions were monitored by UV-Vis until changes were no longer observed (typically 12-24 hours). The solutions were purified by gel permeation chromatography; preparation of the column in the glovebox was performed following a literature procedure.[52] Purified samples were characterized by ICP, PDF, XRD, TEM, XPS, and MALDI-TOF.

4.4.5 *Cd_3P_2 MSC via Molecular Precursors*

Cadmium phosphide MSCs were synthesized using a modified literature procedure.[32] Cadmium oleate (0.135 g, 0.2 mmol) was dissolved in 10 mL dry toluene in a reaction flask under nitrogen. $P(SiMe_3)_3$ (15 µL, 0.05 mmol) was measured into 2 mL of toluene and injected into the flask at room temperature. Cluster growth was monitored by UV-Vis until no further changes occurred. Purification was achieved through successive precipitation/re-dissolution cycles using toluene and ethanol as the solvent and non-solvent, respectively. Particle growth was observed with excess purification, further relevant details are discussed in the SI (Figure S11).

4.4.6 *MALDI-TOF*

Mass spectra were collected on a Bruker Autoflex II instrument using DCTB as the matrix. Cluster samples dispersed in toluene were mixed with toluene solutions of the matrix and spotted on a stainless-steel plate in a glovebox. Desorption and ionization of samples was achieved by irradiation with a pulsed nitrogen laser. Mass spectra were measured with the detector in linear positive mode with a laser intensity between 5-15%. Calibration was performed using external standards ubiquitin I, myoglobin and cytochrome C. Data was smoothed and fitted in Igor Pro using binomial smoothing algorithms.

4.4.7 *XPS Acquisition*

All XPS spectra were taken on a Surface Science Instruments S-Probe photoelectron spectrometer. This instrument has a monochromatized Al Kα X-ray source which was operated at 20 mA and 10 kV, and a low energy electron flood gun for charge neutralization. The samples were drop-cast solutions on a Si wafer while the indium acetate was brushed onto two-sided tape mounted on a Si wafer. X-ray analysis area for these acquisitions was approximately 800 μm across. Pressure in the analytical chamber during spectral acquisition was less than 5×10^{-9} torr. All included figures are high resolution spectra. Pass energy for high resolution spectra was 50 eV and data point spacing was 0.065 eV/step. The take-off angle (the angle between the sample normal and the input axis of the energy analyzer) was 0° (~100 Å sampling depth). Service Physics Hawk version 7 data analysis software was used to peak fit high resolution spectra.

4.4.8 *Computational Methods*

Computational studies were performed using the *Gaussian* electronic structure package.[53] The HSE06 range-separated hybrid DFT functional was used to perform both the linear-response TDDFT absorption spectra and geometry optimizations.[54–56] This method is appropriate for describing charge-transfer excitations and has been previously shown to correctly compute the InP quantum dot electronic structure.[30,31,57] TDDFT was used to compute both the excitation energies and corresponding oscillator strengths of the first 10 electronic transitions.[58–60] The LANL2DZ basis set is used, in which core electrons are replaced by an effective core potential, and only O

(1s, 2s, 2p), C (1s, 2s, 2p), In (5s, 5p), Cd (4d, 5s, 5p) and P (3s, 3p) atomic orbitals are described with explicit basis functions.[61–64]

All calculations were performed on structures where the phenyl moieties were replaced by acetate, $In_{37}P_{20}(O_2CCH_3)_{51}$, $Cd_2In_{35}P_{20}(O_2CCH_3)_{49}$, and $Cd_{16}In_{21}P_{20}(O_2CCH_3)_{35}(HO_2CCH_3)_2$, to investigate the effect of the presence of cadmium atoms on the UV-Vis spectrum, the electronic properties and structural rearrangement. Starting from the optimized $In_{37}P_{20}(O_2CCH_3)_{51}$ structure, the Cd-containing models were prepared, and further optimized, by replacing two In atoms with two Cd atoms and removing two carboxylate ligands, the closest to the substituted atoms, to preserve the charge compensation, $Cd_2In_{35}P_{20}(O_2CCH_3)_{49}$. The substitution strategy mostly retained the overall molecular symmetry, therefore in the resulting models two In atoms, either located on top of the pseudo C_2 symmetry axis (namely axial) of the molecule or in the plane (namely equatorial) orthogonal to it, were substituted by two Cd atoms, respectively. For the 16 Cd-containing structure, starting from the optimized $In_{37}P_{20}(O_2CCH_3)_{51}$ structure, 14 negative charged ligands were removed and another two were protonated (located at the opposite sides of the molecule equatorial plane) to preserve both the charge compensation and simultaneously preserve full cadmium coordination and the overall cluster symmetry.

4.4.9 *PDF Analysis*

X-ray total scattering experiments were conducted on beamline 28-ID-2 at the National Synchrotron Light Source II (NSLS-II) at Brookhaven National Laboratory. An X-ray beam of energy 67.563 keV ($\lambda = 0.18351$ Å) was focused on samples loaded into Kapton capillaries cooled to 100 K using a liquid nitrogen cryostream. Scattered intensities were collected in rapid acquisition mode[65] on a Perkin-Elmer 2D flat panel detector (2048 × 2048 pixels and 200 × 200 μm pixel size) mounted orthogonal to the beam path at a distance of 205.4850 mm from the sample.

Final Cd_3P_2 products were measured on a separate date using a similar setup. A Ni standard sample was measured to calibrate the detector geometry, and 2D intensities were azimuthally integrated to 1D intensity versus the magnitude of the scattering vector Q using Fit2D.[66] Scattering from an empty Kapton tube was measured and subtracted as a background.

The PDF gives the scaled probability of finding atom-pairs in the material at a distance *r* apart. The program xPDFsuite with PDFGetX3[66,67] was used to convert the diffracted intensities to the real-space pair distribution function (PDF), G(r), by

$$G(r) = \frac{2}{\pi}\int_{Q_{min}}^{Q_{max}} F\,(Q) sin(Qr) dQ$$

where *F(Q)* is the total scattering structure function which is generated after normalization and reduction of the coherent scattering intensities, and Q_{min} and Q_{max} are the minimum and maximum values of the scattering momentum transfer considered.

Structure refinements were carried out using the Diffpy-CMI complex modeling framework.[67] The starting model for InP clusters was obtained from Gary *et al.* from which ligand atoms were removed except for oxygen.[30] Model PDFs were generated as in Jensen *et al.*,[68] by first simulating the structure function from the Debye scattering equation,

$$F(Q) = \frac{1}{N\langle f(Q)\rangle^2}\sum\nolimits_{i,j\neq i} f_i\,(Q) f_j(Q)\frac{sin(Qr_{ij})}{r_{ij}},$$

which was then Fourier transformed over a range of 0.85-23.1 $Å^{-1}$, and subsequently refined using isotropic thermal parameters U_{iso} for each atomic species, a scale factor, an expansion coefficient, an *r*-dependent peak sharpening coefficient δ_2 to account for correlated motion.

4.5 References

(1) Eilers, J.; Groeneveld, E.; de Mello Donegá, C.; Meijerink, A. Optical Properties of Mn-Doped ZnTe Magic Size Nanocrystals. *J. Phys. Chem. Lett.* **2012**, *3* (12), 1663–1667.

(2) Mocatta, D.; Cohen, G.; Schattner, J.; Millo, O.; Rabani, E.; Banin, U. Heavily Doped Semiconductor Nanocrystal Quantum Dots. *Science* **2011**, *332* (6025), 77–81.

(3) Sytnyk, M.; Kirchschlager, R.; Bodnarchuk, M. I.; Primetzhofer, D.; Kriegner, D.; Enser, H.; Stangl, J.; Bauer, P.; Voith, M.; Hassel, A. W.; et al. Tuning the Magnetic Properties of Metal Oxide Nanocrystal Heterostructures by Cation Exchange. *Nano Lett.* **2013**, *13* (2), 586–593.

(4) Yang, J.; Muckel, F.; Baek, W.; Fainblat, R.; Chang, H.; Bacher, G.; Hyeon, T. Chemical Synthesis, Doping, and Transformation of Magic-Sized Semiconductor Alloy Nanoclusters. *J. Am. Chem. Soc.* **2017**, *139* (19), 6761–6770.

(5) Son, D. H.; Hughes, S. M.; Yin, Y.; Paul Alivisatos, A. Cation Exchange Reactions in Ionic Nanocrystals. *Science* **2004**, *306* (5698), 1009–1012.

(6) Enright, M. J.; Sarsito, H.; Cossairt, B. M. Quantifying Cation Exchange of Cd2+ in ZnTe: A Challenge for Accessing Type II Heterostructures. *Chem. Mater.* **2017**, *29* (2), 666–672.

(7) Casavola, M.; van Huis, M. A.; Bals, S.; Lambert, K.; Hens, Z.; Vanmaekelbergh, D. Anisotropic Cation Exchange in PbSe/CdSe Core/Shell Nanocrystals of Different Geometry. *Chem. Mater.* **2012**, *24* (2), 294–302.

(8) Mu, L.; Wang, F.; Sadtler, B.; Loomis, R. A.; Buhro, W. E. Influence of the Nanoscale Kirkendall Effect on the Morphology of Copper Indium Disulfide Nanoplatelets Synthesized by Ion Exchange. *ACS Nano* **2015**, *9* (7), 7419–7428.

(9) Smith, A. M.; Nie, S. Bright and Compact Alloyed Quantum Dots with Broadly Tunable Near-Infrared Absorption and Fluorescence Spectra through Mercury Cation Exchange. *J. Am. Chem. Soc.* **2011**, *133* (1), 24–26.

(10) Groeneveld, E.; Witteman, L.; Lefferts, M.; Ke, X.; Bals, S.; Van Tendeloo, G.; de Mello Donega, C. Tailoring ZnSe–CdSe Colloidal Quantum Dots via Cation Exchange: From Core/Shell to Alloy Nanocrystals. *ACS Nano* **2013**, *7* (9), 7913–7930.

(11) Kim, S.; Kim, T.; Kang, M.; Kwak, S. K.; Yoo, T. W.; Park, L. S.; Yang, I.; Hwang, S.; Lee, J. E.; Kim, S. K.; et al. Highly Luminescent InP/GaP/ZnS Nanocrystals and Their Application to White Light-Emitting Diodes. *J. Am. Chem. Soc.* **2012**, *134* (8), 3804–3809.

(12) van der Stam, W.; Bladt, E.; Rabouw, F. T.; Bals, S.; de Mello Donega, C. Near-Infrared Emitting CuInSe2/CuInS2 Dot Core/Rod Shell Heteronanorods by Sequential Cation Exchange. *ACS Nano* **2015**, *9* (11), 11430–11438.

(13) Zhang, J.; Chernomordik, B. D.; Crisp, R. W.; Kroupa, D. M.; Luther, J. M.; Miller, E. M.; Gao, J.; Beard, M. C. Preparation of Cd/Pb Chalcogenide Heterostructured Janus Particles via Controllable Cation Exchange. *ACS Nano* **2015**, *9* (7), 7151–7163.

(14) Beberwyck, B. J.; Alivisatos, A. P. Ion Exchange Synthesis of III–V Nanocrystals. *J. Am. Chem. Soc.* **2012**, *134* (49), 19977–19980.

(15) De Trizio, L.; Manna, L. Forging Colloidal Nanostructures via Cation Exchange Reactions. *Chem. Rev.* **2016**, *116* (18), 10852–10887.

(16) Rivest, J. B.; Jain, P. K. Cation Exchange on the Nanoscale: An Emerging Technique for New Material Synthesis, Device Fabrication, and Chemical Sensing. *Chem. Soc. Rev.* **2013**, *42* (1), 89–96.

(17) Gupta, S.; Kershaw, S. V.; Rogach, A. L. 25th Anniversary Article: Ion Exchange in Colloidal Nanocrystals. *Adv. Mater.* **2013**, *25* (48), 6923–6944.

(18) Beberwyck, B. J.; Surendranath, Y.; Alivisatos, A. P. Cation Exchange: A Versatile Tool for Nanomaterials Synthesis. *J. Phys. Chem. C* **2013**, *117* (39), 19759–19770.

(19) Backhaus-Ricoult, M. Solid-State Reactivity at Heterophase Interfaces. *Annu. Rev. Mater. Res.* **2003**, *33* (1), 55–90.

(20) Wark, S. E.; Hsia, C.-H.; Son, D. H. Effects of Ion Solvation and Volume Change of Reaction on the Equilibrium and Morphology in Cation-Exchange Reaction of Nanocrystals. *J. Am. Chem. Soc.* **2008**, *130* (29), 9550–9555.

(21) Ott, F. D.; Spiegel, L. L.; Norris, D. J.; Erwin, S. C. Microscopic Theory of Cation Exchange in CdSe Nanocrystals. *Phys. Rev. Lett.* **2014**, *113* (15), 156803.

(22) Zheng, Z.; Sun, Y.-Y.; Xie, W.; Zhao, J.; Zhang, S. Solvent-Based Atomistic Theory for Doping Colloidal-Synthesized Quantum Dots via Cation Exchange. *J. Phys. Chem. C* **2016**, *120* (47), 27085–27090.

(23) Bothe, C.; Kornowski, A.; Tornatzky, H.; Schmidtke, C.; Lange, H.; Maultzsch, J.; Weller, H. Solid-State Chemistry on the Nanoscale: Ion Transport through Interstitial Sites or Vacancies? *Angew. Chem. Int. Ed.* **2015**, *54* (47), 14183–14186.

(24) Friedfeld, M. R.; Stein, J. L.; Cossairt, B. M. Main-Group-Semiconductor Cluster Molecules as Synthetic Intermediates to Nanostructures. *Inorg. Chem.* **2017**.

(25) White, S. L.; Banerjee, P.; Chakraborty, I.; Jain, P. K. Ion Exchange Transformation of Magic-Sized Clusters. *Chem. Mater.* **2016**, *28* (22), 8391–8398.

(26) White, S. L.; Smith, J. G.; Behl, M.; Jain, P. K. Co-Operativity in a Nanocrystalline Solid-State Transition. *Nat Commun* **2013**, *4*, 1–8.

(27) van der Stam, W.; Geuchies, J. J.; Altantzis, T.; van den Bos, K. H. W.; Meeldijk, J. D.; Van Aert, S.; Bals, S.; Vanmaekelbergh, D.; de Mello Donega, C. Highly Emissive Divalent-Ion-Doped Colloidal CsPb1–XMxBr3 Perovskite Nanocrystals through Cation Exchange. *J. Am. Chem. Soc.* **2017**, *139*, 4087–4097.

(28) Dong, C.; van Veggel, F. C. J. M. Cation Exchange in Lanthanide Fluoride Nanoparticles. *ACS Nano* **2009**, *3* (1), 123–130.

(29) De Trizio, L.; Gaspari, R.; Bertoni, G.; Kriegel, I.; Moretti, L.; Scotognella, F.; Maserati, L.; Zhang, Y.; Messina, G. C.; Prato, M.; et al. Cu3-XP Nanocrystals as a Material Platform for Near-Infrared Plasmonics and Cation Exchange Reactions. *Chem. Mater.* **2015**, *27* (3), 1120–1128.

(30) Gary, D. C.; Flowers, S. E.; Kaminsky, W.; Petrone, A.; Li, X.; Cossairt, B. M. Single-Crystal and Electronic Structure of a 1.3 Nm Indium Phosphide Nanocluster. *J. Am. Chem. Soc.* **2016**, *138* (5), 1510–1513.

(31) Gary, D. C.; Petrone, A.; Li, X.; Cossairt, B. M. Investigating the Role of Amine in InP Nanocrystal Synthesis: Destabilizing Cluster Intermediates by Z-Type Ligand Displacement. *Chem. Commun.* **2016**, *53* (1), 161–164.

(32) Wang, R.; Ratcliffe, C. I.; Wu, X.; Voznyy, O.; Tao, Y.; Yu, K. Magic-Sized Cd3P2 II−V Nanoparticles Exhibiting Bandgap Photoemission. *J. Phys. Chem. C* **2009**, *113* (42), 17979–17982.

(33) Adolphi, N. L.; Stoddard, R. D.; Goel, S. C.; Buhro, W. E.; Gibbons, P. C.; Conradi, M. S. The 31P NMR Spectra of Cd3P2 and Zn3P2. *J. Phys. Chem. Solids* **1992**, *53* (10), 1275–1278.

(34) Anderson, N. C.; Hendricks, M. P.; Choi, J. J.; Owen, J. S. Ligand Exchange and the Stoichiometry of Metal Chalcogenide Nanocrystals: Spectroscopic Observation of Facile Metal-Carboxylate Displacement and Binding. *J. Am. Chem. Soc.* **2013**, *135* (49), 18536–18548.

(35) Lawrence, K. N.; Dutta, P.; Nagaraju, M.; Teunis, M. B.; Muhoberac, B. B.; Sardar, R. Dual Role of Electron-Accepting Metal-Carboxylate Ligands: Reversible Expansion of Exciton Delocalization and Passivation of Nonradiative Trap-States in Molecule-like CdSe Nanocrystals. *J. Am. Chem. Soc.* **2016**, *138* (39), 12813–12825.

(36) Xie, L.; Shen, Y.; Franke, D.; Sebastián, V.; Bawendi, M. G.; Jensen, K. F. Characterization of Indium Phosphide Quantum Dot Growth Intermediates Using MALDI-TOF Mass Spectrometry. *J. Am. Chem. Soc.* **2016**, *138* (41), 13469–13472.

(37) Gary, D. C.; Terban, M. W.; Billinge, S. J. L.; Cossairt, B. M. Two-Step Nucleation and Growth of InP Quantum Dots via Magic-Sized Cluster Intermediates. *Chem. Mater.* **2015**, *27* (4), 1432–1441.

(38) Beecher, A. N.; Yang, X.; Palmer, J. H.; LaGrassa, A. L.; Juhas, P.; Billinge, S. J. L.; Owen, J. S. Atomic Structures and Gram Scale Synthesis of Three Tetrahedral Quantum Dots. *J. Am. Chem. Soc.* **2014**, *136* (30), 10645–10653.

(39) Stein, J. L.; Mader, E. A.; Cossairt, B. M. Luminescent InP Quantum Dots with Tunable Emission by Post-Synthetic Modification with Lewis Acids. *J. Phys. Chem. Lett.* **2016**, *7* (7), 1315–1320.

(40) Frederick, M. T.; Achtyl, J. L.; Knowles, K. E.; Weiss, E. A.; Geiger, F. M. Surface-Amplified Ligand Disorder in CdSe Quantum Dots Determined by Electron and Coherent Vibrational Spectroscopies. *J. Am. Chem. Soc.* **2011**, *133* (19), 7476–7481.

(41) Xie, R.; Zhang, J.; Zhao, F.; Yang, W.; Peng, X. Synthesis of Monodisperse, Highly Emissive, and Size-Tunable Cd3P2 Nanocrystals. *Chem. Mater.* **2010**, *22* (13), 3820–3822.

(42) Glassy, B. A.; Cossairt, B. M. Ternary Synthesis of Colloidal Zn3P2 Quantum Dots. *Chem. Commun.* **2015**, *51*, 5283–5286.

(43) Glassy, B. A.; Cossairt, B. M. Resolving the Chemistry of Zn3P2 Nanocrystal Growth. *Chem. Mater.* **2016**, *28* (17), 6374–6380.

(44) Harrell, S. M.; McBride, J. R.; Rosenthal, S. J. Synthesis of Ultrasmall and Magic-Sized CdSe Nanocrystals. *Chem. Mater.* **2013**, *25* (8), 1199–1210.

(45) Virieux, H.; Le Troedec, M.; Cros-Gagneux, A.; Ojo, W.-S.; Delpech, F.; Nayral, C.; Martinez, H.; Chaudret, B. InP/ZnS Nanocrystals: Coupling NMR and XPS for Fine Surface and Interface Description. *J. Am. Chem. Soc.* **2012**, *134* (48), 19701–19708.

(46) Borchert, H.; Haubold, S.; Haase, M.; Weller, H.; McGinley, C.; Riedler, M.; Möller, T. Investigation of ZnS Passivated InP Nanocrystals by XPS. *Nano Lett.* **2002**, *2* (2), 151–154.

(47) Huang, K.; Demadrille, R.; Silly, M. G.; Sirotti, F.; Reiss, P.; Renault, O. Internal Structure of InP/ZnS Nanocrystals Unraveled by High-Resolution Soft X-Ray Photoelectron Spectroscopy. *ACS Nano* **2010**, *4* (8), 4799–4805.

(48) Nanda, J.; Kuruvilla, B. A.; Sarma, D. D. Photoelectron Spectroscopic Study of CdS Nanocrystallites. *Phys. Rev. B* **1999**, *59* (11), 7473–7479.

(49) Sowers, K. L.; Hou, Z.; Peterson, J. J.; Swartz, B.; Pal, S.; Prezhdo, O.; Krauss, T. D. Photophysical Properties of CdSe/CdS Core/Shell Quantum Dots with Tunable Surface Composition. *Chem. Phys.* **2016**, *471*, 24–31.

(50) Subila, K. B.; Kishore Kumar, G.; Shivaprasad, S. M.; George Thomas, K. Luminescence Properties of CdSe Quantum Dots: Role of Crystal Structure and Surface Composition. *J. Phys. Chem. Lett.* **2013**, *4* (16), 2774–2779.

(51) Gary, D. C.; Cossairt, B. M. Role of Acid in Precursor Conversion During InP Quantum Dot Synthesis. *Chem. Mater.* **2013**, *25* (12), 2463–2469.

(52) Shen, Y.; Roberge, A.; Tan, R.; Gee, M. Y.; Gary, D. C.; Huang, Y.; Blom, D. A.; Benicewicz, B. C.; Cossairt, B. M.; Greytak, A. B. Gel Permeation Chromatography as a Multifunctional Processor for Nanocrystal Purification and On-Column Ligand Exchange Chemistry. *Chem. Sci.* **2016**, *7* (9), 5671–5679.

(53) Frisch, M. J.; Trucks, G. W.; Schlegel, H. B.; Scuseria, G. E.; Robb, M. A.; Cheeseman, J. R.; Scalmani, G.; Barone, V.; Mennucci, B.; Petersson, G. A.; et al. *Gaussian 09*; Wallingford, CT, USA, 2009.

(54) Heyd, J.; Scuseria, G. E. Hybrid Functionals Based on a Screened Coulomb Potential. *J. Chem. Phys.* **2003**, *118* (18), 8207–8215.

(55) Heyd, J.; Scuseria, G. E. Efficient Hybrid Density Functional Calculations in Solids: Assessment of the Heyd–Scuseria–Ernzerhof Screened Coulomb Hybrid Functional. *J. Chem. Phys.* **2004**, *121* (3), 1187–1192.

(56) Vydrov, O. A.; Heyd, J.; Krukau, A. V.; Scuseria, G. E. Importance of Short-Range versus Long-Range Hartree-Fock Exchange for the Performance of Hybrid Density Functionals. *J. Chem. Phys.* **2006**, *125* (7), 074106.

(57) Cho, E.; Jang, H.; Lee, J.; Jang, E. Modeling on the Size Dependent Properties of InP Quantum Dots: A Hybrid Functional Study. *Nanotechnology* **2013**, *24* (21), 215201.

(58) Casida, M. E.; Jamorski, C.; Casida, K. C.; Salahub, D. R. Molecular Excitation Energies to High-Lying Bound States from Time-Dependent Density-Functional Response Theory: Characterization and Correction of the Time-Dependent Local Density Approximation Ionization Threshold. *J. Chem. Phys.* **1998**, *108* (11), 4439–4449.

(59) Furche, F.; Ahlrichs, R. Adiabatic Time-Dependent Density Functional Methods for Excited State Properties. *J. Chem. Phys.* **2002**, *117* (16), 7433–7447.

(60) Stratmann, R. E.; Scuseria, G. E.; Frisch, M. J. An Efficient Implementation of Time-Dependent Density-Functional Theory for the Calculation of Excitation Energies of Large Molecules. *J. Chem. Phys.* **1998**, *109* (19), 8218–8224.

(61) Schaefer, H. F. *Methods of Electronic Structure Theory*, 1st ed.; Vol. 3.

(62) Hay, P. J.; Wadt, W. R. Ab Initio Effective Core Potentials for Molecular Calculations. Potentials for the Transition Metal Atoms Sc to Hg. *J. Chem. Phys.* **1985**, *82* (1), 270–283.

(63) Hay, P. J.; Wadt, W. R. Ab Initio Effective Core Potentials for Molecular Calculations. Potentials for K to Au Including the Outermost Core Orbitals. *J. Chem. Phys.* **1985**, *82* (1), 299–310.

(64) Wadt, W. R.; Hay, P. J. Ab Initio Effective Core Potentials for Molecular Calculations. Potentials for Main Group Elements Na to Bi. *J. Chem. Phys.* **1985**, *82* (1), 284–298.

(65) Chupas, P. J.; Xiangyun Qiu, P. J.; Hanson, J. C.; Lee, P. L.; Grey, C. P.; Billinge, S. J. L. Rapid-Acquisition Pair Distribution Function (RA-PDF) Analysis. *J. Appl. Crystallogr.* **2003**, *36* (6), 1342–1347.

(66) Hammersley, A. P.; Svensson, S. O.; Hanfland, M.; Fitch, A. N.; Hausermann, D. Two-Dimensional Detector Software: From Real Detector to Idealised Image or Two-Theta Scan. *High Press. Res.* **1996**, *14*, 235–248.

(67) Juhás, P.; Farrow, C.; Yang, X.; Knox, K.; Billinge, S. Complex Modeling: A Strategy and Software Program for Combining Multiple Information Sources to Solve Ill Posed Structure and Nanostructure Inverse Problems. *Acta Crystallogr. Sect. Found. Adv.* **2015**, *71* (6), 562–568.

(68) Jensen, K. M. Ø.; Juhas, P.; Tofanelli, M. A.; Heinecke, C. L.; Vaughan, G.; Ackerson, C. J.; Billinge, S. J. L. Polymorphism in Magic-Sized Au144(SR)60 Clusters. *Nat. Commun.* **2016**, *7*, 11859.

Chapter 5. Dual Role of InP Magic-Sized Clusters: Cation Exchange Platform and Single-Source Precursor

5.1 Note for Collaborative Work

This work was supported in part by a sponsored project agreement with Merck KGaA. All content in the following chapter is confidential and subject to the terms of the agreement.

5.2 Introduction

Magic-sized clusters (MSCs) have proven to be useful models for assessing the mechanistic pathway and structural impacts of chemical reactions that occur in larger semiconductor nanoparticles due to the perfect monodispersity and well-defined stoichiometry of MSCs.[1–3] Our work with cadmium cation exchange demonstrated that the InP MSC undergoes facile cation exchange and structural rearrangement with full conversion to Cd_3P_2. Using this model, we investigated the analogous reaction with zinc, noting the differences in polarizability, ionic radius, and charge of these cations. Whereas Cd^{2+} is a softer acid than In^{3+}, with a chemical hardness η of 10.29, Zn^{2+} (10.88) lies closer to In^{3+} (13) as an intermediately hard acid.[4] In addition to this less favorable replacement in a soft P anionic lattice, the single bond covalent radius difference between In (142 pm) and Zn (122 pm) may induce structural contraction.[5] While the fundamental importance of examining a unique model for cation exchange in a covalent III-V lattice interests us, this work is strongly motivated by the commercial aspect of developing new methods to access and integrate shelled zinc alloyed InP QDs as phosphors for display technologies.

Presently, the majority of modern InP QD syntheses contain zinc as a secondary metal precursor in the nucleation solution.[6] The mechanistic role of zinc remains generally unclear, but it has been observed to improve size distributions and quantum yields of as-synthesized particles.[7–11] The cause of photoluminescence (PL) enhancement, as suggested in our work with post-synthetic zinc treatment, is derived from surface phosphorus passivation.[12] Recent reports that have implicated zinc as an active agent in forming a Zn-P complex, previously used for Zn_3P_2 syntheses, which serves to inhibit the rapid reactivity of $P(SiMe_3)_3$ and indium precursors.[9] The Zn-P complex is suggested to be more stable at higher temperatures than the In-P complex, thus at a critical temperature, a more uniform burst of nucleation occurs resulting in more desirable size distributions compared to syntheses without zinc additives. Naturally, the question remains whether zinc is incorporated homogeneously into the InP lattice or is driven to the surface through InP self-purification. Houtepen and co-workers interrogated this system with an emphasis on the structural manifestation of zinc additives and reported that zinc alloys into the InP QD lattice, discernable by the lattice contractions seen by powder X-ray diffraction (pXRD).[10] Furthermore, emissive properties of InP core-shell nanostructures can be optimized by reducing interfacial strain through composition tuning and consequential adjustment of the InP lattice parameter.[10,13]

We hypothesized that the InP cluster would serve as a viable platform for zinc cation exchange and the resulting compounds would be intriguing precursors for InP QDs that would be more susceptible to epitaxial-like shell growth of ZnE (E=S, Se). Selecting an appropriate zinc source for these reactions was paramount. Unlike the immediate reaction we observed between cadmium carboxylate and InP MSCs, zinc carboxylates could be considered fairly inert with additional complications arising from solubility in compatible solvents. We investigated three viable zinc precursors with a range of reactivities: zinc myristate [$Zn(MA)_2$], a pentanuclear zinc cluster [$Zn_5(O_2CH_3)_6(Et)_4$] denoted Zn5 cluster, and diethyl zinc ($ZnEt_2$). The predicted range of reactivity is based on previous NMR studies performed between these precursors and $P(SiMe_3)_3$

in the synthesis of Zn_3P_2 QDs.[14,15] Our initial experiments evaluated the reactivity of these species with InP MSCs by tracking the UV-Vis absorption and analyzing the structural composition of the resulting products with pXRD and ^{31}P NMR spectroscopy. From this series of zinc precursors, varying the concentration and reaction temperature led us to assess that the Zn5 cluster, added to the InP MSC at room temperature, resulted in the most robust and isolable products. Proceeding forward, cation exchange reactions were performed by titrating a solution of Zn5 cluster into InP MSCs and stirring at room temperature until the reaction was gauged complete by ^{31}P NMR after 3 days. We characterized the modified electronic and physical properties of alloyed clusters using UV-Vis/NMR spectroscopy and MALDI-TOF/XRD/ICP.

5.3 Results and Discussion

5.3.1 *InP Clusters as a Scaffold for Zinc Cation Exchange*

The optical transitions of the $In_{37}P_{20}$ MSC can be diagnostic of reactions taking place at the surface, including with amines, water, and cadmium carboxylates.[2,16,17] We find that the room temperature titration of Zn5 leads to negligible shifts of the absorbance maximum up to 37 equivalents of Zn^{2+} relative to the MSC, shown in Figure 5.1. Above 37 equivalents, the cluster peak starts to blue-shift and broaden, which we assign as the gradual dissolution of InP through zinc incorporation into the core that leads to cluster destabilization. In prior work, the surface interaction of exogeneous ligands or Lewis acids strongly impacted the electronic transitions (HOMO-1 to LUMO and HOMO to LUMO) responsible for the lowest energy absorption feature given that much of the electronic density of these orbitals is localized near the surface. The following data and characterization support our hypothesis that zinc does indeed exchange with indium on the surface of the cluster, thus one possibility for the unchanging absorbance feature is that the energetic overlap between zinc and the cluster is minimal or otherwise closely aligned with indium.

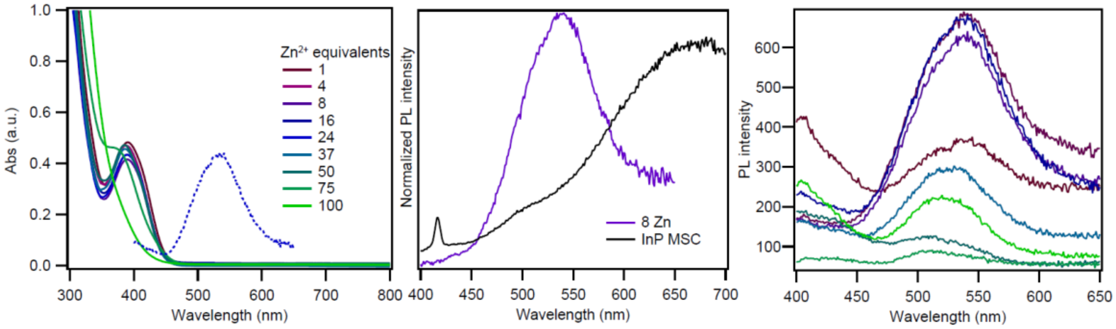

Figure 5.1. UV-Vis spectrum (left) and PL spectra of InP MSC with increasing zinc concentrations. The middle plot shows a normalized comparison of InP MSC PL and a zinc-treated InP PL while the right plot shows the emission of all zinc species corresponding to the colored traces in the absorbance spectrum.

While the absorbance maximum is persistent at 386 nm, the PL of the cluster tells a different story. At 298 K, the InP MSC consistently exhibits weak emission, shown in the middle panel of Figure 5.1, that is associated with structural distortions of the cluster upon excitation.[16] In larger as-synthesized InP quantum dots, the photoluminescence quantum yields (PL QYs) are <1% due to non-radiative pathways arising from under-coordinated or oxidized surface sites. As discussed previously, in the case of InP QDs, the replacement of zinc for indium and concurrent passivation of phosphorus improved the PL QYs, thus we might expect an analogous enhancement of InP MSC PL through the exchange of zinc for indium. The InP cluster presents a unique example lacking un-passivated surface atoms so it has been suggested energy loss occurs through non-radiative vibrational relaxation in the lattice.[16] After several days, all samples stirring with Zn5 cluster exhibited growth of a distinct broad emission feature centered at 526 nm (90 nm fwhm), shown in Figure 5.1. The weak intensity did not significantly change by increased relative zinc equivalents between 4-37, while at concentrations above 37 equiv., the PL decreased, corresponding to the diminishing absorbance feature and gradual dissolution of the cluster. We hypothesize that growth of this proposed PL band edge feature is related to the Z-type ligand exchange of zinc for indium exclusively between the 16 indium ions on the surface of the cluster, comparable to our observations with InP QDs. This effect is likely satisfied with the replacement of just a few surface indium ions while further zinc addition up to 37 equivalents suggests that the energy loss pathways still originate from the core lattice vibrations. The broadness of the emission feature is also related to the non-selective nature of cation exchange and what is likely an average population of clusters with similar but variable structures and compositions.

Discerning the structural impact of indium-to-zinc exchange is aided by ^{31}P NMR spectroscopy. The pseudo-C_2v-symmetric InP cluster has 11 unique phosphorus environments (two P atoms reside on the molecular C2 axis, and the remaining 18 P atoms are related by the C2 axis resulting in nine additional resonances), shown in Figure 5.2, which can be assigned to different sites based on their proximity to In-O neighbors and shielding arguments.[17] The addition of 4 eq. Zn slightly broadens the distinct resonances as expected with a difference in shielding tensors and this effect is observed with further equivalents of zinc due to the non-site selective nature of the exchange. Zinc phosphide nanocrystals have a phosphorus resonance at –200 ppm which would be consistent with the lack of significant shifts in this series of alloyed clusters.[15] In comparison, a progressive upfield shift was observed with cadmium cation exchange as the alloyed cluster took on increasing cadmium-phosphide character, where Cd_3P_2 clusters have a phosphorus resonance at –364 ppm.[2]

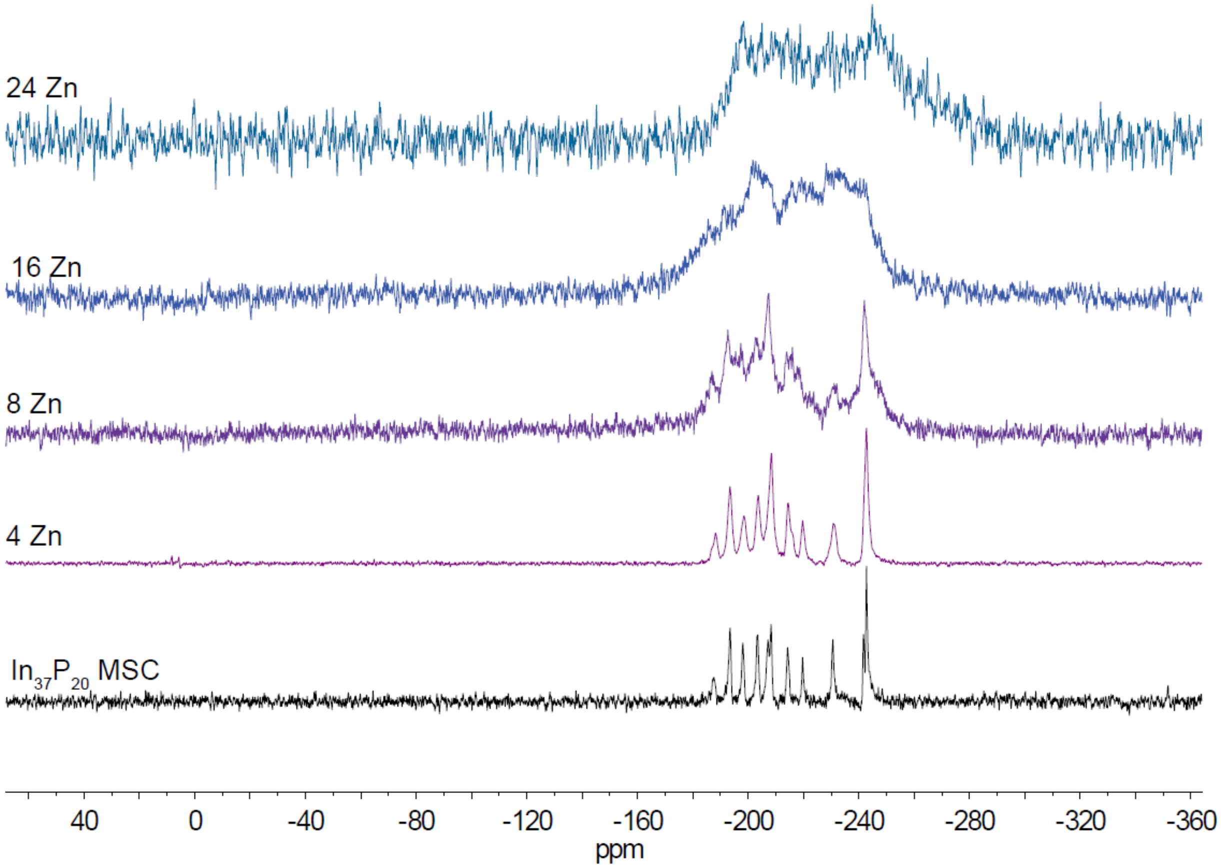

Figure 5.2. ^{31}P NMR (283.5 MHz, C_6D_6) spectra of clusters and increasing zinc equivalents taken at room temperature.

Mass spectrometry has proven to be a valuable technique for the identification of semiconductor nanoclusters and their alloyed derivatives.[3,18,19] Previously, the mass spectrum of phenylacetate-capped $In_{37}P_{20}$ MSCs obtained by our group using MALDI-TOF showed that the largest mass peak was centered at 8,500 m/z, indicating that a portion of the intact cluster (mass 11,759 g/mol) must be displaced during ionization.[2] Since then, we have characterized a series of carboxylate-ligated $In_{37}P_{20}$ MSCS to identify a consistent fragmentation pattern that can aid in the identification of alloyed intermediates. Shown in Figure 5.3 are the mass spectra of phenylacetate, oleate, and myristate-capped InP MSCs with the zoom inset highlighting the largest and most apparent mass peak. The masses of these fragments correspond closely to a parent fragment ion that retains an $[In_{21}P_{20}]^{3+}$ core, 10 surface-coordinated $In(O_2CR)_3$, and 2 $^{-}O_2CR$, with the respective carboxylate ligands.

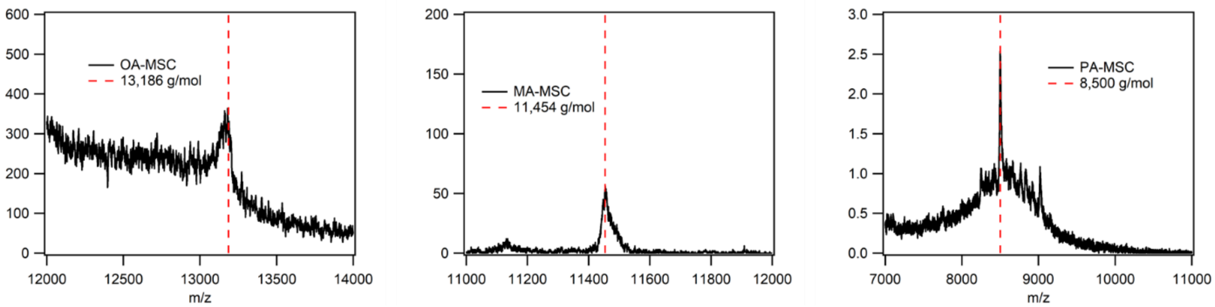

Figure 5.3. MALDI-TOF spectra of InP MSCs ligated with oleate (OA), myristate (MA), or phenylacetate (PA). The largest mass peak in each sample matches with the calculated mass (red dashed line) of a $[In_{31}P_{20}(O_2CR)_{32}]^+$ fragment.

We sought to extract a mass profile through the exchange of zinc and indium, as shown in Figure 5.4. Following addition of any amount of zinc to cluster, the largest mass peak broadens significantly. We attribute this to the non-selectivity of exchange in which zinc does not preferentially replace the 10 $In(O_2CR)_3$ remaining on the parent fragment, in addition to the strong probability that there is a distribution of clusters with less or more zinc exchanged for indium. Also, we cannot disregard that any potential zinc intercalating into the core would need to account for charge balance. Noticeably, the 4 Zn sample has a broad peak that is not shifted beyond that of the pure InP MSC which may be telling of more preferential exchange with the indium carboxylates that are lost during irradiation and ionization. Conversely, samples with 8 Zn and higher were shifted to smaller masses. Envisioning a cluster with partial surface exchange of zinc for indium and replacing half of the ten $In(O_2CR)_3$ with $Zn(O_2CR)_2$ corresponds to a fragment mass of 10,070 m/z, as indicated by the dashed black line that crosses through the broad peak of 8 Zn. Furthermore, in the case of hypothetical complete surface exchange with zinc, the fragment mass would be 8,684 g/mol, shown by the second dashed line, intersecting with the 16 Zn and 37

Zn sample peaks. These mass fragment distributions strongly support our assignment of primarily surface exchange with zinc, i.e. topotactic exchange. At higher concentrations of added zinc, interpretation of cluster fragmentation becomes more challenging as the cluster dissociates in a less predictable manner, consistent with cluster dissolution.

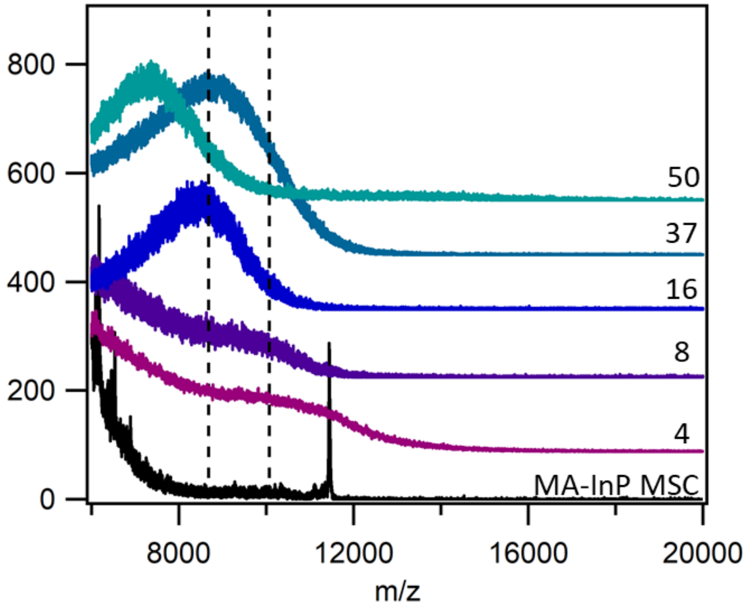

Figure 5.4. Low-mass MALDI-TOF spectra of InP MSC with increasing zinc equivalents. The dashed lines correspond to fragment masses of 10,070 g/mol and 8,684 g/mol.

To complement these findings, compositional analysis of purified samples was performed. To verify removal of free Zn5, alloyed cluster samples were purified by gel permeation chromatography (GPC) in which two consecutive columns were completed with aliquots taken after each column fraction for ICP analysis. The molar ratios of each aliquot verified that free Zn5 was removed following a single GPC purification. The plot in Figure 5.5 shows the Zn:P molar ratio of purified samples measured by ICP versus the initial reaction stoichiometry. The dashed line is representative of 1:1 cation exchange, at least to 37 equivalents, beyond which an excess of zinc was useful to evaluate the role of zinc concentration and verify if conversion to Zn_3P_2

nanomaterials was accessible. At lower equivalents, exchange appears to occur nearly stoichiometrically while above 4 equivalents, the composition deviates from stoichiometric exchange and seemingly plateaus at 37 equivalents (see zoomed out plot).

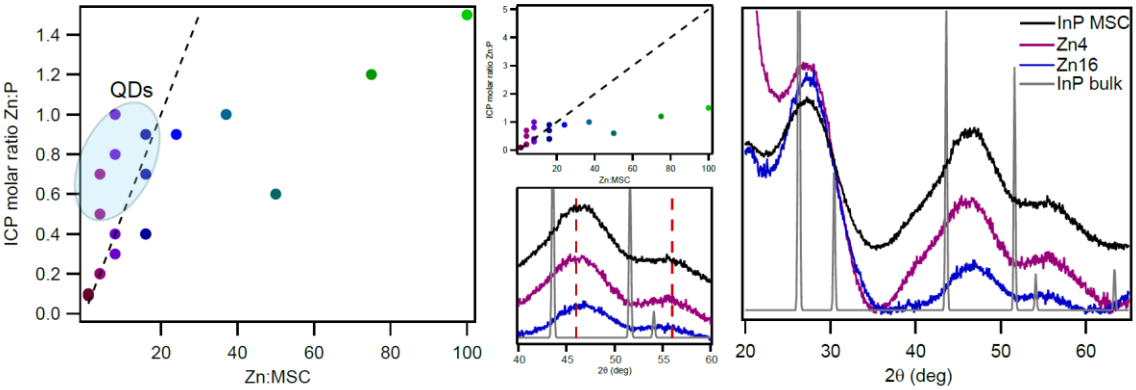

Figure 5.5. ICP and pXRD data of zinc treated clusters. Measured molar ratios of Zn:P versus the stoichiometric addition of zinc (left) Data points highlighted in the blue circle correspond to QD samples. The dashed line represents the complete 1:1 exchange of zinc for indium based on the added stoichiometry and the zoomed out plot (middle, top) highlights the plateau of zinc incorporated in the clusters. The pXRD of InP MSC, 4 Zn, and 16 Zn samples is shown (right) in comparison to bulk InP where a zoom-in of the peaks at 46 and 51 2θ (middle, bottom) may have shifted to higher angles. The dashed red line is to guide the eye through the InP MSC peak maxima.

Based on the gradual disappearance of the cluster absorbance feature and significant broadening of the ^{31}P NMR cluster resonances, the measured molar ratios of samples with 50, 75, and 100 zinc equivalents represent an amorphous mixed metal phosphide series of compounds. This data indicates that beyond the exchange of surface indium carboxylate, it is likely that only a few zinc atoms diffuse into the $In_{21}P_{20}^{3+}$ core before destabilization. The powder X-ray diffraction pattern hints at this eventual dissolution as well. The distinct cluster crystal twist-boat phase[20] is primarily conserved at 4 and 16 zinc equivalents but there is a minor shift to higher diffraction angles in the 16 Zn sample which would correspond to lattice contraction (Figure 5.5).[10] We find it highly unlikely that the InP MSC would be a suitable environment for extensive zinc exchange considering the difference in ionic radius and charge.

Together, these data support a mechanism of exchange between the 16 surface indium and zinc from the Zn5 cluster, after which several zinc atoms may exchange within the $In_{21}P_{20}^+$ core but a threshold is reached leading to destabilization of the cluster. The formation of a zinc phosphide cluster was not observed under these conditions and was deemed unlikely based on the synthetic strategies our lab has developed for the chemistry of Zn_3P_2 nanocrystals.[14,15] A similar initial progression of cation exchange was observed between cadmium and InP MSCs as well, but differences between the HSAB profile and ionic radius of cadmium and zinc, and the lattice energy of the resulting II-V cluster limit further stable intercalation of zinc atoms into the strained InP cluster core.

As described in the introduction, previous literature reports have evaluated the evolution of InP QDs synthesized with zinc, indium, and phosphorus molecular precursors. Isolated InP MSCs are a distinct approach to InP QD formation wherein the active monomer species are necessarily different from molecular monomers, forcing non-identical nucleation pathways. We sought to then investigate the role that alloyed clusters could play as single-source precursors to alloyed InP QDs.

5.3.2 *Alloyed Cluster Single-Source Precursors for Quantum Dots*

InP QDs were grown via a hot injection of InP alloyed clusters (40 mg dissolved in 1 mL 1-octadecene [ODE]) into a bath of ODE (5 mL) at 290 °C under a nitrogen atmosphere. Unlike other MSC materials that progress towards larger nanomaterials via Ostwald staging, i.e. quantized monomer addition, or oriented attachment, InP particle evolution occurs by cluster dissolution and re-nucleation by monomer species distinct from those derived from molecular precursors involving $P(SiMe_3)_3$.[21] Growth reactions were monitored by UV-Vis and PL spectroscopy (Figure 5.6) and we observed that over all concentrations of zinc (0-100 equivalents), growth was complete within 5-10 minutes. Based on the absorbance values at high energy wavelengths,[18] the concentration of InP particles was consistent across reactions performed under these conditions. We hypothesize that across this series, the initial number of nuclei is similar but the monomer species active in particle growth is inhibited by the presence of less reactive zinc complexes. With increasing zinc content, the final LEET blue-shifted from 580 nm (0 Zn) to a less defined feature at 490 nm (100 Zn). Furthermore, the samples with 50+ equivalents of zinc continued to blue-shift at room temperature in the day following QD growth, indicating that the product obtained at elevated temperatures could not maintain a stable crystal phase.

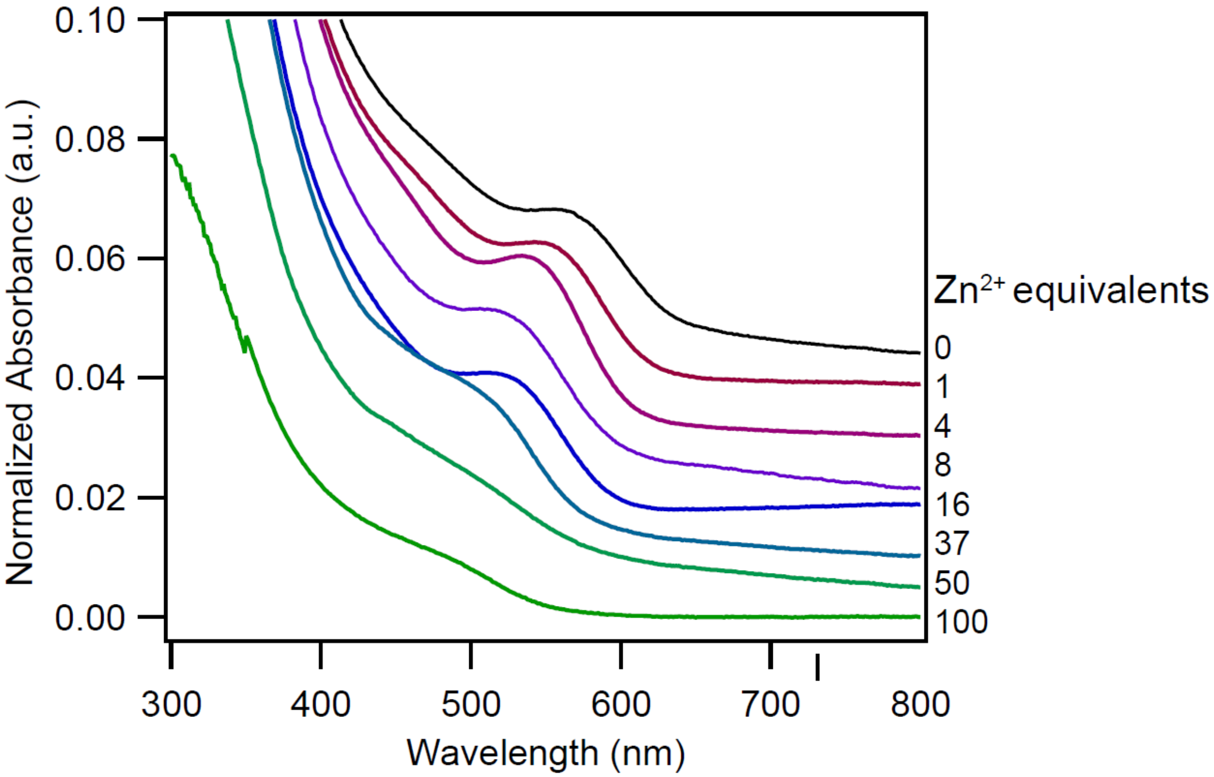

Figure 5.6. Stacked UV-Vis spectra of hot-injection reactions to convert alloyed InP clusters into QDs.

The trend observed in the absorbance spectrum is reflected by the particle sizes measured by transmission electron microscopy (TEM). A representative TEM image of 1 Zn, 4 Zn, and 16 Zn is shown in Figure 5.7 where measured particle diameters are 2.6 nm, 2.3 nm, and 2.1 nm, respectively. Particle diameters were not measured for the 37 Zn sample due to the observed morphology variation and it is possible that amorphous Zn_3P_2 exists among the diverse population of particles present. Other groups that have imaged InP QDs nucleated in the presence of zinc additives also observe less uniform particle morphologies with higher zinc concentrations, i.e. greater than 1:1 Zn:In ratio.[10] Additionally, the pXRD pattern of the 37 Zn sample was significantly broadened, indicating a loss of crystallinity (Figure 5.7). For the remainder of this study, we focused our efforts on InP QDs with a ratio of 0, 4, 8, and 16 Zn:MSC.

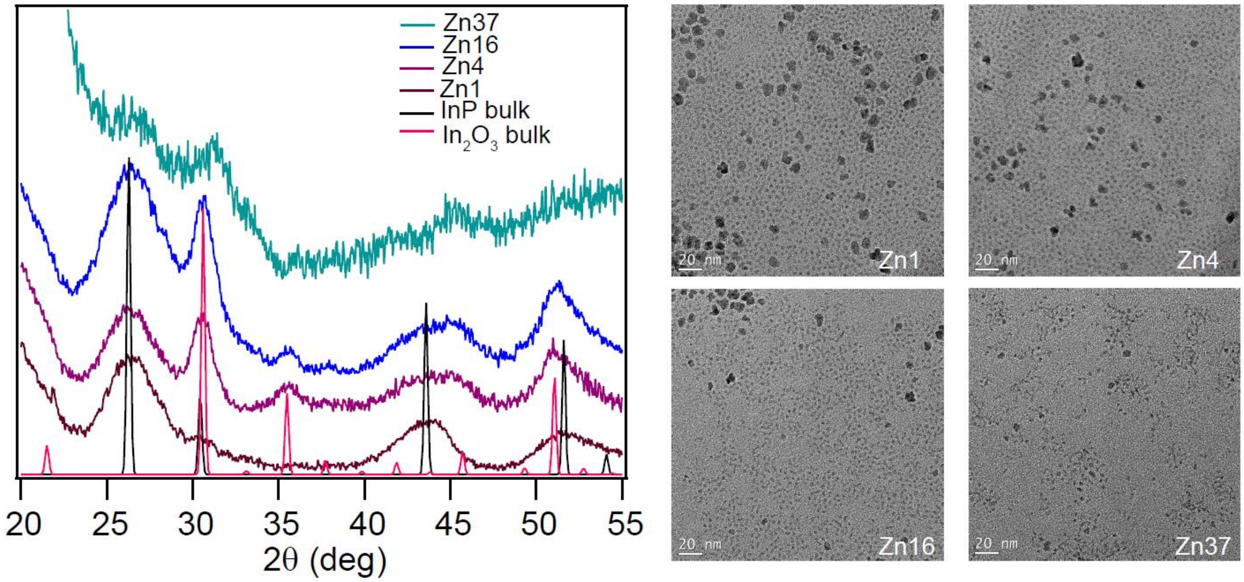

Figure 5.7. pXRD of alloyed QD products and representative TEM images of select samples.

Notably, only QD reactions that included some amount of zinc were accompanied by the formation of ca. 11 nm diameter In_2O_3 nanocrystals (shown in Figure 5.7 TEM images), as confirmed by lattice fringe analysis and pXRD. In_2O_3 by-products have been previously observed as a thermolysis product of indium carboxylates that were displaced from InP QD surfaces by zinc and cadmium carboxylates.[12,22] We hypothesize that in an analogous fashion, zinc substitutes into indium sites and the ejected indium carboxylates decompose as In_2O_3. We believe this process is initiated during cluster dissolution and growth since In_2O_3 was observed regardless of the extent of alloyed cluster precursor purification.

In_2O_3 diffraction peaks overlap with two of the major InP diffraction peaks at 43 and 53 2θ. While most of the In_2O_3 can be removed through careful size selective precipitation, a thorough analysis of the InP diffraction patterns has been limited. A cursory examination of the InP pXRD data does reveal that no other crystalline phosphide phases are present. Homogeneous zinc alloying, or lattice contraction, would be distinguishable by shifts to higher angles which is not apparent in the strongest peak at 26 2θ. Thus, we propose that the extent of zinc alloying that occurs is limited to the outer layer of the InP QD.

In agreement with surface zinc passivation, the measured InP PL QYs increase from 0.15% up to 19% in 0 Zn and 16 Zn, respectively (Figure 5.8), although this quantification includes both InP band edge emission and the non-suppressed trap emission. These QYs are also comparable to the range reported for zinc-alloyed InP QDs prepared by a one-pot molecular precursor synthesis. As expected, the compositional analysis of our particles (4, 8, and 16 Zn equivalents) shows that zinc, indium, and phosphorus are all present. The measured Zn:P ratio nearly doubles from that of the measured Zn:P in the alloyed clusters (Figure 5.5). It has been posited by Houtepen *et al.* that phosphorus vacancies form to balance charge as zinc is incorporated which would be consistent with our experimental data.[10]

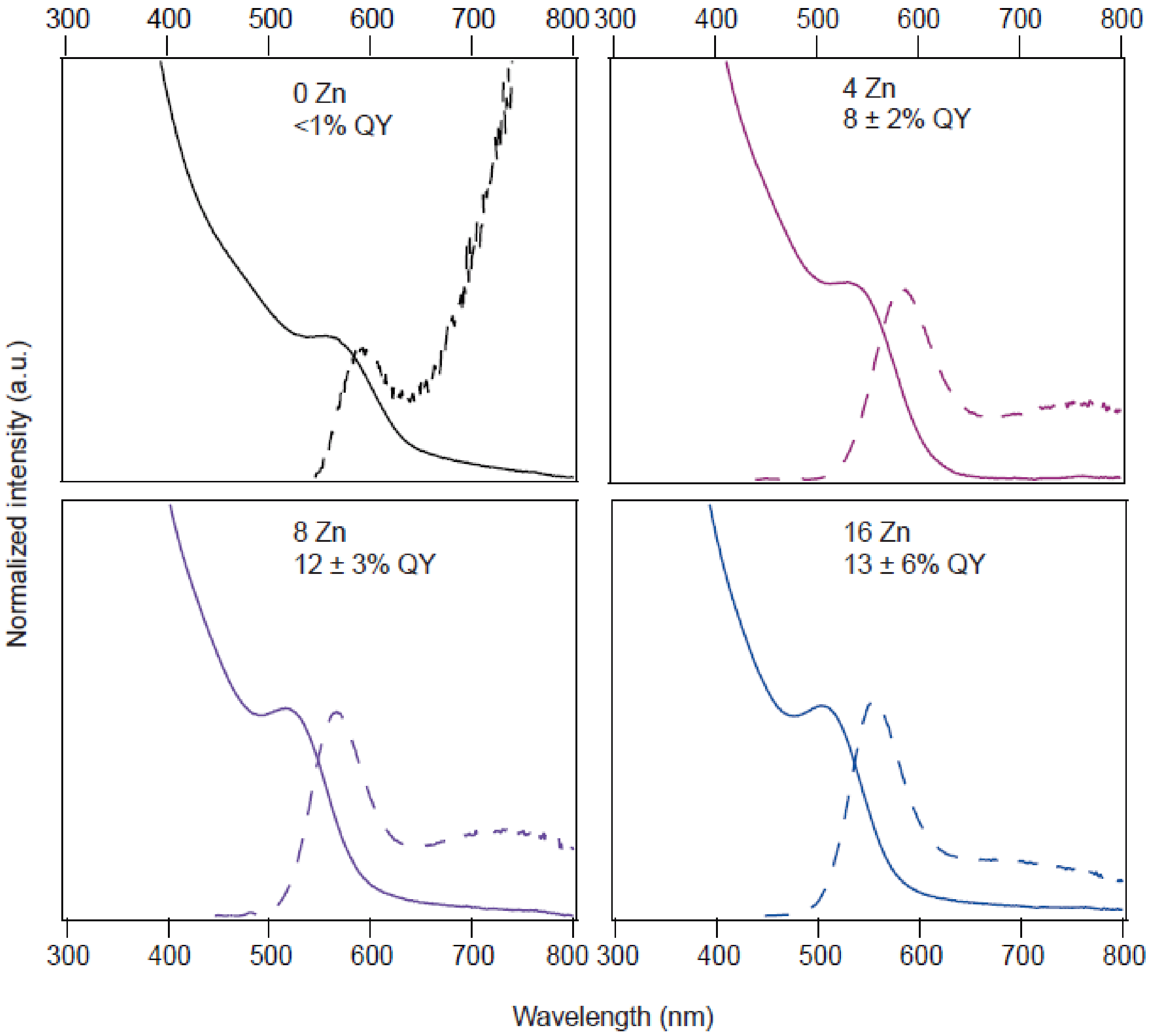

Figure 5.8. UV-Vis and PL spectra of QD products from 0, 4, 8, and 16 Zn and InP precursors.

Although there is no discernable lattice contraction suggested by the X-ray diffraction patterns, we sought to study the impact of zinc alloying on the lattice parameter of these InP QDs. ZnS and ZnSe have a 7.6% and 3.4% lattice mismatch with InP, respectively, but the detrimental impact of lattice strain can be alleviated through the formation of a gradient alloy at the interface and consequently, improve core-shell optical properties. We selected a ZnSeS gradient alloy shell to mitigate direct contact between ZnS and InP and to confine the exciton in the core more effectively than ZnSe with ZnS. Experimental conditions were optimized by Lee and co-workers to afford PL QYs up to 65% and 70 nm fwhm emission linewidths.[23] Briefly, zinc stearate was added in excess of InP (10:1 Zn:In) at elevated temperatures after which a solution of TOPSe and TOPS was added over a gradual heat-up. Further details regarding shell growth can be found in the Experimental section.

The plot in Figure 5.9 summarizes the measured PL QYs of InP/ZnSeS particles with an initial Zn:MSC ratio of 0, 4, 8, and 16. There is a direct correlation between improved PL QYs and increasing Zn:MSC ratios where the highest QY, 85%, was measured for the 16Zn sample. In contrast, a 55% PL QY was measured for the non-alloyed InP QD control sample. While the emission linewidths are broad in comparison to other shelling procedures that report linewidths in the range of 40-60 nm, there is a consistent decrease from 0Zn, 85 nm fwhm at 586 nm, to 16Zn, 66 nm fwhm at 556 nm, which likely corresponds to more uniform shell deposition.

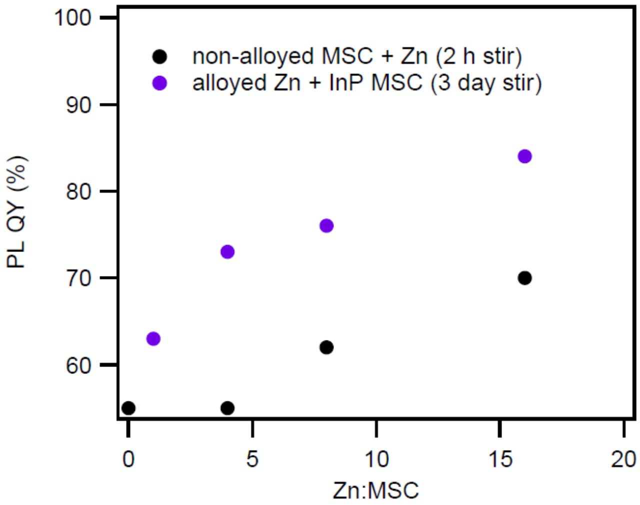

Figure 5.9. Plot of QYs versus the amount of zinc added to InP clusters.

We wanted to verify that these results are relevant to the formation of a zinc alloyed cluster, so InP QD growth reactions were performed in a fashion analogous to the molecular precursor approach. InP MSCs were stirred with Zn5 for only 2 hours, over which we did not observe evidence of alloying by PL or ^{31}P NMR spectroscopy, then converted these compounds to InP QDs via hot-injection at 290 °C. The QD optical properties of the 2 hour cation exchange reaction were comparable to that of the 3 day cation exchange but following shell growth, a stark difference can be seen between the two experiments (Figure 5.9). Clusters that were only given 2 hours to react with Zn5 before QD growth had consistently lower PL QYs with a maximum of 70%. We consider this as direct evidence identifying the importance of equilibrating to an alloyed cluster end-product before utilizing these materials as single-source precursors.

5.4 Conclusions

We observe a topotactic exchange of zinc for the 16 surface indium of the $In_{37}P_{20}$ MSC along with gradual cluster dissolution as zinc initially diffuses into the core. The replacement of indium with this divalent cation with a shortened M-P bond length contributes to structural instability. The formation of robust InP clusters with pre-formed Zn-P bonds can be utilized as a single-source precursor for alloyed InP QDs. Since nanocrystal growth proceeds via dissolution of the cluster, rather than oriented attachment or Ostwald staging, this synthetic route benefits from monomer species unique from those in the molecular nucleation pathways. Upon shelling, a clear trend was observed in which the QYs of InP/ZnSeS increased from 55% to 85% on the basis of Zn:MSC concentration. We attribute the improved InP QD optical properties to zinc alloying at the surface considering the absence of significant lattice contraction. Notably, the optical properties of InP/ZnSeS core/shell nanocrystals are greatly improved, indicated by an increase in PL QY of approximately 10%, following equilibration of the alloyed cluster precursors prior to QD growth. Atomically precise InP MSCs provide a robust model for cation exchange studies and have now been applied as viable precursors towards larger alloyed nanocrystals, expanding upon the valuable chemistry of composition tailoring in covalent III-V materials.

5.5 Experimental

5.5.1 *General Considerations*

All glassware was dried in a 160 °C oven overnight prior to use. All reactions, unless otherwise noted were run under an inert atmosphere of nitrogen using a glovebox or using standard Schlenk techniques. *Warning: Diethyl zinc and $P(SiMe_3)_3$ are both pyrophoric reactants and were handled with care within a nitrogen glovebox.* Indium acetate (99.99%), myristic acid (≥99%), trioctylphosphine (97%), sulfur powder (99.5% sublimed), selenium powder (99.99%), zinc acetate (99.99%), zinc stearate, and *trans*-2-[3-(4-tert-Butylphenyl)-2-methyl-2-propenylidene]malononitrile (DCTB) (≥99.0%) were purchased from Sigma-Aldrich Chemical Co. and used without further purification. Diethyl zinc (95%) was purchased from Strem Chemicals and stored in a nitrogen atmosphere glovebox. All solvents, including toluene, pentane, and acetonitrile, were either purchased anhydrous from Sigma-Aldrich Chemical Co. or collected from a solvent still and stored over 4 Å molecular sieves in a nitrogen-filled glove box. 1-octadecene was dried over CaH_2, distilled, and stored over 4 Å molecular sieves in a nitrogen-filled glove box. C_6D_6 was purchased from Cambridge Isotope Labs and was similarly dried and stored. Bio-Beads S-X1 were purchased from Bio-Rad Laboratories. Omni Trace nitric acid was purchased from EMD Millipore and used without further purification. 18.2 MΩ was collected from an EMD Millipore water purification system. $P(SiMe_3)_3$ was prepared following literature procedures.[24]

^{31}P and ^{1}H NMR spectra were collected on a 700 MHz Bruker Avance spectrometer. UV-Vis spectra were collected on a Cary 5000 spectrophotometer from Agilent. Fluorescence and quantum yield measurements were taken on a Horiba Jobin Yvon FluoroMax-4 fluorescence spectrophotometer with the QuantaPhi integrating sphere accessory. ICP-OES was performed using a Perkin Elmer Optima 8300. Powder X-ray diffraction data was collected using a Bruker D8 Discover diffractometer. TEM images were collected on an FEI Tecnai G2 F20 microscope using an ultrathin carbon film on holey carbon purchased from Ted Pella Inc. MALDI-TOF data was collected on a Bruker Autoflex II instrument using DCTB as a matrix. All XPS spectra were collected using a Surface Science Instruments S-probe spectrometer.

5.5.2 *Synthesis of InP MSCs*

InP magic-sized clusters (MSCs) were synthesized following a modified preparation.[16] Indium acetate (1.40 g, 4.8 mmol) and myristic acid (3.98 g, 17.4 mmol) were heated neat at 100 °C under reduced pressure overnight. Dry toluene (40 mL) was added to the reaction flask at room temperature under N_2 the following day, after which $P(SiMe_3)_3$ (698 µL, 2.4 mmol) was measured into 5 mL of toluene and injected into the indium myristate solution at 100 °C. Cluster growth was complete within 1 hour as indicated by the characteristic absorbance peak at 386 nm. The particles were concentrated down to a minimal volume of toluene, centrifuged to remove insoluble products, and purified by GPC.

5.5.3 *Zn5 Cluster Synthesis*

$Zn_5(O_2CCH_3)_6(CH_2CH_3)_4$ was synthesized following a literature procedure where zinc acetate (1.107 g, 6.03 mmol) was dissolved in toluene (5 mL) and then diethyl zinc (413 uL, 4.02 mmol) was added drop-wise to the stirring solution.[25] The reaction was allowed to complete at room temperature overnight. The toluene was concentrated under vacuum and then the Zn5 cluster was precipitated with the addition of heptane. The white solid was dried down and confirmed pure by ^1H NMR.

5.5.4 *Zn^{2+} Titrations*

Typical titration experiments were conducted by dissolving 40 mg of $In_{37}P_{20}(O_2C_{14}H_{27})$ in toluene (2 mL) and adding varying equivalents (1, 4, 8, 16, 24, 37, 50, 75, and 100) of Zn^{2+} from a stock solution of Zn5 to stir at room temperature. The Zn5 stock solution was prepared by dissolving 54 mg (7 x 10^{-3} mol) of Zn5 in 2 mL of toluene to make a 0.034 M solution. The reaction was monitored by UV-Vis aliquots taken over 2, 20, 48, and 84 h intervals. Reactions to examine the products of InP MSCs and diethyl zinc or zinc myristate were conducted in a similar fashion either at room temperature or heated to 50 °C under N_2 on a Schlenk line. Samples were purified by GPC by loading the reaction solution directly into a toluene-based column. For the 2 h reaction time samples, clusters were dissolved in 1 mL of ODE rather than toluene to prepare for hot-injection.

5.5.5 *Alloyed InP QD Growth*

In a typical QD growth reaction, the alloyed clusters were resuspended in 1 mL of 1-ODE and rapidly injected into a flask containing 5 mL of ODE at 290 °C under active N_2 on a Schlenk line. The reaction was monitored by UV-Vis and PL aliquots to determine the endpoint of growth, at which point the heating mantle was removed and the flask was placed into a silicone oil bath to rapidly cool down. For sample characterization, ODE was removed under vacuum distillation and the remaining QD paste was resuspended in a minimal amount of toluene inside a glovebox. Acetonitrile was added to precipitate the particles and centrifuged at 7500 rpm for 10 minutes. After removing the clear supernatant, the film of QDs was resuspended in toluene and purified by GPC. For ZnSeS growth, InP QDs were kept in the same flask following the hot-injection reaction in order to keep stoichiometry and volumes consistent.

5.5.6 *ZnSeS Shell Growth*

Shell growth was performed using a modified literature procedure from Lee *et al*.[23] TOPSe and TOPS stock solutions (1 M) were prepared by dissolving either 128 mg of sulfur powder (4 mmol) or 316 mg of selenium (4 mmol) in 4 mL of TOP. InP QDs that had previously been formed from clusters solutions were estimated to have 0.09 mmol of In3+, assuming a 100% conversion of cluster to QD. The InP QD solutions, in approximately 6 mL of ODE, were heated to 220 °C. A suspension of zinc stearate, $Zn(st)_2$, was prepared by placing 570 mg (0.9 mmol) in 2 mL of ODE and then injected into the QDs. A blue-shift was observed, corresponding to zinc surface passivation, which appeared to stop changing after 15 minutes. At this point, TOPS (810 µL, 0.81 mmol) and TOPSe (90 µL, 0.09 mmol) were measured out into 1 mL of ODE and then injected into the InP/Zn solution. The temperature was set to 300 °C and the PL was monitored until no further increases were measured (40 minutes following TOPS/Se injection). The reaction was cooled down by placing the flask in an oil bath. For characterization, ODE was removed under vacuum distillation, resuspended in toluene, filtered through a syringe filter (PTFE), and purified by precipitation cycles with toluene/EtOH as the solvent/non-solvent.

5.6 References

(1) White, S. L.; Banerjee, P.; Chakraborty, I.; Jain, P. K. Ion Exchange Transformation of Magic-Sized Clusters. *Chem. Mater.* **2016**, *28* (22), 8391–8398.

(2) Stein, J. L.; Steimle, M. I.; Terban, M. W.; Petrone, A.; Billinge, S. J. L.; Li, X.; Cossairt, B. M. Cation Exchange Induced Transformation of InP Magic-Sized Clusters. *Chem. Mater.*, **2017** *29* (18), 7984-7992..

(3) Yang, J.; Muckel, F.; Baek, W.; Fainblat, R.; Chang, H.; Bacher, G.; Hyeon, T. Chemical Synthesis, Doping, and Transformation of Magic-Sized Semiconductor Alloy Nanoclusters. *J. Am. Chem. Soc.* **2017**, *139* (19), 6761–6770.

(4) Pearson, R. G. Absolute Electronegativity and Hardness: Application to Inorganic Chemistry. *Inorg. Chem.* **1988**, *27* (4), 734–740.

(5) Pyykkö, P.; Atsumi, M. Molecular Single-Bond Covalent Radii for Elements 1–118. *Chem. – Eur. J. 15* (1), 186–197.

(6) Tamang, S.; Lincheneau, C.; Hermans, Y.; Jeong, S.; Reiss, P. Chemistry of InP Nanocrystal Syntheses. *Chem. Mater.* **2016**, *28* (8), 2491–2506.

(7) Tessier, M. D.; Dupont, D.; De Nolf, K.; De Roo, J.; Hens, Z. Economic and Size-Tunable Synthesis of InP/ZnE (E = S, Se) Colloidal Quantum Dots. *Chem. Mater.* **2015**, *27* (13), 4893–4898.

(8) Xi, L.; Cho, D.-Y.; Besmehn, A.; Duchamp, M.; Grützmacher, D.; Lam, Y. M.; Kardynał, B. E. Effect of Zinc Incorporation on the Performance of Red Light Emitting InP Core Nanocrystals. *Inorg. Chem.* **2016**, *55* (17), 8381–8386.

(9) Koh, S.; Eom, T.; Kim, W. D.; Lee, K.; Lee, D.; Lee, Y. K.; Kim, H.; Bae, W. K.; Lee, D. C. Zinc–Phosphorus Complex Working as an Atomic Valve for Colloidal Growth of Monodisperse Indium Phosphide Quantum Dots. *Chem. Mater.* **2017**, *29* (15), 6346–6355.

(10) Pietra, F.; De Trizio, L.; Hoekstra, A. W.; Renaud, N.; Prato, M.; Grozema, F. C.; Baesjou, P. J.; Koole, R.; Manna, L.; Houtepen, A. J. Tuning the Lattice Parameter of InxZnyP for Highly Luminescent Lattice-Matched Core/Shell Quantum Dots. *ACS Nano* **2016**, *10* (4), 4754–4762.

(11) Thuy, U. T. D.; Reiss, P.; Liem, N. Q. Luminescence Properties of In(Zn)P Alloy Core/ZnS Shell Quantum Dots. *Appl. Phys. Lett.* **2010**, *97* (19), 193104.

(12) Stein, J. L.; Mader, E. A.; Cossairt, B. M. Luminescent InP Quantum Dots with Tunable Emission by Post-Synthetic Modification with Lewis Acids. *J. Phys. Chem. Lett.* **2016**, *7* (7), 1315–1320.

(13) Rafipoor, M.; Dupont, D.; Tornatzky, H.; Tessier, M. D.; Maultzsch, J.; Hens, Z.; Lange, H. Strain Engineering in InP/(Zn,Cd)Se Core/Shell Quantum Dots. *Chem. Mater.* **2018**, *30* (13), 4393–4400.

(14) Glassy, B. A.; Cossairt, B. M. Ternary Synthesis of Colloidal Zn3P2 Quantum Dots. *Chem. Commun.* **2015**, *51*, 5283–5286.

(15) Glassy, B. A.; Cossairt, B. M. Resolving the Chemistry of Zn3P2 Nanocrystal Growth. *Chem. Mater.* **2016**, *28* (17), 6374–6380.

(16) Gary, D. C.; Flowers, S. E.; Kaminsky, W.; Petrone, A.; Li, X.; Cossairt, B. M. Single-Crystal and Electronic Structure of a 1.3 Nm Indium Phosphide Nanocluster. *J. Am. Chem. Soc.* **2016**, *138* (5), 1510–1513.

(17) Gary, D. C.; Petrone, A.; Li, X.; Cossairt, B. M. Investigating the Role of Amine in InP Nanocrystal Synthesis: Destabilizing Cluster Intermediates by Z-Type Ligand Displacement. *Chem. Commun.* **2016**, *53* (1), 161–164.

(18) Xie, L.; Shen, Y.; Franke, D.; Sebastián, V.; Bawendi, M. G.; Jensen, K. F. Characterization of Indium Phosphide Quantum Dot Growth Intermediates Using MALDI-TOF Mass Spectrometry. *J. Am. Chem. Soc.* **2016**, *138* (41), 13469–13472.

(19) Kasuya, A.; Sivamohan, R.; Barnakov, Y. A.; Dmitruk, I. M.; Nirasawa, T.; Romanyuk, V. R.; Kumar, V.; Mamykin, S. V.; Tohji, K.; Jeyadevan, B.; et al. Ultra-Stable Nanoparticles of CdSe Revealed from Mass Spectrometry. *Nat. Mater.* **2004**, *3* (2), 99–102.

(20) Ritchhart, A.; Cossairt, B. M. Templated Growth of InP Nanocrystals with a Polytwistane Structure. *Angew. Chem. Int. Ed. 57* (7), 1908–1912.

(21) Friedfeld, M. R.; Stein, J. L.; Cossairt, B. M. Main-Group-Semiconductor Cluster Molecules as Synthetic Intermediates to Nanostructures. *Inorg. Chem.* **2017**, *56* (15), 8689–8697.

(22) Narayanaswamy, A.; Xu, H.; Pradhan, N.; Kim, M.; Peng, X. Formation of Nearly Monodisperse In2O3 Nanodots and Oriented-Attached Nanoflowers: Hydrolysis and Alcoholysis vs Pyrolysis. *J. Am. Chem. Soc.* **2006**, *128* (31), 10310–10319.
(23) Lim, J.; Bae, W. K.; Lee, D.; Nam, M. K.; Jung, J.; Lee, C.; Char, K.; Lee, S. InP@ZnSeS, Core@Composition Gradient Shell Quantum Dots with Enhanced Stability. *Chem. Mater.* **2011**, *23* (20), 4459–4463.
(24) Gary, D. C.; Cossairt, B. M. Role of Acid in Precursor Conversion During InP Quantum Dot Synthesis. *Chem. Mater.* **2013**, *25* (12), 2463–2469.
(25) Orchard, K. L.; White, A. J. P.; Shaffer, M. S. P.; Williams, C. K. Pentanuclear Complexes for a Series of Alkylzinc Carboxylates. *Organometallics* **2009**, *28* (19), 5828–5832.